論文 / 著書情報
Article / Book Information

題目(和文)	鋼橋を対象としたロボティック点検手法と腐食損傷評価に関する研究
Title(English)	A study on a robotic inspection method and corrosion damage evaluation of steel bridges
著者(和文)	阿久津絢子
Author(English)	Ayako Akutsu
出典(和文)	学位:博士(工学), 学位授与機関:東京工業大学, 報告番号:甲第10804号, 授与年月日:2018年3月26日, 学位の種別:課程博士, 審査員:佐々木 栄一,廣瀬 壮一,WIJEYEWICKREMA ANIL,岩波 光保,千々和 伸浩,小林 裕介
Citation(English)	Degree:Doctor (Engineering), Conferring organization: Tokyo Institute of Technology, Report number:甲第10804号, Conferred date:2018/3/26, Degree Type:Course doctor, Examiner:,,,,,
学位種別(和文)	博士論文
Type(English)	Doctoral Thesis

Doctoral Dissertation

A Study on a Robotic Inspection Method and Corrosion Damage Evaluation of Steel Bridges

Tokyo Institute of Technology

Department of Civil Engineering

Supervised by Eiichi SASAKI

Ayako AKUTSU

Contents

List of Figures

Chapter 1: Introduction

Chapter 2: Development of a Self-Propelled Inspection Robot for Bridges

Chapter 3: Capability of Robotic Inspection System

Chapter 4: Proposal of Corrosion Damage Evaluation Method

List of Tables

Chapter 2: Development of a Self-Propelled Inspection Robot for Bridges

Chapter 3: Capability of Robotic Inspection System

Chapter 4: Proposal of Corrosion Damage Evaluation Method

List of symbols

S', S'_0	Effective sectional area between an air pump and an air pad [mm^2]
Q, Q_0	Flow of vacuumed air [l/min]
P_p, P_{p0}, P_a, P_{base}	Pressure of vacuumed air [MPa]
$C_{airflow}$	Coefficient of air flow calculation [l/min·N]
α'	Effective sectional area between an air pad and surfaces [mm^2]
g	Gap coefficient [μm]
N	Number of air pads
D	Diameter of air pads [mm]
F_v, F_h	Suction force [N]
R_a	Average surface roughness [μm]
R_z	Maximum surface height [μm]
W	Wind load [N]
ρ_a	Air density [kg/m^3]
U_d	*W*ind speed [m/s]
A_n	Projected area [m^2]
G_a	Gust response factor
C_D	Drag coefficient
N_1, N_2, n_1, n_2, k_1, k_2, n_{10}, n_{20}	Pixel
$f(n_1,n_2)$, $g(n_1,n_2)$	Image
$F(k_1,k_2)$, $G(k_1,k_2)$	2D DFTs of the image
$R_{FG}(k_1,k_2)$	Normalized mutual power spectrum of the image
$r_{fg}(k_1,k_2)$	POC function of the image
e	Napier's constant
t	Time [s]
$\Psi_{\theta k}(n_{10}, n_{20})$	Wavelet coefficient or two dimensional gabor wavelet
ψ_g	Mother wavelet: gabor wavelet
α^k	Scaling parameter of two dimensional wavelet transformation.
u	Input signal
v	Output signal
s	Complex number

$U(s)$	Laplace transforms of input signal
$V(s)$	Laplace transforms of output signal
$G(s)$	Transfer function
γ^2	Coherence
W_{uu}, W_{vv}, W_{uv}	Power spectrum and the cross spectrum of the input signal and the output signal .
δ	Penetration depth [m]
f, f_L, f_t, f_c	Frequency [Hz]
μ	Relative permeability
σ	Electro conductivity [S/m]
v_v, V_m, V	Voltage [V]
I, I_m	Current [A]
R	Resistance [Ω]
L	Inductance [H]
Z	Impedance
ω	Angular velocity [rad/s]
ϕ	Phase transition
B	Magnetic flux density [T]
E	Electric field [N/C]
J	Current density [A/m²]
W_e	Eddy current loss [W/m^3]
ρ	Resistivity
$W_\psi[u(t)]$	Wavelet coefficient: Mexican hat
ψ	Mother wavelet: Mexican hat
a	Scale parameter of Wavelet transformation
b	Shift parameter
d, d_0	Plate thickness [mm]
l, l_0	Lift-off [mm]
WC_L, WC_t	Wavelet Coefficient
$P_{xx}(f)$, $P_{yx}(f)$	Power spectral density and Cross power spectral density of the input and output waveform.
Φ	Phase [degree]

Acknowledgements

I wish to express my deepest gratitude to my supervisor, Associate Professor Eiichi Sasaki for his very kind supports, advices and encouragements. I am thankful for his aspiring guidance, invaluably constructive criticisms and friendly advices during the research work.

I wish to express my gratitude to Associate Professor Yusuke Kobayashi, Dr. Atsushi Tanabe and Dr. Hisatada Suganuma for their accurate advice and kind encouragements. I am sincerely grateful to them for their truthful and constructive views on a number of issues related to this research. I would like also to thank sincerely Assistant Professor Hiroshi Tamura for his kind support, very friendly advices and encouragements. A special thanks goes to Ms. Ishihara and Ms. Hamada for her support in non-research field. They helped many office works.

I would like to offer my special thanks to Dr. Takeya. He gave me fundamental knowledge about developing robots. I learned many things thorough his advice and discussion. Dr. Natdanai and Dr. Cao gave me advices on my research works, and experiments. I wish to thank our laboratory members, PhD. student Ms. Sanjeema, Mr. Ando, Mr. Iizuka and Mr. Kurishiba. It was good experience for me to help their research works. It was good experience for me to discuss on our research works and spending great time with PhD. student Ms. Tuttipongsawat, PhD. student Ms. Mohamed, PhD. student Mr. Piseth, Mr. Mishima, Ms. Irie, Ms. Rodthong and Ms. Shigeta.

I wish to special big thank Ms. Scorupski for her advice about my research work and English. She gave me useful view and remarks of my research works. Furthermore, I would like to thank our graduated laboratory members, Mr. Tajima, Mr. Navicus, Mr. Ueda, Mr. Umekawa, Mr. Kanamori, Mr. Ebisawa, Mr. Itami, Mr. Tominaga. Mr. Ota for their kind help and friendship. Especially, I learned many things from assisting their research work and discussion with them.

Finally, I would like to thank to my mother Ms. Tomiko Akutsu for her long support and understanding.

Abstract

Bridge maintenance is a topic that is gaining more and more significance in the field of civil engineering and so, performing inspection periodically has become an important theme. Particularly in the case of steel bridges, there are many areas that are difficult to access and see directly, hence it is difficult to acquire key information such as steel corrosion or the deterioration of decks. In this research, robotic inspection has been considered as a means to acquire this aforementioned, and a method that is simple, safe, low cost, and does not require scaffolding has been investigated and proposed. Moreover, a corrosion damage evaluation method that can easily obtain the rust thickness and residual thickness of corroded steel members based on eddy current testing has been newly developed. The proposed self-propelled robot uses vacuum suction for attachment and movement, and both a visual inspection and detailed inspection system using small sensors has been implemented as inspection functions. Furthermore, the capacity of robotic movement and the inspection functions were confirmed through experiments on actual bridges. The proposed corrosion damage evaluation method has been investigated as both an independent inspection method as well as one of the robotic inspection functions.

***Keywords**: Bridge maintenance, robotic inspection, self-propelled robot, corrosion damage evaluation*

Chapter 1

Introduction

Abstract

In this chapter, the background, related research, and purpose and objectives of this research have been discussed. Related research has focused on several types of existing robots that are used for inspection or to evaluate corrosion damage using eddy current testing, to understand difficulties or needs during inspection and taking measurements. Taking into account the background and related research, pertinent purpose and objectives were determined for this research. To achieve an effective and efficient inspection of steel bridges, inspection by use of a robot, which is called robotic inspection in this study, and corrosion damage evaluation have been considered.

1.1. Background

Infrastructure including steel bridges constitutes an important transportation network that contributes to the national economy and transportation system [1]. In Japan, the construction of bridges rapidly increased, especially in the period of high economic growth during the 1960s [2,3]. Currently, there are about 700,000 road bridges exceeding two meters in length and approximately 30% of those are steel bridges [4]. At present, the construction of steel bridges has slowed down. However, 20% of all bridges are 50 years or older, and moreover, it is expected that this number is increasing swiftly [5-9]. In addition, steel bridges in particular are prone to deterioration due to corrosion. These facts clearly indicate that bridges in Japan are facing deterioration problems. If this deterioration continues to progress and rebuilding or large-scale repair is consequently required, an enormous cost will be incurred, resulting in economic losses.

Based on the abovementioned situation, bridge maintenance is a topic that is gaining more and more significance in the field of civil engineering [10,11]. Presently bridges cannot simply meet the demands of traffic loadings, but they must also ensure security and reliability under various natural environment conditions. It is therefore important to improve the safety of bridges, maintain their service life, and reduce their life-cycle cost [12-16]. A bridge inspection process normally involves three steps; first, regular inspection to recognize the damage conditions of various structures predominantly using visual inspection, second, detailed inspection to check the structural behavior of the bridge using various inspection devices for cause identification, and finally, consideration of countermeasures that can be performed for the repair and reinforcement of the bridge structure [4,6,7,11,17]. For steel bridges, in particular, corrosion is the main reason for damage, followed by damage on deck [18-20]. Steel bridges using weathering steel materials are being constructed, yet accumulated rust layer accompanied by delamination due to corrosion has been discovered in coastal areas [19,21-23]. For these reasons, it is considered preferable to conduct corrosion specific inspections, as well as regular inspections of steel bridges, to acquire corrosion damage information such as the presence of rust and reduction in steel plate thickness [24-27]. To maintain bridges effectively and efficiently within a limited budget, developing technologies that can perform close visual inspection without requiring large-scale inspection devices and many inspectors is essential [28,29]. These technologies are considered extremely useful for making periodic inspection more feasible.

There are many bridges that are approaching the time for the need of rebuilding due to deterioration, yet in recent economic conditions, rebuilding is proving difficult. Therefore, it is important to predict serious damage in advance through maintenance, and promote long service life by applying countermeasures to minor damages. However, there is a great lack in the number of inspectors required for the number of existing bridges, the time required for inspection is

lengthy, inspection cost is high, and hence it is currently difficult to conduct inspection periodically as required. In addition, it is considered the issue of current inspection is that it is difficult to keep quantitative records because inspection results depend on the inspector's skills. Furthermore, steel bridges comprise many sections that are invisible location, or either narrow or difficult to access by inspectors. These factors also contribute to making inspection difficult as it becomes necessary to have large facilities such as scaffolding for inspection to be carried out. For example, in a steel bridge, sections that are difficult to inspect include a narrow part in a truss component or the inside of a closed cross-section of a steel box girder. It is required to perform simple inspections frequently without requiring large-scale facilities such as scaffolding and bridge inspection vehicles (**Figure 1.1**) and many inspectors [28,29].

An inspection using a robot can be considered as one means to realize aforementioned inspection. Recently, inspection technologies and monitoring techniques using robots (referred to as robotic inspection in this research) have gained much attention as a means to accomplish the necessary aforementioned inspections. The relationship between basic inspection processes and potential robotic inspection is shown in **Figure 1.2**. During bridge monitoring, it is expected that data such as deformation is obtained for long term use [7,30,31]. Therefore, in this research, robotic inspection has been focused as inspection technologies. Through robotic inspection, it is expected that inspection functions that can be used for bridge inspection can be established, in addition to developing robots equipped with various attachments and movement functions.

The advantages of performing robotic inspection is that large equipment such as scaffolding or special vehicles is not necessary and inspection cost can be reduced. The need of skilled inspectors is also reduced, moreover, the inspection results could be evaluated later by skilled inspectors since the results obtained by performing the inspection using a robot is not greatly affected by the skill of the inspector carrying out the actual inspection. Therefore, it is expected that it will be easier to conduct inspection periodically [32-36] and to record inspection results quantitatively. However, steel bridges not only have steel components but also concrete components such as decks or piers, and so the robot must have the ability to move along these components also. In addition, since there are also many parts that become blind spots for inspectors, it is considered important to acquire information regarding the inspection site, that is, to acquire the inspection position of the robot. In current robotic inspection, the application of robots which have supplementary features such as rails [37-41], wall climbing type robots [42-52], and flight type robots (UAV: Unmanned Aerial Vehicle) [32-36,53-68] are mainstream. In addition, research and development of inspection functions is currently underway, mainly focusing on visual inspection and hammering tests that are conducted when performing regular inspection. In this research, in addition to visual inspection, specific inspection methods that enable the acquisition of information such as vibration or corrosion of steel bridges have been

investigated, and a method to implement these functions into a robot for robotic inspection has been proposed.

On the other hand, according to a report that investigated the reason for the renewal of steel bridges which underwent rebuilding in the past [68], the ratio of rebuilding due to damage to upper structures was confirmed to be five times higher than that of damage to lower structures. In addition, corrosion was found to be a major factor for rebuilding steel bridges, as corrosion of steel materials in upper structures accounted for more than half, 51.7%, of all cases. Regarding local corrosion, it is possible to repair corroded parts and consequently recover and improve performance. However, this is only temporary as corrosion progresses, especially when the corrosion of main structures is significant, and hence complete repair eventually becomes necessary. As the area for repair increases, so does the economic burden. Therefore, it is important to detect the existence and degree of local corrosion during periodic inspection and to carry out repairs while the damage is still minimal. Examples of local and minor corrosion include the generation of a rust layer, thinning of plate wall thickness and occurrence of holes in the various steel sections

Moreover, it has been made clear that corrosion damage lowers the load-carrying capacity of steel members [69-77]. Hence much research has been carried out by using the ratio of a designed thickness to a residual thickness to develop evaluation methods of the remaining load-carrying capacity [71-77]. Therefore, if it becomes possible to obtain the residual plate thickness of steel members during inspection, it will enable evaluation of the remaining load-carrying capacity, and thus be an effective inspection method for steel bridges.

1.2. Related Research

The robotic inspection proposed in this research is targeted for narrow areas such as truss panels and inside of box members, and locations that are difficult to access by inspectors. Therefore, the proposed robot must satisfy certain conditions, namely, it moves by self-propulsion, it can move along surfaces made of various materials, surface conditions and angles, and it can make turnings of small radii. The proposed robotic inspection intends to cover not only simple visual inspection, but also be able to determine structural performance and evaluate corrosion damage. Therefore, in addition to the wall-climbing robots and inspection systems using UAVs that are currently attracting much research attention, inspection methods for corrosion damage which causes serious damage to steel bridges were investigated through following related research. The applicability of these methods to robotic inspection is discussed.

1.2.1. Inspection System of Structures using Wall Climbing Robots

Wall climbing robots need to attach and move on surfaces to access target sections. There are various surface attachment systems of robots. For example, robots that are capable of attaching to only steel surfaces use magnet [43], permanent magnets [44,45] and electromagnets [46]. For application to other materials, there are mechanisms such as using electrostatic film [47,48], passive suction cups [49], negative suction cups [50,51] and suction cups with decompression fans [52]. These mechanisms can attach to surfaces irrespective of the material, and the suction force depends on the surface roughness. There are also a variety of movement methods, such as robots that move with tires, are crawler type or are piston type. Except for the piston type robots, a motor is necessary and so it likely that the robot body becomes heavy. Also, the crawler type and the piston type robots only allow forward and backward motion, and so it is sometimes difficult to change the direction of the robot.

Currently, although there are not many robots with inspection functions, Wang et al. [43] developed a robot that attaches to and inspects steel surfaces using a magnet wheel (**Figure 1.3**). For attaching to surfaces, electricity is sent to the magnet wheels to magnetize them and the magnet wheels are then moved by motors. The magnet wheel shown in **Figure 1.3** not only attaches the robot to the steel surface but also magnetizes the steel surface. Therefore, as the robot attaches to the surface, cracks located near the surface can be detected by the magnetic flux leakage method using a GMR sensor, which is a thin element that works in a similar manner to the coil in eddy current testing. This method can identify surface layer flaws, which is one type of corrosion damage that seriously damages steel bridges, thus it can be considered as a useful robotic inspection function.

Iwamoto et al. [52] developed a robot that can inspect concrete slabs or vertical concrete walls using the impact echo method. The developed robot is capable of exploring vertical and ceiling surfaces by wireless control. The robot attaches to surfaces by bringing the inside of the suction cup close to a vacuum state using a decompression fan (**Figure 1.4**). For movement, it adopts a mechanism that uses a belt and a DC motor. Furthermore, a CCD camera is installed for visual inspection, an impact hammer and a microphone is installed for hammer sound inspection and measurement data is then recorded and stored in a PC by a wireless LAN.

1.2.2. Inspection System of Structures using Unmanned Aerial Vehicles

To perform inspection of highway bridges, after lane regulation, visual inspection is carried out by an inspector using a special inspection vehicle. The time period for lane regulation is limited, and so the inspection range is limited to about 300 meters per day [29]. Under such circumstances, inspection of bridges using UAV, which can acquire a lot of data simultaneously, gained particular attention, and so research and development is actively underway in this domain (**Figure 1.5**) [60].

Inspection by UAV is mainly performed by taking a photograph of an entire bridge and obtaining information such as surface cracks, and then flying to target areas and carrying out visual checks using an attached camera [55-57,59-61].

Photchara et al. [54] attached electromagnets to parts corresponding to the legs of the UAV, and developed a robot that could both fly and attach. This robot was developed assuming that the hammering test is performed once the robot has reached the target area for inspection by flying and then attached to the target area using electromagnets. However, the body of the UAV is large hence it is difficult to approach locations with complicated structures. In addition, being able to resist the reaction force in hammering tests by the suction force of UAV is another challenge. Nonetheless, this robot, which is capable of both flight and attachment, can achieve large changes in inspection position by flying.

NEXCO East Japan conducted a demonstration flight of a "fully automated robotic aerial birds-eye view photographing system" using a UAV. A small UAV, originally developed for military use that takes off vertically with four rotors was used for the demonstration. This UAV was produced to quickly confirm the location of disaster occurrence following the lessons learnt from roads that suffered damage due to the Great East Japan Earthquake and due to the occurrence of landslides. The demonstration flight was carried out as a verification experiment based on the idea of installed system was carried out based on the idea that it can be used daily for bridge inspection [20]. With this UAV, it is also possible to confirm the condition of bridges by using the movies or images taken by the attached camera, and to create a map using the obtained images. For map creation, the UAV automatically takes shots of a specified range. Since location information is also stored at the time of photographing, UAV is also applicable to photogrammetry. Even in other organizations such as NTT Facilities Research Institute [51], the development of inspection technology using UAV is underway.

As a summary of inspection robots, current inspection robots tend to equip camera for visual inspection but not many inspection robots have several inspection devices. In addition, UAVs need to consider about flight control, and the influence on hovering due to wind. In this research, aiming to achieve effective and efficient inspection for steel bridges, in addition to visual inspection other inspection methods such as vibration measurement or corrosion damage evaluation are also considered investigating. To achieve the inspection, wall climbing type robot was selected considering wind influence, performing vibration measurement and corrosion damage evaluation. Hence, it is preferable to choose attachment methods which can be applied to surfaces irrespective of materials, and to have good contact with surfaces. It is also important to take measures against potential damage to the inspection site surroundings. To perform visual inspection, vibration measurement, and corrosion damage evaluation without influenced by

surface conditions, robots own vibration, and wind, in this research, especially attachment system has focused.

1.2.3. Method to Inspect Corrosion Damage on Steel Members

For corrosion damage inspection, application of ultrasonic testing [78-81] and eddy current testing [79,82] has been progressed since measurement methods which are able to obtain residual thickness by measuring from only one side of steel members are gained high demand. Ultrasonic testing requires preliminary surface treatment due to the need for measurements taken in direct contact with the target surfaces. Furthermore, the measurement time for ultrasonic testing, which can last anywhere between several minutes to just under one hour is another problem [81]. On the other hand, for residual thickness measurement of steel members, it has been reported eddy current base methods that remote field methods [83-85] and Pulsed Eddy Current (PEC) testing [81,86-96] can eliminate preliminary and post-treatment of target surfaces. In remote field methods, the penetration depth of eddy current is increased by using a relatively low frequency with an eddy current testing of about 1000 Hz, and the interval between excitation and the detection coil is increased to efficiently detect changes in the eddy current produced by the ferromagnetic material. Additionally, surface or near-surface cracks in steel materials can be detected using PEC testing [86-88] which includes a wide frequency range and can instantaneously create a large magnetic field [89]. Furthermore, it has been found that the PEC testing method can be applied for the measurement of steel thickness [90-93], and the detection of piping corrosion under insulation material [94]. However, in the aforementioned methods using eddy current, relatively large power consumption and the need of large equipment may be a difficulty during field measurements. Although the use of small probes has also been investigated, there are still problems that it is difficult to detect a detailed damage conditions such as the actual thickness range that can be measured being small, and a thickness reduction due to local corrosion.

In addition to establishing an independent inspection method, a corrosion damage evaluation method has been considered in this research as one of the inspection functions of the developed robotic inspection method. Hence the aim is to establish a method with a simple measurement system using a small probe that can acquire local information such as thickness reduction, and that can easily be installed onto a robot.

1.3. Purpose and Objectives

Inspection of steel bridges can be very challenging since there are many sections that are narrow or difficult to access by inspectors. One option which can be considered to solve these difficulties

is inspection by using a robot. The purpose of this research has thus been to develop a robotic inspection method where a self-propelled robot is used to reach target sections of steel bridges and successfully perform inspection. Firstly, a self-propelled inspection robot that can freely attach and move on various types of surfaces has been developed to perform simple and effective inspections. Next, inspection functions for robotic inspection system have been proposed, and the performance of robotic movement and all the inspection functions have been experimentally verified. In addition to robotic inspection, a corrosion damage evaluation method especially for use on steel bridges has been proposed and its performance has also been investigated. The proposed corrosion damage evaluation method can perform as both an independent measurement method as well as one of the inspection functions of the developed robotic inspection system. Since obtaining corrosion damage information is important for steel bridges, the proposed corrosion damage evaluation method is considered to be an effective and efficient inspection method that can be used independent of the inspection robot. The conceptual image of the proposed robotic inspection for steel bridges in this study is show in **Figure 1.6**. In the proposed robotic inspection, "Access" and "Measurement" are key words where "Access" includes movement and observation of various surfaces and "Measurement" indicates measurement using various sensors. The robotic inspection is expected to complement regular inspection and detailed inspection and it is also expected to expand locations where inspection can be performed. To achieve the purpose of this research, the three main research objectives considered are as follows:

I. Development of a mobile robotic inspection device which can move on various surfaces and access locations difficult for inspectors.
II. Investigation of robotic inspection functions for observation and various measurements.
III. Proposal of an efficient corrosion damage evaluation method.
    - An independent inspection method (General inspection)
    - One of the robotic inspection functions (Robotic inspection)

1.4. Outline of this Dissertation

The research objectives are discussed in three main chapters, Chapters 2 to 4. Outlines of all chapters are shown below (**Figure 1.7**).

Chapter 1: Introduction

Background, purpose and objectives and related research have been discussed. In this

research, an inspection method applying a robot which can be considered one option to achieve an effective and efficient inspection, and a method to acquire and to evaluate corrosion information are investigated.

Chapter 2: Development of a Self-Propelled Inspection Robot for Bridges

In order to develop a self-propelled inspection robot that is applicable on several types of surfaces and surface conditions, an attachment system using air pads for the robot was thoroughly investigated. Moreover, a gap coefficient, which is the average gap height between the air pads and target inspection surface, was defined to evaluate the attachment condition of the robot. A new type of air pad was also proposed in this chapter to improve the attachment condition, namely, to reduce the gap between the air pads and target inspection surface.

Chapter 3: Capabilities of a Robotic Inspection System

The proposed robotic inspection was attempted to cover both visual inspection and other measurements such as vibration measurement. Moreover, when the inspection robot works at sections invisible such as closed box section, it is important to understand robot location. To acquire the location of the inspection robot, identifying the location of the inspection robot and making a map of the robotic movement was also proposed using the images taken by attached camera used for visual inspection.

Chapter 4: Proposal of Corrosion Damage Evaluation Method

In order to detect the thickness of rust layer and the residual thickness of corroded steel members, a corrosion damage evaluation method applying eddy current testing techniques has been newly proposed and developed. This corrosion damage evaluation method aims to act as both an independent measurement system and as one of the robotic inspection functions. Therefore, a method to install an eddy current probe to the inspection robot was also investigated, and the performance of the corrosion damage evaluation method was clarified using a corroded steel specimen.

Chapter 5: Conclusions and Recommendations

The results of each chapter are summarized in this chapter. Based on the findings obtained in this study, recommendations for versatile robotic inspection and practical use of the corrosion damage evaluation method are proposed.

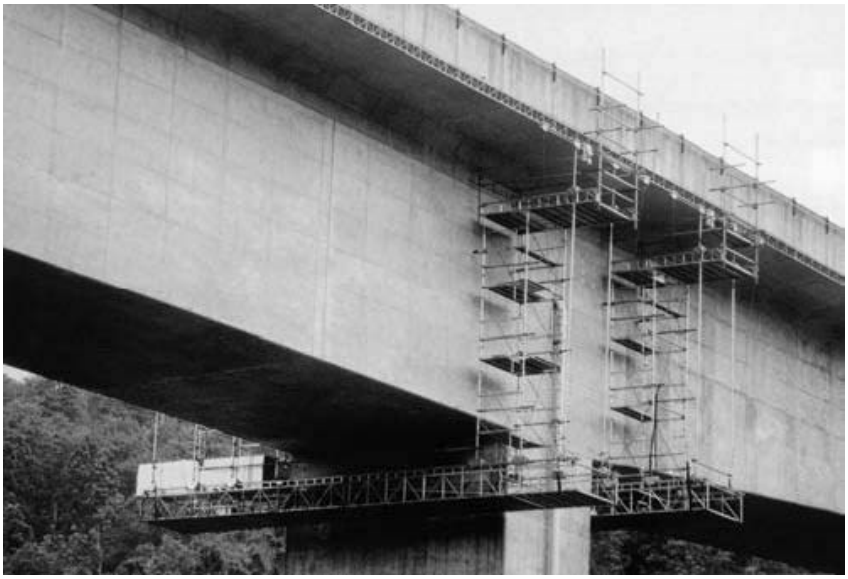

Figure 1.1 Examples of inspection using large-scale facilities [28]

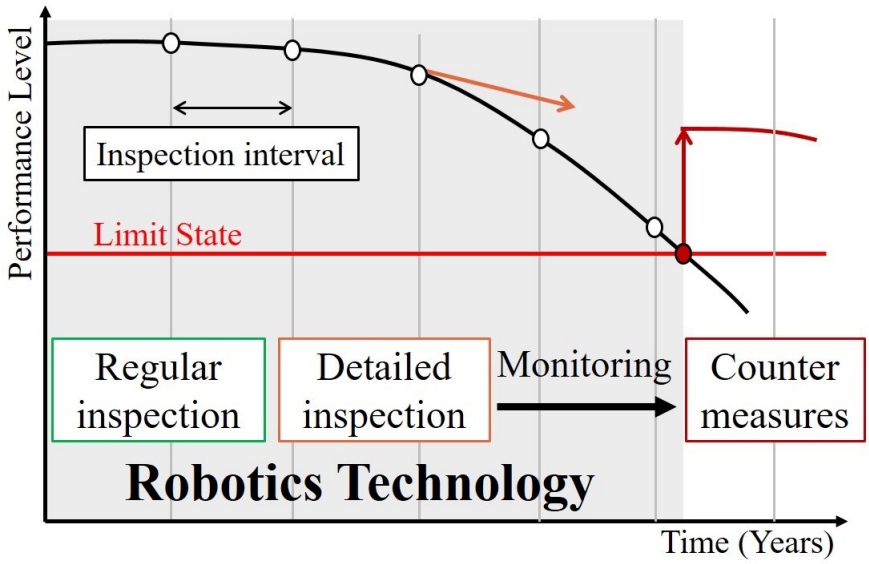

Figure 1.2 Relationship between basic inspection processes and potential robotic inspection

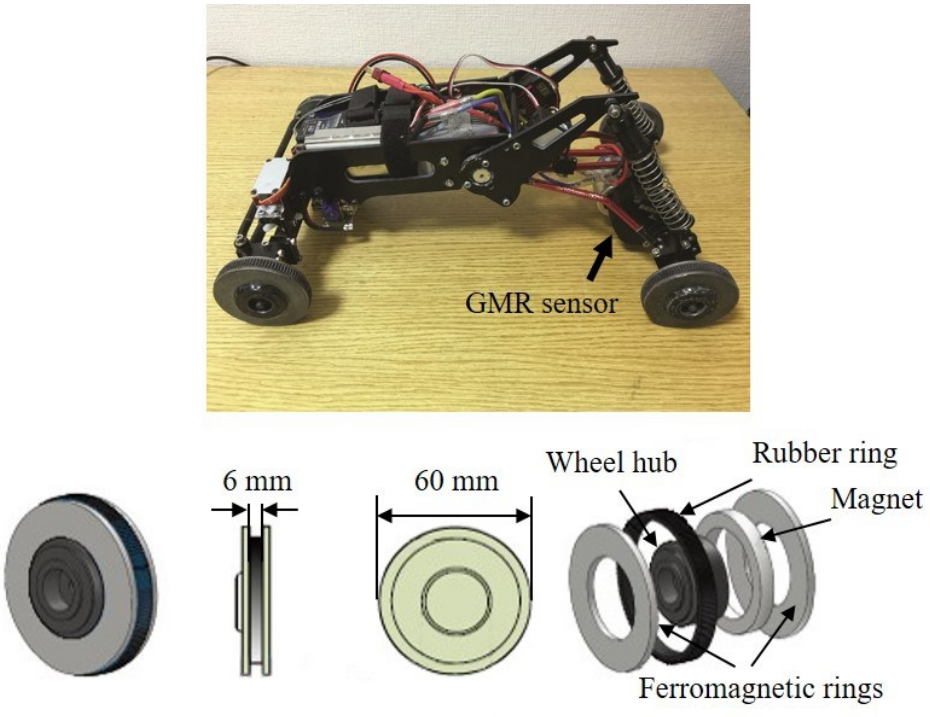

Figure 1.3 Inspection robot with a magnet wheel [43]

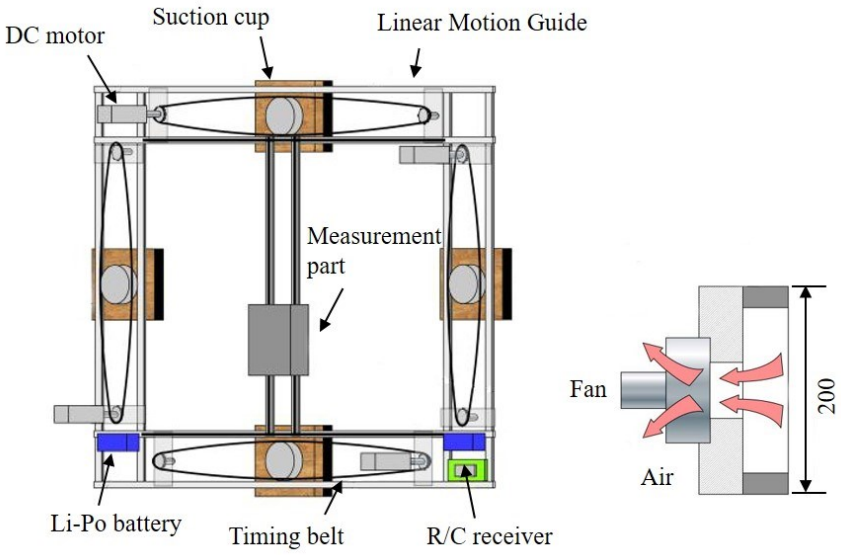

Figure 1.4 Inspection robot with suction cups [52]

Figure 1.5 Application of UAV for inspection [59]

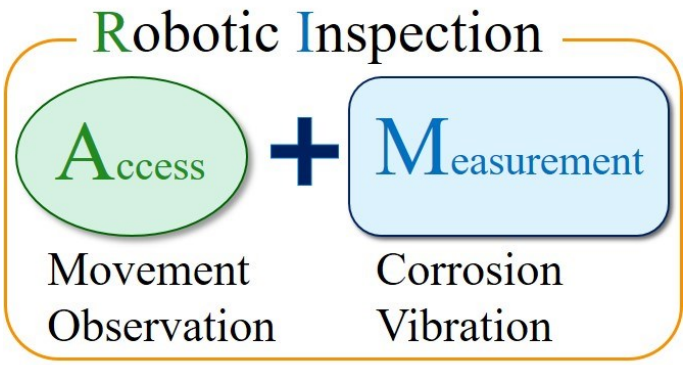

Figure 1.6 Conceptual image of robotic inspection in this study

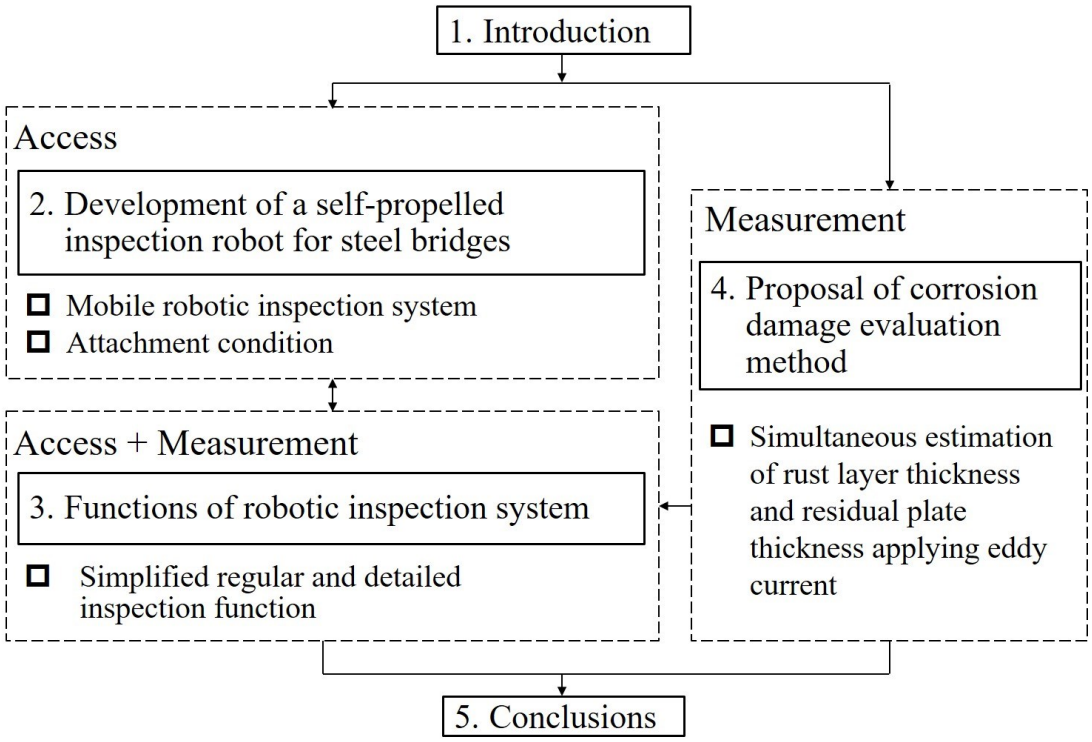

Figure 1.7 Flow of this dissertation

Chapter 2

Development of a Self-Propelled Inspection Robot for Bridges

Abstract

In this research, an inspection method using a robot has been investigated. The aim is for the robot to effectively access target sections of bridges, such as areas that are either narrow or difficult to reach by inspectors, and then perform inspection using various attached devices. A self-propelled robot has initially been developed in this chapter. Steel bridges are the target of this research, however, they are not only made of steel components but also comprise concrete or other materials. Therefore, the robot must be able to move on numerous surfaces under various conditions. In this chapter, the attachment system of the robot has been the main focus to enable movement on various surfaces under a range of conditions.

2.1. Overview

Bridge maintenance has gained much attention in the field of civil engineering. Especially for steel bridges, which consist of steel and concrete sections, acquiring information such as steel deck corrosion, concrete deck cracks, and changes in vibration characteristics due to deterioration is particularly important. However, the complicated structure of bridges makes inspection difficult. One option to achieve aforementioned inspection can be considered robotic inspection. Consequently, robotic inspection has recently gained much interest as an increasingly important part of bridge maintenance procedures. However, at narrow sections such as truss components or internal closed sections of steel box girders incur significant inspection cost and effort when inspection must be performed continuously. These factors make inspection complicated, and there are further problems including the difficulty to secure enough personnel or inspection equipment. Considering these factors, if a robot could move across both steel and concrete parts and inspect sections that are narrow, difficult to access or even invisible for inspectors, performing inspection would become easier and more cost effective than conventional inspection methods.

In this chapter, a self-propelled inspection robot hereafter, referred to as inspection robot with the ability to move on various surfaces and angles was initially built. It was then developed further with the aim to achieve effective bridges maintenance within a limited budget, and perform inspection without the need of scaffolding or large inspection passages for inspectors. It is considered to be able to apply also for concrete bridges. Moreover, the attachment system of the inspection robot has been thoroughly investigated. In this research, air pads which can attach to surfaces by their inside being made into a vacuum state were selected for the robot so that it can attach to several surface conditions irrespective of the material. Furthermore, an evaluation method for the suction condition has been newly developed, by considering that the vacuumed air flow can estimate the attachment condition of the inspection robot. Finally, after numerous improvement processes, performance tests and robotic movement tests were carried out at various locations.

2.2. Concepts of the Inspection Robot

To begin with, there are several expectations of robotic inspection. Examples include that the robot can perform inspection at sections that are difficult for inspectors to access, as well as perform low cost and easy to schedule inspections without scaffolding.

Sections need of inspection are made of various materials, mainly steel and concrete in steel bridges, and so the inspection robot needed to be able to attach and move on such surfaces also.

The proposed robotic inspection is namely, to approach a target section by robot and to then perform several inspections. Moreover, establishing a method to obtain damage information such as the corrosion or deterioration condition of the bridge through visual inspection, vibration measurement and corrosion damage evaluation has been considered. In addition, most of the aforementioned narrow sections are invisible for inspectors and it is therefore important to obtain location information of the robot. It is also important to obtain such location information when inspectors find cracks or corrosion to accurately determine damage locations which can then also be used for consequent inspections.

To perform not only visual inspection, but also vibration measurement and corrosion damage evaluation, the inspection robot needs to have good contact with surfaces so that it does not influence its own vibration. Therefore, the most important point to apply wall climbing type robot to inspection can be considered attachment condition. The inspection robot is also not intended to perform inspection of an entire bridge but of locations where damage is expected or locations where it is difficult to approach by inspectors. Concretely, since robotic inspection is able to perform measurement in addition to visual inspection, it is expected to complement of regular inspection and detailed inspection. Furthermore, it is expected to make it possible to inspect locations such as high places, closed sections or narrow sections where inspections have been considered difficult (that is, expansion of the inspection place). In addition, the inspection robot is considered able to determine the degree of damage progress by performing inspection periodically at the same location. Considering these facts, the requirements of the inspection robot were determined as shown in **Table 2.1**. Functions of the robot to satisfy the requirements will be explained in the following chapters.

2.3. Development of a Movement System, a Surface Attachment System and a Prototype Inspection Robot

In this research, five prototype robots as shown in **Table 2.2** were initially built. Each robot applied improvements such as changing materials of the inspection robot, shape of the inspection robot or method of making vacuumed state. Finally, the fifth version was selected as the inspection robot to satisfy the requirements as shown in **Table 2.1**. Main reasons that the inspection robot can achieve good contact and self-propelled movement are considered improvement of attachment method, enough suction force, and its weight. Air pads were selected to attach the inspection robot to surfaces irrespective of surface materials (**Figure 2.1**). The air pads have a similar surface attachment system to vacuum suction cups, however in this research, an air pump which can provide vacuumed air directly to the air pads has been used instead of a fan to create a

vacuumed state. By using air pads and an air pump, there is no need for additional parts such as a fan to be attached to the air pads, hence the leg part of the robot can be made simple and light, and a more stable vacuum state can be sustained. After the fifth prototype robot was built and selected, several improvements were made to the robot, and inspection devices were then installed to create the proposed inspection robot for this research. The body of the inspection robot is made of polycarbonate, which is a useful plastic for applications that require high impact resistance, and its use enabled the robot to become lightweight and durable. To consider the narrow sections, finally the size of the robot body without inspection devices is (W) 153 mm × (L) 148 mm × (H) 60 mm and its weight is 327.5 g. It is considered to be able to apply at narrow sections such as truss components or hand hole of closed box girders. The plan view and appearance of the inspection robot are shown in **Figures 2.2** and **Figure 2.3** respectively.

The proposed inspection robot was built considering simple control system, therefore, a micro sequencer which can provide “on” and “off” signal to control all movements is selected. Moreover, air pump is selected to use to make vacuumed state of air pad thus, air tubes are required on the inspection robot. Consideration of simple control system and required air tube, the robot is considered to be regulated by wired control. It is considered important to guarantee the safety of the roads under the bridges that are being inspected. In case of the proposed inspection robot, the attached cables would keep the robot suspended from the bridge if it robot accidentally fell down while performing inspection. Hence using wired control robot with attached cables can prevent damage to the area under the inspection site. Then finally, the inspection robot was proposed with four components; robot body, air supply part, control part and an inspection part. The air supply part consists of an air compressor and an air pump to supply compressed and vacuumed air to the robot body, as shown in **Figure 2.4(a)**. The control part consists of a micro sequencer and a controller, to control the robotic movement and devices for inspection as shown in **Figure 2.4(b)**. The inspection part consists of a Charged Couple Device (CCD) camera to perform visual inspection, plus other cameras to view the surrounding areas, and an accelerometer to determine structural performance as shown in **Figure 2.4(c)**. Specifications of the devices used in the robot body, control part, air supply part and inspection part are defined in **Table 2.3** to **Table 2.6** respectively. The inspection devices were selected with consideration of applicability and their size. If the inspection devices are small, other inspection devices could be additionally installed onto the robot, or used to replace existing inspection devices to enable other types of inspection. The robot body and inspection parts are connected to the control part by cables, which can currently extend to 10 meters. It was decided as the length that it can be inspected members such as stringer or cross beam at one time. Therefore, inspectors are able to control the robot from a safe distance, without putting themselves in any danger, while viewing the images from the inspection cameras to examine specific areas in real-time. An

additional inspection function, namely a corrosion damage evaluation method using an eddy current probe, has been investigated in Chapter 4.

The main unique feature of the proposed inspection robot is that it is able to attach to various surfaces. It does so by using six air pads, and it moves by the expansion and contraction of the air cylinder piston rods. It is therefore possible for the inspection robot to move along surfaces with various materials, angles, and roughness, without the need of special rails, as required by inspectors. In addition, the inspection robot is relatively small and lightweight and is also tightly attached to the surface by air pads, thus it is difficult for the inspection robot to be affected by wind.

2.3.1. Movement System of the Inspection Robot

The proposed robot is made of two separate parts hereafter called the upper part and the lower part as shown in **Figure 2.2**. In this system, the bodies of the air cylinders are fixed onto the upper part and the piston rods are fixed onto the lower part. The lower part advances when the piston rods expand. On the other hand, the upper part advances when the piston rods contract. Moreover, the robot has a movement mechanism that moves up and down (**Figure 2.5**) according to whether the air pads are or are not attached to the surfaces as shown in **Figure 2.6**. This mechanism allows the inspection robot smooth movement regardless of friction force which influences to the air pads movement and will be explained following section. When an air pad is said to be “attached”, it means that the inside of the air pad is made into a vacuum state by the air pump. Solenoid valves are used for the robot to control the air cylinders and air pads by sending “on” and “off” signals from a micro sequencer. This technique allows the movement system to become simple. The air pads attach to a surface and the air cylinders cause the piston rods to contract when the solenoid valve sends them an “on” signal. The electronic equipment used, such as the solenoid valves and air cylinders are shown in **Figure 2.7**. There are two types of solenoid valves in this research. One is for compressed air to send signals to the air cylinders and the other is for vacuumed air to send signals to the air pads. The piston rod of the air cylinders is 20 millimeters thus in theory, the robot should be able to move 20 millimeters in one movement and whether this is the case or not has been examined.

The designed movement system allows the inspection robot to move forward, retreat and also rotate. **Figure 2.8** shows one cycle of the movement system for forward motion. The colored air pads indicate that they are attached, and the uncolored air pads indicate that they are not attached. Forward movement composes of three steps; standby, upper part advances, and lower part advances. First, air pads of both the upper and lower parts are attached to the surface, and the piston rods of the air cylinder are expanded (Step 1). Next, the air pads of the upper part detach from the surface by sending the air pads of the upper part an “off”-signal to release them from the

vacuum state. The upper part then advances by contracting the air cylinder piston rods (Step 2). The lower part advances by attaching the air pads of the upper part but not lower part to the surface, by expanding the air cylinder piston rods. Finally, the robot returns to standby by attaching the air pads of the lower part to the surface (Step 3). When the advance button of the controller is pressed continuously, the motion of Step 1 to Step 3 is repeated. For retreat motion, the steps of forward motion are simply reversed.

Figure 2.9 shows one cycle of the rotation motion system in the right-hand direction. Rotation motion composes of five steps; standby, lower part retreats, lower part rotates, upper part rotates, and lower part advances. First, air pads of both the upper and lower parts are attached to the surface by suction, and the air cylinder piston rods contract (Step 1). The lower part then retreats by removing the suction of the air pads of the lower part and contracting the air cylinder piston rods (Step 2). The lower part can then rotate approximately 10°, by expanding the left hand air cylinder piston rod (Step 3). The upper part can then rotate approximately 10° by attaching the air pads of the lower part but not upper part to the surface by suction, and by contracting the left hand air cylinder piston rod. (Step 4). The lower part advances by expanding the air cylinder piston rods, and finally, the robot returns to standby by suction of the lower part air pads (Step 5). When the right rotation button of the controller is pressed continuously, the motion of Step 1 to Step 6 is repeated. During left rotation motion, right and left are reversed in the aforementioned steps.

2.3.2. Investigation of Attachment Method using Air pads and Improvement Process of the Suction Condition

In this research, a method to enable a self-propelled inspection robot to attach to surfaces of various angles or roughness has been developed initially. The proposed inspection robot attaches to surfaces using air pads, hence the suction force of the air pads is the most influential factor for inspection such as vibration measurement when dealing with surface angles or conditions. In general, using larger diameter air pads increases the suction force. However, if there is a gap, air leakage increases, which lowers the suction force. The balance between suction force and air leakage, and the dead weight of the robot need to be considered to improve the suction force. In this study, in particular, an air pad having a strong suction force and a small air leakage was selected. The suction force is a particularly important factor in the use of air pads, so evaluation method of suction force will be discussed in the following section.

Air pads are mainly used for transporting products and machinery in factories hence there are many types of air pads with different shapes or materials according to their various purposes. In this research, bellows type air pads have been selected for the attachment part of the robot. Bellows type air pads are considered adaptable to surface conditions with little constraint on the

movement range and can be expanded and contracted vertically according to the required suction condition. Two types of material with different hardness were selected for the air pads, namely elastodur and nitrile rubber as shown in **Figure 2.10**. The specifications for air pads made of both materials are shown in **Table 2.3**.

Nitrile rubber is harder than elastodur, and so the movement of the robot can be made more stable. However, on rough surfaces such as concrete or corroded steel, nitrile rubber was not able to have good contact due to the poor surface condition and so the suction force reduced. For this reason, elastodur air pads, was initially selected. Although the attachment condition of the elastodur air pads to concrete surfaces or other rough surface conditions was better than the nitrile rubber air pads, the edge of the elastodur air pads rolled up due to the softness of elastodur and due to the friction force between the air pads and surface as shown in **Figure 2.11**. It was confirmed that the suction force reduces due to this phenomenon and so air pads made of nitrile rubber, which had greater hardness and stability for robotic movement than elastodur was investigated. Attachment to rough surfaces, which was considered to be a problem for nitrile rubber air pads, was solved by attaching a chloroprene rubber sponge to the suction part of the nitrile rubber air pads as shown in **Figure 2.12**. A chloroprene rubber sponge was selected to further develop the nitrile rubber air pads as it contains bubbles and is thought to be able to change shape corresponding to the surface conditions. Using a chloroprene rubber sponge alone cannot support the weight of the robot, however the proposed nitrile air pads with chloroprene sponge, named hereafter sponge bellows air pads, can support the weight of the robot by using the expansion and contraction feature of bellows type air pads. As shown in **Figure2.12**, in order to restrict the movement of the sponges, a support material has been embedded and glued inside of the sponges. Taking into consideration the potential of air leakage in the sponge part, the minimum height required for attachment, without compromising the adhesion strength, was determined through experiment. **Figure 2.13** shows the attachment condition of the sponge bellows air pad.

By using sponge bellows air pads, an attachment system has been developed to enable the robot to move across various surfaces with many different surface conditions, except damaged surfaces such as those with large cracks or peeling corrosion. However, although the inspection robot has a movement mechanism that moves up and down according to whether the air pad is or is not attached to the surface, friction wear has been confirmed since the sponge is weaker against friction force than the elstodur air pads. As the friction wear of the sponge progresses, the suction force decreases and this was considered to influence the movement of the robot Therefore, further improvement to the air pads was examined.

There are various materials for the sponge as well as the air pads, and so a silicone sponge which is more resistant to abrasion and has finer bubbles than a chloroprene rubber sponge was considered to improve the attachment condition of the robot. First, silicone rubber has a higher

hardness than chloroprene rubber and has better durability. It was also confirmed through experiment that air leakage at the sponge section was also reduced due to the finer bubbles of silicone rubber. In addition to changing the sponge material, the shape of the inner support attached inside of the sponge was also changed, as shown in **Figure 2.14**, to make the suction state more efficient and stable. The height of the inner support shown in **Figure 2.14** was also made higher and the size of the support holes was made bigger to maintain a suction state more effectively than the previous sponge bellows air pads. While there are many advantages of using silicone sponge bellows pad that have fine bubbles and high hardness, named hereafter silicone bellows air pad, especially for use on smooth surfaces it was established that smooth movement was sometimes prevented due to friction or surface moisture. Sponge bellows air pads using chloroprene rubber sponges and silicone bellows air pads have different characteristics on different surface types. Therefore, sponge bellows air pads and silicone bellows air pads can be selected according to the surface condition of the target inspection location.

By selecting the type of air pad accordingly, the robot is able to move on various surfaces such as corroded steel, outside concrete walls or even ceilings as shown in **Figure 2.15** to **Figure 2.17** respectively. If sponges are not attached to the air pads, friction wear occurs at the attachment surface of the air pads directly. Since the cost of air pads is relatively higher than sponges, using sponges can be assumed to be an advantage as sponges can be replaced immediately with low cost and ease if friction wear is discovered.

2.3.3. Definition and Quantitative Evaluation Method for Evaluating the Attachment Condition of the Proposed Robot

The most important thing when using air pads is evaluating the suction state, as this is considered the attachment condition of the inspection robot. During the performance test of the air pads, the suction state and robotic movement on various surface conditions such as mortar or exterior concrete walls have been confirmed. In this research, twelve different types of surface were selected as target surfaces for the inspection robot. The target surfaces are shown in **Figure 2.18**. They are made of either steel or concrete with corrosion, cracks or peeling present.

In this subsection, a quantitative evaluation method of the suction state of the inspection robot has been examined. Therefore, with reference to formulas for calculating the air flow rate and effective cross sectional area of the air tube used when selecting the vacuum pump, a gap coefficient, which is the average height between the air pads and surfaces, has been defined. Furthermore, by using the calculation for the gap coefficient, it is also possible to calculate the suction force of the air pads. To obtain the gap coefficient for each surface, experiments which measure the negative pressure of the air pump when one air pad is attached to a surface have been carried out. Schematic image of deterring the gap coefficients are as shown in **Figure 2.19**. In this

figure, S' and S_0' indicate the effective sectional area between the air pump and the air pad when the air pad is or is not attached to surfaces respectively , a' indicates the effective sectional area between the air pad and surfaces, and t indicates the gap coefficient. As a result of the experiments, the suction state could be classified into three levels using the gap coefficient as follows:

(1) g < 20 μm (Complete attachment and movement);
(2) 20 ≤ g < 60 μm (Attachment and movement: conditional);
(3) 60 ≤ g μm (Impossible to attach).

The second level indicates that the robot can move across surfaces, however, the possibility of it falling down increases as the gap coefficient nears 60 μm. Based on the flow characteristics of air pumps, the flow of vacuumed air can be expressed as:

$$Q = Q_{max} * \frac{P_{base} - P_p}{P_{base}} \tag{2.1a}$$

$$Q_0 = Q_{max} * \frac{P_{base} - P_{p0}}{P_{base}} \tag{2.1b}$$

where Q_{max} is the maximum flow of vacuumed air of the air pump. In this research, an air pump with Q_{max} of 90 [l/min] has been used. Q is the flow of vacuumed air when the air pad is attached to surfaces by suction and Q_0 is the flow of vacuumed air when the air pad is not attached to surfaces, namely opened condition. P_{base} is the base pressure of vacuumed air and P_{base} of 0.1 [MPa] is generally used. The pressure of vacuumed air when the air pad is attached to surfaces P_p [MPa] and the pressure of vacuumed air in the open condition P_{p0} [MPa] were obtained from experiment. S′[mm^2], which is the effective sectional area between the air pump and the air pad which is attached to surfaces, and S_0' [mm^2], which is the effective sectional area between the air pump and the air pad in open condition, are given by:

$$S' = \frac{Q}{C_{airflow} * \sqrt{(P_{base} - P_p)P_p}} \tag{2.2a}$$

$$S_0' = \frac{Q_0}{C_{airflow} * \sqrt{(P_{base} - P_{p0})P_{p0}}} \tag{2.2b}$$

Where, $C_{airflow}$ [l/min·N] is coefficient of air flow and $C_{airflow}$ of 240 [l/min·N] is used. Moreover, S' can also be expressed by following equation:

$$\frac{1}{S'^2} = \frac{1}{S_0'^2} + \frac{1}{a'^2} \tag{2.3}$$

Using Equations (2.2a), (2.2b) and (2.3), α' [mm^2] which is the effective sectional area between the air pad and surfaces can be obtained as:

$$\alpha' = \frac{1}{\sqrt{\frac{1}{S'^2} - \frac{1}{S_0'^2}}} \tag{2.4}$$

Finally, the gap coefficient g [μm] can be determined as:

$$g = \frac{\alpha'}{\pi DN} \times 1000 \tag{2.5}$$

where N is number of air pads and D [mm] is the diameter of the air pads. By calculating the gap coefficient of a target bridge before performing inspection, it is possible to predict the suction state of the robot before performing inspection. However, it should be noted that the vacuumed air flow and effective sectional area are theoretical values.

The calculated gap coefficients of five example surfaces from **Figure 2.18** are showed in **Figure 2.20**. R_a is known as the average surface roughness and R_Z is known as the maximum surface height. These values are generally used to characterize surface roughness [98]. In this research, a laser displacement meter was used to obtain R_a and R_Z values for each surface. **Figure 2.20** shows the level of the suction state based on the gap coefficient. The gap coefficients of sponge bellows air pads and silicone bellows air pads were decreased compared with elastodur air pads hence the suction state has been improved. Therefore, using the developed sponge bellows air pads and silicone bellows air pads has proven to be highly effective.

A method to obtain the suction force F [N] using the gap coefficient t obtained by the above process is as follows. First, $\alpha'(D)$, which is the effective sectional area between the surface and air pads attached to the surface with a diameter D [mm], and $S'(D)$ [mm^2] which is the effective sectional area between the air pump and air pads which are attached to surface with a diameter D [mm] are given by:

$$\alpha'(D) = \pi g DN/1000 \tag{2.6}$$

$$S'(D) = \frac{1}{\sqrt{\frac{1}{\alpha'^2(D)} + \frac{1}{S_0'^2}}} \tag{2.7}$$

Moreover, the flow of vacuumed air when the air pads are attached to the surface Q can also be expressed by the following equation according to the theoretical formula.

$$Q = C_{airflow} * S'^2\ (D)\sqrt{(P_{base} - P_p)(P_p - P_a)} \tag{2.8}$$

From equation (2.8) and (2.9), the pressure of vacuumed air when all air pads are attached to the surface P_a can also be represented as follows:

$$P_a = P_p + \frac{Q^2}{{C_{airflow}}^2 * S_0'^2(D)(P_p - P_{base})} \tag{2.9}$$

Finally, the suction force in the vertical direction F_v can be represented as follows:

$$F_v = P_a * \frac{D^2}{2}\ \pi * N \tag{2.10}$$

Figure 2.21 shows the results of calculating the suction force of silicone bellows air pad using same surfaces as **Figure 2.20**. F_h in **Figure 2.21** is the suction force in the horizontal direction, and it is evaluated with a safety factor of 1/2 to F_v. The results show that although each type of air pad has a similar suction force on the smooth surface, on the rough surface, the suction force was six times higher using the sponge bellows air pads and twenty-five times higher using the silicone bellows air pads than using elastodur air pads. Hence using the proposed air pads enabled a significantly higher suction force on rough surfaces than using elastodur air pads. Therefore, these results indicate the effectiveness of using sponge bellows air pad and silicone bellows air pads over elastodur air pads. Namely, it has been confirmed that attaching chloroprene or silicone sponge to the attachment surface of the elastodur air pads is highly effective as it increases the suction force of the air pads. For example, limited wind speed for inspection is 10 to 15 meter per second and wind load for the inspection robot can be calculated approximately 9 N. From the view point of wind load, the inspection robot can be considered to have enough suction force. Moreover, it can be considered the inspectors can select applicable weight of inspection devices from suction force evaluation process. The wind load W (N) can be calculated by following equation [99];

$$W = \frac{1}{2}\rho_a U_d A_n C_D G_a \tag{2.11}$$

Where, ρ_a is air density [kg/m^3], U_d is wind speed [m/s], A_n is projected area [m^2], C_D is drag coefficient and G_a is gust response factor. In this calculation, ρ_a of 1.2 [kg/m^3], C_D of 1.6 and G_a of 1.9 have been used.

2.4. Performance Tests of Robotic Movement on Target Surfaces and an Existing Bridge

The proposed robot is able to move forward, retreat and rotate. Performance tests of robotic movement were carried out in three locations. First, target surfaces (**Figure 2.18**), second, at an existing steel bridge with significant corrosion, and third, at a trial bridge, (which is used for inspection training). These locations are also used for other performance tests in following chapters. The first performance test on target surfaces was carried out to evaluate robotic movement on various surface conditions. The performance tests on the existing bridge and the trial bridge were then carried out to better understand robotic movement on actual surface conditions. The existing bridge was assumed surface conditions of significant corrosion and the trial bridge was assumed general concrete deck.

The first performance test was on target surfaces. In this test, all three movements were performed and evaluated on all target surfaces. **Figure 2.22** shows one of the performance tests carried out on an exterior concrete wall. It was confirmed that the inspection robot could move on various surfaces such as concrete or corroded steel, and that it can move up to 400 millimeters per minute. It was also confirmed that the inspection robot is able to advance and retreat well on various surfaces, and moreover, rotate smoothly on various surfaces. Moreover, the performance of the robotic movement was barely affected by its weight or the elasticity of the cables.

A performance test was also carried out at an existing bridge with steel corrosion as shown in **Figure 2.23**. The existing bridge is a twenty-eight span simple through-truss bridge with a total span of 559.6 m, located in Japan sea side. It is currently limited to five tons of weight due to the presence of considerable corrosion hence there are plans to rebuild the bridge in a few years time.

To perform live robotic inspection, performance of robotic movement was tested to examine whether the robot can be used at sections that inspectors cannot reach, such as panel sections of truss members. In this performance test, the inspection robot was tested on a lower chord and a vertical member of a truss, as shown in **Figure 2.24(a)** and **(b)**. The results confirmed that the inspection robot could move in areas where corrosion was relatively minor. However, corrosion has significantly progressed in most areas of this bridge and some places showed peeling of the corrosion surface that has more peelings than case 2 or case 3 of **Figure 2.18**. The surface condition in these areas was far worse than the concrete walls used in experiment, and the peeling

of the corrosion surface lowered the performance of the robots movement. The poor surface condition created a greater gap between the air pads and the surface than when tested on concrete walls. Moreover, it was confirmed that the sponge section of the sponge bellows air pads became worn down by the peeling of the corrosion surface, and this promoted gap propagation between the air pads and the surface. Two cameras and a single accelerometer were attached to the front of the inspection robot t to perform live robotic inspection, but the weight of these devices was found to wear down the front air pads. It was confirmed that the inspection robot could attach and move even at significant corroded areas, however it required to solve the problem of wearing down the air pads. Therefore, silicone bellows air pads were proposed and examined.

The last is performance test was at a trial bridge which is used for inspection training. As the sponge part of the sponge bellows air pads were worn down in the previous performance test, silicone bellows air pads were proposed for use on rough surfaces such as those with significant steel corrosion peeling. The use of silicone bellows air pads was examined on the concrete deck of the trial bridge, which is currently no longer in use. This bridge is very old and now only used for training inspectors. **Figure 2.25** shows the inspection robot during the performance test on the concrete deck of the trial bridge. The surface condition of the concrete deck is also shown in **Figure 2.25**. As shown, the concrete deck consists of a rough surface with cracks. It was therefore considered to be useful for the performance test of silicone bellows air pads. The inspection robot with silicone bellows air pads was able to attach to the trial bridge surface and move without the sponges becoming worn down. Hence the results indicate that silicone bellows air pads are good for use on rough surfaces with cracks or corrosion peeling. Moreover, since it was raining at the time of the experiment on the trial bridge, robotic movement of the proposed robot on wet surfaces could also be examined. When using silicone bellows air pads, smooth movement was occasionally prevented as the friction between the air pads and the surfaces was too strong due to surface moisture. On the other hand, smooth movement was not a problem when using sponge bellows air pads on the same wet surface. Thus it can be considered that the two proposed air pads can be selected according to the condition of the surface that requires inspection, such as rough or wet surfaces. The finally, the attachment condition and performance of robotic movement were clarified through these performance tests.

2.5. Summary

In this chapter, fundamental investigations were conducted to clarify the attachment and self-propelled movement system of the inspection robot. An inspection robot which can move across various surfaces to carry inspection devices for robotic inspection has been developed in this

chapter. The developed inspection robot uses air pads to attach to various surfaces and air cylinders to move forward, retreat and rotate. The inspection robot has a movement mechanism that moves up and down according to whether the air pads are or are not attached to the surface, to enable smooth movement.

In this chapter, focus has been made on the attachment system, as the most important factor when using air pads is the suction condition. To evaluate the suction condition, a gap coefficient, which is the average height between the air pads and surface has been defined. Moreover, using this gap coefficient, a quantitative evaluation method for the suction state has been proposed. This suction state helps inspectors to estimate how well the inspection robot will attach to target bridges in advance of carrying out inspection.

To improve the attachment condition of the inspection robot, two new air pads were proposed. The gap coefficient of each air pad was obtained for twelve target surfaces. The results confirmed that the suction condition was improved by using the proposed air pads compared with using elastodur air pads, and that smoother movement could be achieved. Furthermore, use of the two air pads can be selected based on the surface condition such as roughness or moisture. Finally, performance tests of robotic movement were carried out on target surfaces in laboratory, at an existing bridge and at the trial bridge. These performance tests confirmed that robotic movement improved by using the proposed sponge bellows air pads and silicone bellows air pads.

In this research, fundamental function for self-propelled inspection robot was developed, which can make the inspection robot move on various surface of existing bridges. It is unsupported to places where is step and is an angle of the face changes so far, yet it is possible to cope with by changing the movement mechanism, for example changing the angle of the leg part of the inspection robot by the encoder.

Table 2.1 Requirements of inspection robot

Requirements	Functions for requirement
Ability to attach and move on various surface conditions, includes difference in materials, roughness, angles, without special rails	Attachment and self-propelled movement system with air pads and vacuumed air
Ability to obtain information of surface condition for observation in robotic inspection	Visual inspection function, crack detection function
An automatic identification system of robot location especially at invisible areas	Location identification function
Ability to obtain information of damage condition for measurement in robotic inspection	Vibration measurement, Corrosion damage evaluation
Small in size to inspect narrow sections	Miniaturization of robot body

Table 2.2 Developed five prototype robots

Ver.	Appearance	Size	Weight	Movement	Features
1		(L) 130 mm (W) 183 mm (H) 61 mm	720 g	Floor: Fail Wall: Fail Ceiling: Fail	Aluminum Elastdur air pad Compressive to vacuumed
2		(L) 130 mm (W) 183 mm (H) 51 mm	760 g	Floor: Ok Wall: Fail Ceiling: Fail	Nitrile air pad
3	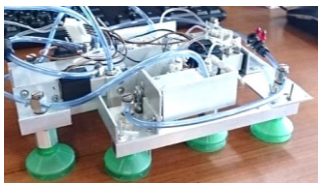	(L) 150 mm (W) 210 mm (H) 66 mm	624 g	Floor: Ok Wall: Smooth surfaces Ceiling: Fail	Elastdur air pad Movement mechanism
4	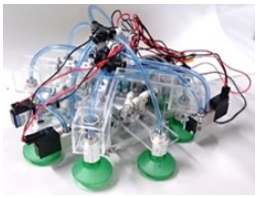	(L) 170 mm (W) 200 mm (H) 66 mm	563 g	Floor: Ok Wall: Smooth surfaces Ceiling: Fail	Polycarbonate Robot shape
5		(L) 148 mm (W) 153 mm (H) 60 mm	328 g	Floor: Ok Wall: Ok Ceiling: Ok	Vacuumed air directly supply Number of air pads

Figure 2.1 Appearance of several types of air pads

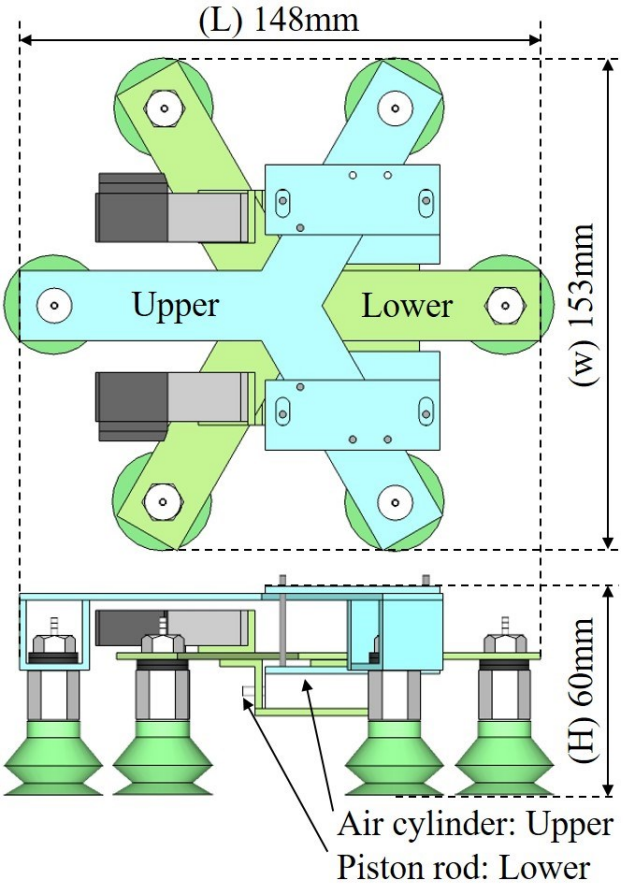

Figure 2.2 Plan view of proposed inspection robot

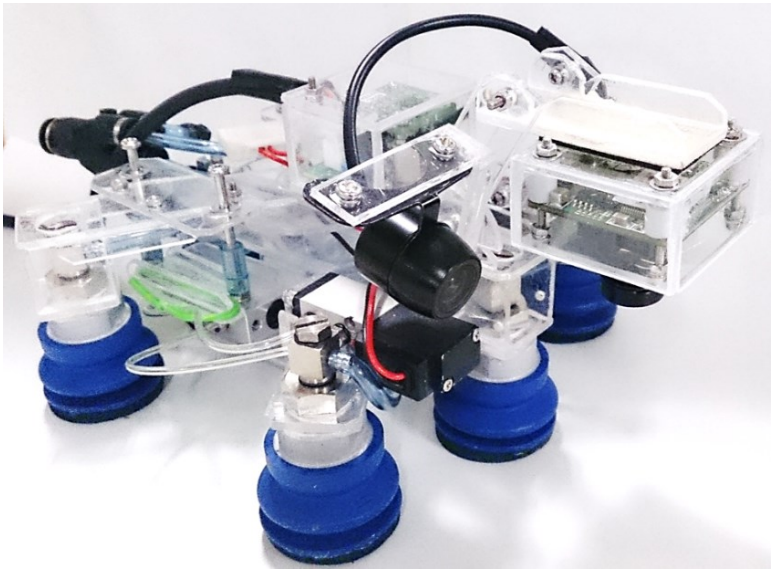

Figure 2.3 Appearance of proposed inspection robot

(a)

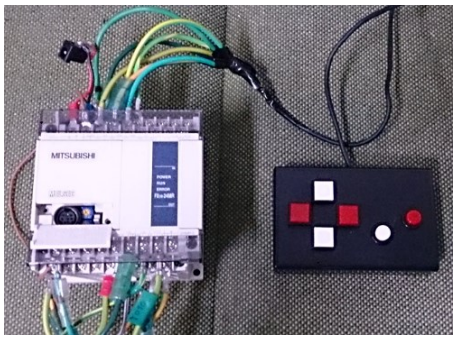

(b)

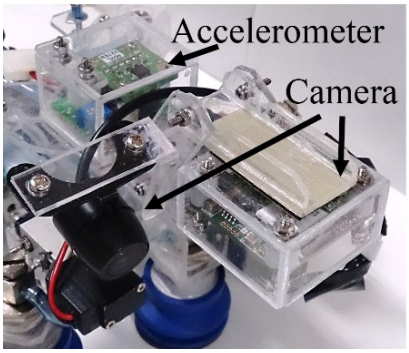

(c)

Figure 2.4 Composition of proposed inspection robot, (a) Air supply part, (b) Control part, (c) Inspection part

Table 2.3 Specification of devices in robot body

Basic information	Size	(L) 148 mm (W) 153 mm (H) 60 mm
	Weight	327.5 g
	Material	Polycarbonate
Air pad	Rubber material	Elastodur / Nitrile rubber
	Shore hardness	65 / 70
	Size	φ 31.4 mm /φ 32 mm
	Weight	8 g / 5.5 g
Solenoid valve	Number of positions	2 positions
	Number of ports	5 ports
	Valve function	Single solenoid
	Size	(W)10 mm×(L)43.5 mm×(H)14 mm
	Weight	20 g
	Applicable fluid	Air
	Actuation technology	Internal pilot
	Connection caliber	M3×0.5
	Oiling	-
	Withstanding pressure	1.05 MPa
	Response time	ON: 4 ms, OFF: 8 ms
	Applicable voltage range	24±10% DCV
	Current value	52 mA
Air cylinder	Size	(W)10 mm×(L)24.5 mm×(H)21 mm
	Weight	15 g
	Actuation technology	Double operation type
	Applicable fluid	Air
	Withstanding pressure	1.05 MPa
	Oiling	-
	Connection caliber	M3
	Cylinder diameter	8 mm
	Piston rod diameter	3 mm
	Basic stroke	20 mm
Speed controller	Applicable fluid	Air
	Applicable tube size	φ 1.8 mm
	Applicable pressure range	0.1 ~ 0.9 MPa

Table 2.4 Specification of devices in control part

Air compressor	Power supply	Single phase 100 ACV
	Maximum applicable pressure	0.7 MPa
	Discharge air flow rate	15 L/min
	Air tank capacity	5 L
	Size	(W)350 mm×(L)310 mm×(H)290 mm
	Weight	10.3 kg
Air pump	Power supply	Single phase 100 ACV
	idling speed	1250 /min
	Motor output	90 W
	Vacuum pressure	-98.3 kPa
	Exhaust speed	90 L/min
	Size	(W)125 mm×(L)340.6 mm×(H)181 mm
	Weight	9.0 kg
Air filter	Applicable fluid	Air
	Connection caliber	Rc1/4
	Nominal filtration rating	5 μm
	Applicable pressure range	1.47 MPa
	Drain storing capacity	55 cc
	Material	Zinc die-cast
	Weight	330 g
	Drain cock	screw
Regulator	Applicable fluid	Air
	Connection caliber	Rc1/4
	Applicable pressure range	1.47 MPa
	Oiling	-
	Material	Zinc die-cast
	Weight	230 g

Table 2.5 Specification of devices in air supply part

Micro sequencer	Processing and controlling method	Stored program repeated processing method
	Input and output controlling method	Batched processing
	Program language	Relay symbol and step ladder method
	Program memory	8 k step EEPROM
	Commands	Sequencer command: 27
		Step ladder command: 2
		Application command: 89
	Processing speed	Basic command: 0.55~0.7 μs / Command
		Application command: 3.7~999 μs / Command
	Input and output	DC input: 14
		Relay input: 10
	Weight	450 g
Solenoid valve (Vacuum)	Number of positions	2 positions
	Number of ports	2, 3 ports
	Valve function	Normally closed
	Size	(W)15 mm×(L)80.7 mm×(H)24 mm
	Weight	80 g
	Applicable fluid	Air
	Actuation technology	External pilot
	Connection caliber (main)	M5×0.8
	Connection caliber (pilot)	M5×0.8
	Oiling	-
	Withstanding pressure	1.05 MPa
	Response time	ON: 15 ms, OFF: 25 ms
	Applicable voltage range	24±10% DCV
	Current value	65 mA

Table 2.6 Specification of devices in inspection part

CCD camera (Visual inspection)	Lens mount	M12×0.5
	Image-acquisition method	NTSC
	Pixel number	250,000 pixels
	Horizontal resolution	360 TV Line
	Lowest illuminance	0.1 Lux
	Angle of view	90 degrees
	Power supply	12 VDC±10% / 80 mA
	Size	(W)32 mm×(L)32 mm
	Weight	14g / 29.5 g (includes case)
	Applicable temperature	-10~50℃
CCD camera (Surrounding)	Image sensor	1/4 CCD
	Image-acquisition method	NTSC
	Pixel number	400,000 pixels
	Horizontal resolution	480 TV Line
	Lowest illuminance	0.5 Lux
	Angle of view	170 degrees
	Power supply	12 VDC±10% / 80 mA
	Size	(W)18.5 mm×(L)22 mm
	Weight	27 g
	Waterproof	IP68
Acceleration sensor (ADXL327)	Axis	3 axis
	Size	(W)4 mm×(L)4 mm×(H)1.45 mm
	Size (with circuit board)	(W)20 mm×(L)20 mm
	Power supply	1.8 ~ 3.6 VDC±10% / 350 μA
	Minimum full scale range	±2g
	Band width (X axis)	0.5 ~ 1600Hz
	Band width (Y axis)	0.5 ~ 1600Hz
	Band width (Z axis)	0.5 ~ 550Hz

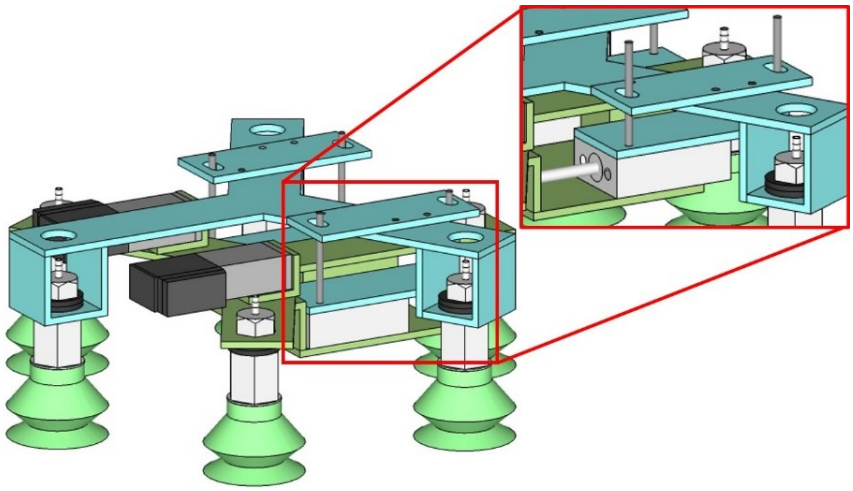

Figure 2.5 Movement part of air cylinder

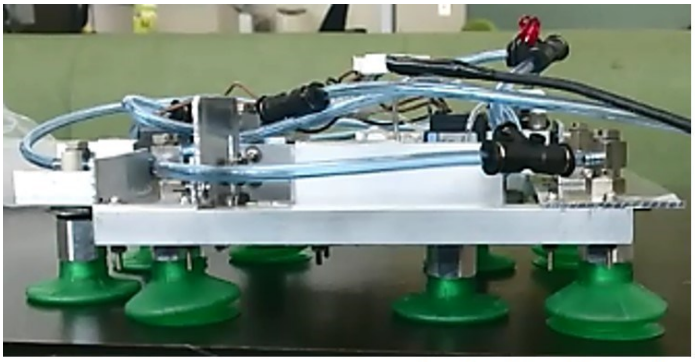

Figure 2.6 Condition of air pads when attached and not attached to surfaces

(a) (b) (c)

Figure 2.7 Electronic equipment installed on the proposed inspection robot, (a) Solenoid valve for compressive air, (b) Solenoid valve for vacuum air, (c) Air cylinder

	Step 1	Step 2	Step 3
Air pad (U)	ON	OFF	ON
Air pad (L)	ON	ON	OFF
Air cylinder (L)	OFF	ON	OFF
Air cylinder (R)	OFF	ON	OFF

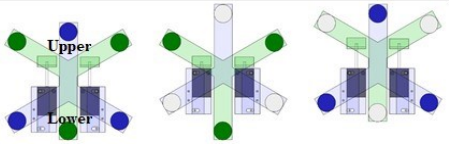

Figure 2.8 Movement system for forward motion in one cycle

	Step 1	Step 2	Step 3
Air pad (U)	ON	ON	ON
Air pad (L)	ON	OFF	OFF
Air cylinder (L)	OFF	ON	ON
Air cylinder (R)	OFF	ON	OFF

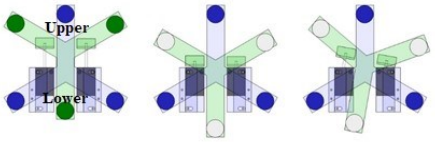

	Step 4	Step 5
Air pad (U)	OFF	ON
Air pad (L)	ON	OFF
Air cylinder (L)	OFF	ON
Air cylinder (R)	ON	ON

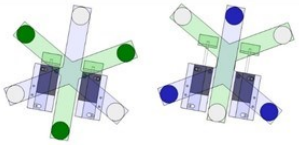

Figure 2.9 Movement system for rotation motion in one cycle

Figure 2.10 Appearance of elastodur air pads and nitrile rubber air pads

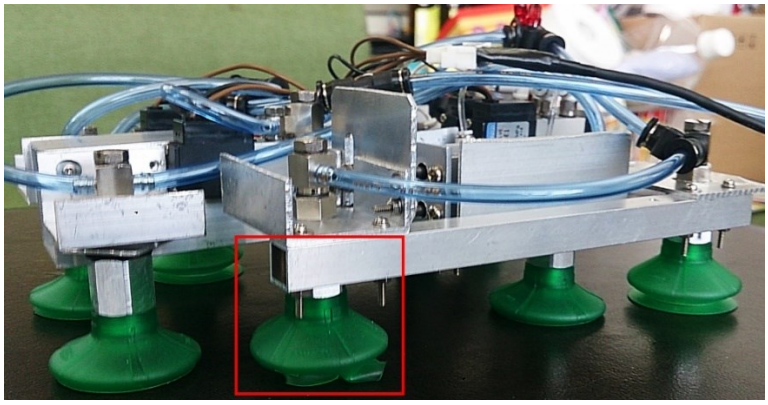

Figure 2.11 Condition of air pads while edge is rolling up by friction force

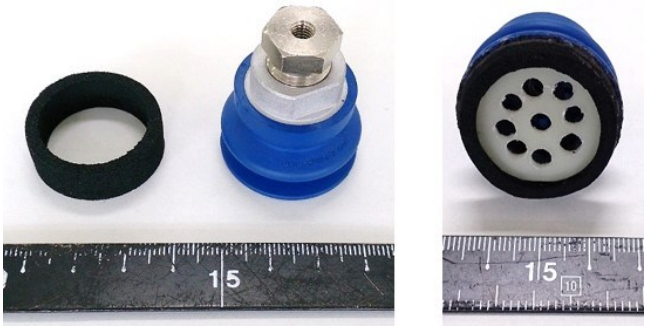

Figure 2.12 Proposed sponge bellows air pads

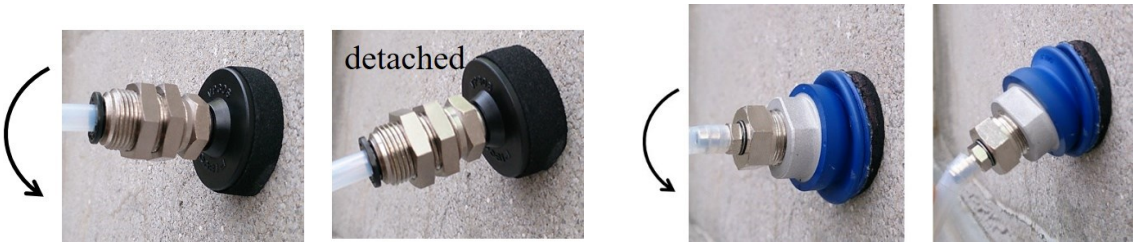

(a) (b)

Figure 2.13 Attachment condition, (a) Chloroprene sponge when a horizontal force is applied, (b) Sponge bellows air pads when a horizontal force is applied

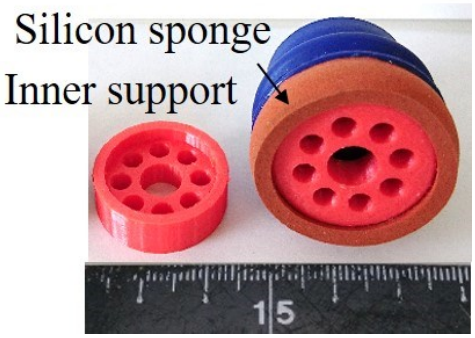

Figure 2.14 Appearance of proposed silicone bellows air pads

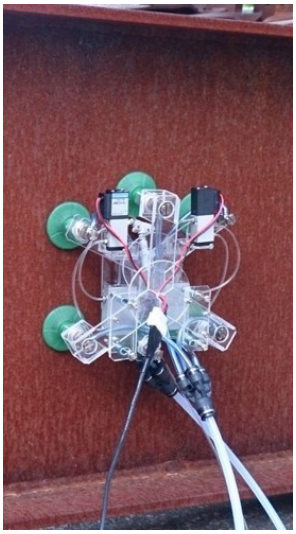

Figure 2.15 Attachment condition and robotic movement on a corroded steel surface

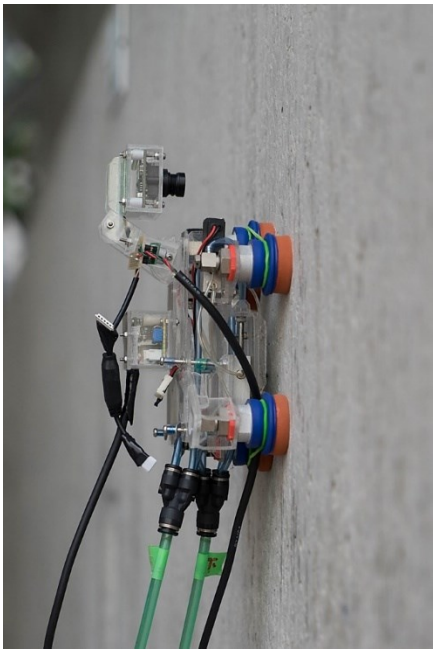

Figure 2.16 Attachment condition and robotic movement on an exterior concrete surface

Figure 2.17 Attachment condition and robotic movement with upside down condition

	 Case1		 Case2		 Case3		 Case4		 Case5	
	Steel		**Corroded steel1**		**Corroded steel2**		**Mortar**		**Mortar (crack)**	
Ra	16.1	um	34.6	um	47.1	um	15.7	um	17.3	um
Rz	139.5	um	378.1	um	381.7	um	99.4	um	154.5	um
	 Case6		 Case7		 Case8		 Case9		 Case10	
	Concete (smooth1)		**Concete (smooth2)**		**Concrete (rough1)**		**Concrete (rough2)**		**Mortar (peeling)**	
Ra	17.5	um	51.4	um	60.1	um	138.9	um	27.5	um
Rz	264.2	um	329.6	um	554.5	um	632.9	um	299.6	um
	 Case11		 Case12							
	Conctete(peeling1)		**Concrete (peeling2)**							
Ra	142	um	460.9	um						
Rz	736	um	2000.9	um						

Figure 2.18 Target surfaces on which the proposed robot is assumed to work on

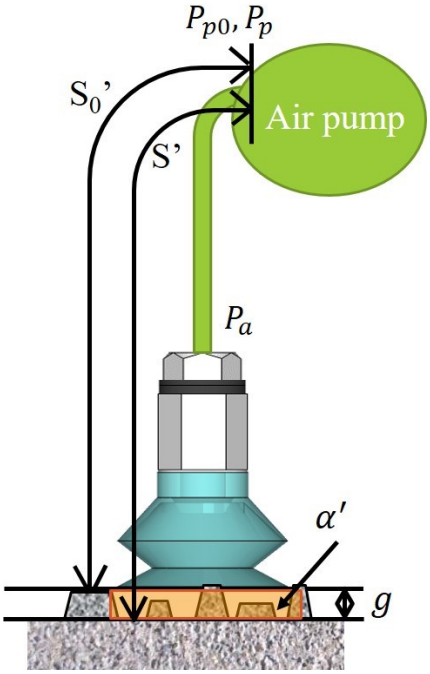

Figure 2.19 Schematic image of determining the gap coefficient

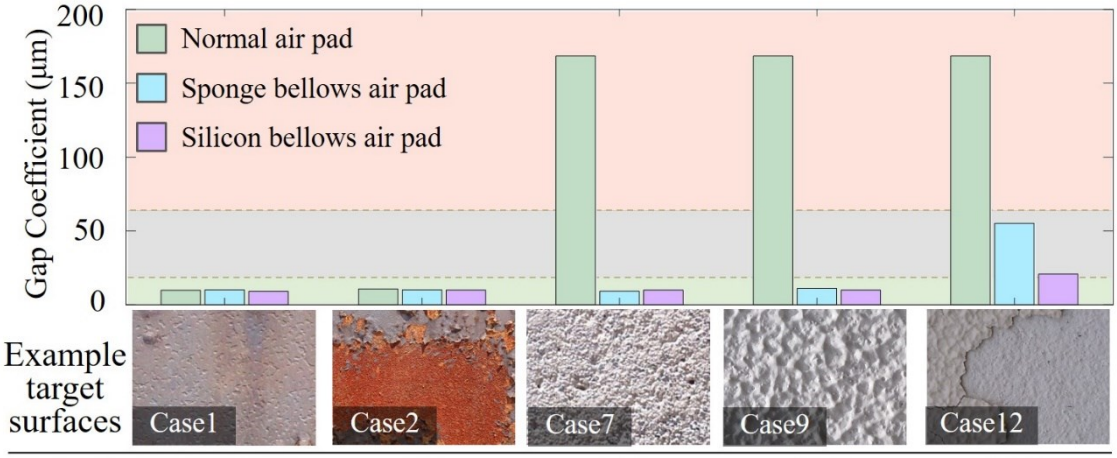

R_a [μm]	16.1	34.6	51.4	138.9	460.9
R_z [μm]	139.5	378.1	329.6	632.9	2000.9

Figure 2.20 Results of calculating gap coefficient

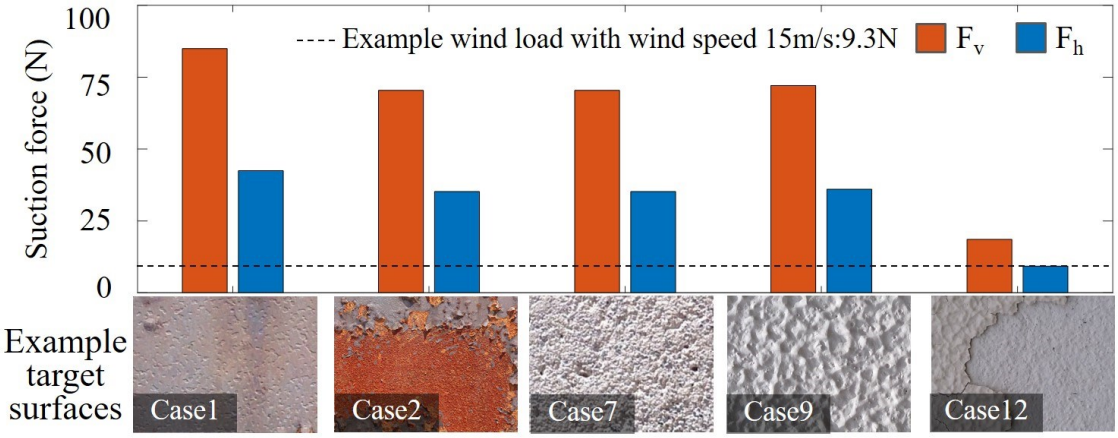

Figure 2.21 Results of calculating suction force

Figure 2.22 Inspection robot during a performance test of robotic movement on an outside concrete wall

Figure 2.23 Appearance of the target bridge

(a)

(b)

Figure 2.24 Performance test of robotic movement at the target bridge, (a) Lower chord, (b) Vertical member of the truss

Figure 2.25 Performance test of robotic movement on the trial bridge

Chapter 3

Capability of Robotic Inspection System

Abstract

For steel bridges, which consist of steel and concrete sections, it is necessary to acquire damage information such as steel corrosion or deck deterioration. In the previous chapter, a self-propelled inspection robot with the ability to move on various surfaces was developed. In this chapter, inspection functions to be installed onto this robot have been investigated, and the performance of the robotic inspection system has been verified through experiments on several types of wall surfaces and trial bridges. On the other hand, inspectors need to know the location of the inspection robot when the inspection robot is used in areas that are blind spot or at locations where corrosion or cracks exist. Thus, a function to identify the robot location using an attached camera has also been developed and implemented on the robot.

3.1. Overview

In a steel bridge inspection, it is required to acquire information such as steel corrosion, cracks of concrete decks, or changes in vibration characteristics of bridges or members, in an easy, safe and economical manner, without using scaffolding. In this research, robotic inspection has been selected to realize the inspection. Robotic inspection therefore aims to perform inspections for observation and measurement in robotic inspection concept. In the previous chapter, the inspection robot which is a self-propelled with the ability to move on various surfaces and angles was developed. Therefore, in this chapter, capability of robotic inspection system has been discussed and inspection functions which is implemented in the inspection robot has been investigated.

Proposed robotic inspection includes visual inspection to observe surface conditions, vibration measurement to obtain structural behavior and corrosion damage evaluation method to obtain corrosion information of bridges. Visual inspection is considered as part of observation. Vibration measurement of bridges using acceleration sensors is considered as a part of measurement. A corrosion damage evaluation method has also been developed for measurement yet this method will be explained in the next chapter. Furthermore, the proposed robot is expected to perform inspection at locations that are invisible or difficult to approach by inspectors. Therefore, obtaining information of the robot location is important for the robotic inspection system. In this research, the image processing applying Phase-Only Correlation method has been investigated to build a location identification method, as investigated in this chapter.

3.2. Functions for the Proposed Robotic Inspection System

The proposed robotic inspection system includes functions to observe surface conditions and measurement functions. In addition, location identification and mapping function was also investigated.

3.2.1. Visual Inspection Function

The key advantage of using the proposed visual inspection function is that it can easily inspect areas where visual inspection is normally difficult. Moreover, it can significantly reduce inspection cost and secure safety by eliminating the scaffolding or inspection passages required by inspectors. In this research, the visual inspection function focused on two points; the ability to distinguish between different colors and to check detailed surface conditions. However, the robot must remain relatively small in size to be able to inspect narrow areas. Hence, a small and light

CCD camera maintaining adequate quality to consider filming area, color identification, and image quality to perform visual inspection was selected. The proposed robot has a CCD camera for visual inspection, named hereafter visual inspection camera, in front of the robot, plus another camera, named hereafter surrounding camera to view the surrounding areas (**Figure 2.4(c)**).

Since the visual inspection camera is wide angled and the images are taken at a considerably close distance to the surface, distortion similar to a fisheye lens occurred. Although the center of the image can be taken relatively well, distortion appears towards the edge. In this research, location identification is performed by using images taken with this camera yet it was found that the accuracy of location identification became extremely poor if analysis was performed without distortion correction. In order to eliminate this distortion, camera calibration was carried out. The distortion correction was made by using values such as distortion coefficients obtained by the camera calibration process. For the camera calibration process, the distortion correction was performed applying the Zhengyou Zhang calibration method [100], and further distortion coefficient was obtained using a checkerboard. **Figure 3.1** shows an original image (left) and an image after applying distortion correction (right). The right side image in **Figure 3.1** indicates the distortion correction was successful.

The visual inspection camera is attached to the inspection robot with the height of the lens positioned 50 mm from the structural surface being viewed. In the location identification function which uses images taken by this camera, securing the filming range of images is important. This 50 mm is the minimum necessary height for securing this filming range. The visual inspection camera is 250,000 pixels, in which is far lower in resolution than commercially available digital cameras which are around 20 million pixels. However, for the visual inspection function, the filming range of images can be reduced to obtain detailed information of surface conditions. For this reason, it was considered that this CCD camera could be used as the visual inspection camera, and so the accuracy of the images obtained were then verified. Here, verification of a filming range 50 mm from the surface, distinguishing between colors using a color chart, and the image quality using a 6 mm × 6 mm grid was performed to evaluate the applicability of the visual inspection camera (**Figure 3.2**). By these images, it is possible to view a range of (W) 60 mm × (L) 45 mm using a 640×480pixel range in detail. Although the image taken by the visual inspection camera is slightly blue and the filming range is small, it is still able to take images which do not greatly differ in color recognition and image quality to the digital camera images, so long as a 640×480pixel resolution is used.

Figure 3.3 shows an image taken by the visual inspection camera in the performance test of visual inspection at the existing bridge referred to in the previous chapter. The right side of the figure shows the image attached with the actual scale adjusted to the image from the relationship between the pixel value and the actual size. The image was taken when performing inspection of

a vertical member of the truss. From **Figure 3.3**, it is possible to see the corrosion condition of the steel surface, the uneven surface condition, and furthermore, the color difference using the visual inspection camera. Based on the results of basic performance tests and the images taken of the target surfaces, it has been clarified that the visual camera can take high quality images to perform effective visual inspection. Moreover, **Figure 3.4** presents two images taken of a lower chord, one by the visual inspection camera, and one by a forward facing surrounding camera. The left-hand image was taken by the visual inspection camera, and the right hand image was taken by the forward facing surround camera. As shown, the visual inspection camera can take detailed images of surface conditions such as peeling, cracks, color and roughness of the corrosion surface. Furthermore, by using the surrounding cameras, the inspector can check the surface conditions of not only close surfaces, but also the surface condition one step ahead of the robot. Therefore, the inspectors are able to estimate the sections which need to be inspected in real time, by assessing the condition of the surfaces ahead of the robot.

3.2.2. Location Identification Function to Determine the Inspection Location

The inspection robot is required to work in areas visually unclear for inspectors, as the target areas considered are either narrow to perform visual inspection, difficult to access or are invisible. For this reason, it is important to identify the location of the robot.

There are some methods to identify the location of the robot using GPS, ultrasonic waves or lasers [101,102]. However, these methods have some difficulties to apply to location identification function for the robotic inspection. The possibility that a GPS may not work properly in the target parts of this robot due to closed areas is considered. Moreover, it is considered preferable to avoid installing new equipment since the inspection robot is made relatively small. Hence, location identification method using pictures taken by the visual inspection camera was built and installed as one of the inspection function. The Phase-Only Correlation method (POC Method) that uses an image matching process such as fingerprint authentication program, has been applied to make a function program [103-105]. Location identification method is carried out using numerical calculation software MATLAB.

3.2.2.1. Phase-Only Correlation Method

The flow of the POC method is shown in **Figure 3.5**. Firstly, Fourier transformation is performed for two different images, to obtain amplitude and phase. In this method, analysis is performed using only phase information to place emphasis on the edges of images and omit information regarding brightness. Two phase images are then combined to obtain the peak value of the POC function. This peak value demonstrates how much the position between two images are changed. Considering two $N_1 \times N_2$ pixel images, $f(n_1, n_2)$ and $g(n_1, n_2)$, where the index ranges are

assumed as $n_1 = -M_1, \dots, M_1$ and $n_2 = -M_2, \dots, M_2$ for mathematical simplicity, $N_1 = -2M_1 + 1$ and $N_2 = -2M_2 + 1$. Letting $F(k_1, k_2)$ and $G(k_1, k_2)$ denote the 2D DFTs of the images, the cross-phase spectrum $R_{FG}(k_1, k_2)$ can then be defined as:

$$R_{FG}(k_1, k_2) = \frac{F(k_1, k_2)\overline{G(k_1, k_2)}}{\left|F(k_1, k_2)\overline{G(k_1, k_2)}\right|} \tag{3.7}$$

where $k_1 = -M_1, \dots, M_1$, $k_2 = -M_2, \dots, M_2$ and $\overline{G(k_1, k_2)}$ denotes the complex conjugate of $G(k_1, k_2)$.

The POC function $r_{fg}(k_1, k_2)$ is the 2D IDFT of $R_{FG}(k_1, k_2)$ and is given by:

$$r_{fg}(k_1, k_2) = \frac{1}{N_1 N_2} \sum_{k_1 k_2} R_{FG}(k_1, k_2) W_{N_1}^{-k_1 n_1} W_{N_2}^{-k_2 n_2} \tag{3.8}$$

where $W_{N_1} = e^{-j*2\pi/N_1}$ and $W_{N_2} = e^{-j*2\pi/N_2}$. When two images are similar, their POC function $r_{fg}(k_1, k_2)$ gives one distinct sharp peak. On the other hand, the peak significantly drops, when two images are not similar to each other. Moreover, when the two images are shifted, the position of the peak shifts from the center. The shifted value from the central point shows how much two images change in position. However, what is obtained here is a pixel value, which needs to be collected to the actual length.

3.2.2.2. Location Identification Method and Mapping Function

A detailed outline of the location identification function is as follows. One picture is taken by the attached camera for each cycle of robotic movement, and then using consecutive two images, the values of parallel translations in both horizontal and vertical directions (hereafter named, x and y direction) and a rotation angle can be obtained. The proposed robot can rotate approximately 10 ° in one rotation cycle. Therefore, to determine the rotation angle, the image after rotation is rotated between −15 ° to +15 ° with 0.1 ° pitch. The rotation angle and the values of x and y are obtained using the POC method at same time. By summating all obtained values, the total parallel translation and rotation angle from the beginning to the end of the robot movement can be calculated.

In the location identification function, the location of the robot could be determined numerically. However, when the robot is working at sections that are out of visible sight, it is difficult to identify the real location of the robot from the obtained values. Therefore, another CCD camera, surrounding camera, has been attached to look 170° in front as well as a mapping function of the motion track of the inspection robot to help inspectors determine the location of

the robot visually. It is expected to be an inspection database to record inspection results and recognize progressing of corrosion or cracks comparing previous inspection maps. An example of applying location identification and mapping function is presented in **Figure 3.6**. **Figure 3.6(a)** shows the obtained images from the inspection robot at the beginning point and after one movement. The precise method of this function is the implementation of a 1010 × 1010 pixel basemap and the images taken by visual inspection camera continuously. First, one image is taken at the starting position of the robot, and this is attached to the center of the basemap (**Figure 3.6(b)**). Second, using the obtained values from the location identification function after the robot moves (**Figure 3.6(c)**), the new image is attached to the aforementioned image. This cycle is repeated and so that all images can be attached in order (**Figure 3.6(d)**). Finally, the entire map is completed by combining all the basemaps. Moreover, by implementing a shutter to the camera of this program, it is possible to retake images when the obtained result is completely different due to shadow issues. **Figure 3.7** shows a schematic image of the location identification function using the inspection robot. In this function keeping intersection part as shown in **Figure 3.7** is important. Therefore, lens height was decided as 50 mm from surfaces. During or after inspection, using mapping results, the inspectors can detect cracks or corrosions and their size. Method to detect them is so far using the images or movies from camera however another method which performing analysis using wavelet transformation to detect cracks automatically in images will be investigated in following subsection.

3.2.2.3. Accuracy Improvement Process of Location Identification Function and Performance Test at Concrete Wall

The following test was performed on a concrete with good surface conditions which is case 7 in target surfaces. The initial position and end position of the robot can be seen in **Figure 3.8**. The movement was three forward motions, two clockwise rotations, and then seven motions forward, hence the total movement was 61 mm in the x direction, 165 mm in the y direction, with a rotation angle of 19 °. The result of analysis, in the x direction is 54.45 and, 149.76 mm in the y direction with a rotation angle of 18 °. The relative error was approximately 10 % which is considered high. The allowable error of this function was considered around 5 %. The location identification function is summing the all obtained values and so relative error may increase. However, when the robot moved only forward, the error was significantly smaller.

To decrease the relative errors, make the calculation pitch of rotation angle smaller (0.01 °), remove the distortion parts, insert deblurring step, put scaling factor and use the average of peak values of POC function if the difference between the peak and other peaks is less than 0.001. After applying distortion correction, there are still some parts distorted thus remove the edge. Although the value is depending on the images, the area of 90 % to 95 % from the center has used for

calculation. When the results show obvious error, most cause is picture blur or shadow. Therefore, deblurring step which uses for camera shake correction was applied. The height of the visual inspection camera is not always same due to attachment condition of the inspection robot. When the height of camera changes, the scale of the obtained images also changes. Therefore, to correct this scaling, similar method to calculating rotation motion was applied. The scaling factor is 0.9 to 1.1 with 0.01 pitch.

The results of this test after modification are shown in **Table 3.1**. As shown, the total movement was 63.9 mm in the x direction and, 164.5 mm in the y direction, with a rotation angle of 20.5 °. The maximum relative error becomes half of the previous method and it was considered appropriate and so, it has been confirmed that the location identification function performs well when used on real structures. The mapping result, a map of the robot tracks, is shown in **Figure 3.9**. It is able to confirm that the modified analysis is tracking robot's movement better, hence demonstrate that the mapping function can track the movement of the robot effectively. It has thus been confirmed that the location identification function has the capacity to work in real inspection sites.

However, this performance test is very short movement. Therefore, to confirm if the accuracy of this function increases due to movement distance, another performance test at concrete wall similar condition to previous test was carried out. The initial position and end position of the robot are shown in **Figure 3.10**. In this test, the movement was thirty-two times forward motions, five clockwise rotations, and then twelve times forward, hence the total movement was around 223 mm in the x direction, 670 mm in the y direction, with a rotation angle of 46 °. The result of analysis, in the x direction is 215.23mm and, 643.80 mm in the y direction with a rotation angle of 44.08. **Figure 3.11** shows the mapping result using obtained values. The maximum relative error is 4.2 % in rotation thus the error became slightly increase. However, in **Figure 3.11**, there is not big gap in the connection part of each images so that it needs to consider the way to obtain more accurate values to change pixel to millimeters. It can also be able to consider the body of the robot is twisting due to attachment conditions even the rotation angles of images in analyzing are correct. Currently, the relative error is evaluated as a percentage, however this means that as the movement distance increases, the error tolerance range is expanded. For this reason, the allowable error has been limited to being within a 150 mm diameter area. This range has been determined by taking into consideration the size of the inspection robot, which currently has a cable length of 10 m, and using this as a reference. Since the error did not increase in proportion to the distance moved during experiment, the location identification function of the robot can be considered to possess sufficient precision. Especially if the inspection range is small, accuracy becomes higher. These errors are considered to be permissible values yet some improvement methods can be thought.

3.2.3. Crack Detection Function for Concrete Component in Steel Bridges

In the previous subsection, it was shown that the image obtained by the visual inspection camera was able to observe the surface condition in detail, and the condition of damages such as cracks and peelings due to corrosion could be confirmed. Moreover, with the mapping function in location identification, it is possible to record the inspection track as a map by connecting the captured image according to the movement of the robot. In addition to these functions, a crack detection function was attempted to implement to the robotic inspection function in this subsection. Since the range of the image of the visual inspection camera is narrow and can be seen detailed surface conditions, it is possible for the inspector to visually judge from the image. For this reason, this function is supposed to be an optional function aimed at leaving it as an inspection record. The actual scale is known by the location identification function therefore, it can be considered that it is possible to judge the degree of danger using the crack scale which is for measuring the crack width used for crack inspection of concrete.

For the crack detection, a method applying Gabor wavelet function [106,107] was investigated. First, edge emphasis of obtained images is performed (**Figure 3.12(a)**). Next, Gabor wavelet transformation is applied to the images (**Figure 3.12(b)**). Then, cracks are judged using threshold (**Figure 3.12(c)**). Finally, noise is eliminated by crack shape and length (**Figure 3.12(d)**). In this method, not only cracks but also other things such as hole, dirt, shadow or spot mark can be detected if it is over 0.2 mm, it is therefore, necessary to consider a method to separate them from cracks. It is considered that the holes or spot marks can be distinguished by shape such as similar to circle or too short. Therefore, such holds can be eliminated by crack shape and length. Since only cracks of over 0.2 mm are assumed to be a target in this study, evaluation standard is using pixel area (2 pixels × 2 pixels: 0.19 mm × 0.17 mm) corresponding to 0.2 mm instead of each pixel. From **Figure 3.12 (d)**, which is the result obtained by the above method, it was confirmed that the part which is not a crack disappeared, only the crack part remained. The visual inspection camera can obtain images with detailed surfaces conditions therefore, this crack detection function can be used as optional function to emphasis cracks or record conditions. Gabor wavelet transformation can be represented as follows;

$$\Psi_{\theta k}(n_{10}, n_{20}) = \frac{1}{\alpha^k} \iint_{-\infty}^{\infty} f(n_1, n_2) \psi_g \left(\frac{n_1 - n_{10}}{\alpha^k}, \frac{n_2 - n_{20}}{\alpha^k} \right) dn_1 dn_2 \qquad (3.9)$$

Where, (n_{10}, n_{20}) is focused point of wavelet transformation, $\Psi_{\theta k}(n_{10}, n_{20})$ is wavelet coefficient of Gabor wavelet, ψ_g is Gabor function and α^k is scaling factor of wavelet transformation.

3.2.4. Vibration Measurement Function

Not only the visual inspection camera but an acceleration sensor is attached to the robot to recognize structural behavior as detailed inspection. For example, it is able to obtain performance level of bridges using acceleration [108]. A natural frequency of healthy bridge shows high and damaged bridge shows low natural frequency. Therefore, measuring bridge vibration periodically, the possibility of evaluating if the bridge got some damage in the middle of inspection interval can be considered. Measuring bridge behavior by acceleration sensor is normally performed using several acceleration sensors yet using the inspection robot, it can measure acceleration while moving. Therefore, it is conceived that it becomes possible to obtain bridge behavior without disposing of a plurality of acceleration sensors.

In this subsection, to realize aforementioned measurement, focusing on getting response spectrum, dominant frequency, vibration characteristics by obtaining acceleration data of structures and analyzing the data. Advantage of using inspection robot for determining structural behavior is that it is difficult to replace the acceleration sensor on real structures however using this robot, it becomes easy to move and replace its position. Furthermore, it is also possible to check the surface condition by attaching a camera, while the inspection robot is moving. Thus, it is easy to measure the acceleration if the inspector judges it necessary. This inspection robot is designed for estimating the sections that are needed to inspect before the accelerometer has been disposed in real case scenarios.

3.2.4.1. Investigation of Vibration Characteristics of Proposed Robot

The proposed inspection robot was confirmed to have enough suction force to attach several types of surfaces, however considering to install acceleration sensor, robot vibration may be influenced to obtaining bridge vibration. It is considered that air pads have the possibility to affect robot vibration due to nonlinearity of rubber behavior. Therefore, it is important to confirm the influence of air pads to obtained vibration by the inspection robot. A laboratory experiment using vibration generator was performed to evaluate suction condition and vibration characteristics of the inspection robot. In particular, data from an acceleration sensor attached to the inspection robot, named hereafter robot acceleration sensor, and direct attached acceleration sensor are compared to confirm if the robot fixed to the surface enough to obtain bridge vibration. **Figure 3.13** shows sensor arrangements. A base plate was attached to the vibration generator and its natural frequency was calculated 250Hz by eigenvalue analysis in FEM. Shell model was used for the analysis. Both acceleration sensors are same as indicated in **Table 2.6**.

In this test, the robot was attached on a base plate next to the direct attached acceleration sensor (**Figure 3.13**) to know the vibration characteristics of air pads. Five waves which are triangle wave of 1~5 Hz in 1Hz pitch were used. **Figure 3.14(a)** shows one of the input wave

which is triangle wave with 2 Hz. **Figure 3.14(b)** shows obtained acceleration data from both robot acceleration sensor and direct attached acceleration sensor. A red line indicates acceleration data from robot acceleration and a blue line indicates direct attached acceleration sensor. It was confirmed that although the position and the amplitude of the peak coincided with both acceleration sensors, the amplitude of the robot acceleration sensor increased with the vibration after the peak. This phenomenon is considered to be the influence of the vibration characteristics of the air pad. **Figure 3.14(c)** shows Acceleration Fourier Spectrum obtained by each acceleration data. The colors of the lines are same as obtained acceleration data. The figure indicates that both lines fit well, especially this graph shows the important frequency band in bridge structures. Here, to evaluate vibration characteristics of the inspection robot, a gain, a phase lag and a coherence were used. Calculation method of a gain, a phase lag and a coherence are shown as follows.

When $u(t)$ represents an input signal and $v(t)$ represents an output signal, a function indicating the relationship between them is generally called a transfer function. In this case, the differences in the amplitudes of the two waves and the deviations using transfer function which is between both acceleration data of the robot acceleration sensor and the direct attached acceleration sensor, are investigated. Here, focusing on a gain, a phase lag, and a coherence to investigate the relationship between two waves. In general, the transfer function is expressed by the following equation.

$$\begin{gathered} U(s)G(s) = V(s) \\ s = \sigma + j\omega \end{gathered} \tag{3.10}$$

Where, $U(s)$ and $V(s)$ are Laplace transforms of input and output signals, respectively, and $G(s)$ is a transfer function. The expression of Laplace transform is represented by complex regions. However, in the case where the expression is limited to the frequency domain without considering the transient phenomenon, simplification of the equation of $\sigma = 0$, $s = j\omega$ can be possible. Note that j is conventionally used in imaginary units in control engineering. Therefore, the transfer function $G(j\omega)$ is expressed by the following equation.

$$G(j\omega) = \frac{V(j\omega)}{U(j\omega)} \tag{3.11}$$

A gain indicates the absolute value of the transfer function logarithmically and is expressed by the following equation. The unit is decibel [dB]. The meaning that if it is 0 at a certain frequency, the amplitude of the output signal is equal to the input signal.

$$Gain\ [dB] = 20 \cdot \log_{10}|G(j\omega)| \tag{3.12}$$

A phase lag is a phase angle of the transfer function, which means the phase shift of the output signal with respect to the input signal in a certain frequency component and is expressed by the following equation. In this research unit is indicated in degrees.

$$Phase\ Lag = \angle G(j\omega) \tag{3.13}$$

A coherence represents the strength of the correlation between the input signal and the output signal and is used as an index for measuring the reliability level of the transfer function. The coherence is calculated as follows using the power spectrum W_{uu}, W_{vv} and the cross spectrum $W_{uv}$of the input signal u and the output signal v.

$$\gamma^2 = \frac{|W_{uv}|^2}{W_{uu} \cdot W_{vv}} \quad (0 < \gamma^2 < 1) \tag{3.14}$$

The gain, the phase lag, and the coherence obtained using the acceleration data, obtained by the direct attached acceleration sensor, as an input signal and the acceleration data, obtained by the robot acceleration sensor, as an output signal are shown in **Figure 3.15**. From all graphs in **Figure 3.15**, it can be considered that disturbance of waveform at 50 Hz has been affected by power supply noise. Moreover, natural frequency of base plate was calculated 250 Hz. Therefore, the natural frequency of air pad can be considered 140 Hz. An amplitude of robot acceleration is bigger and phase lag occurs over 140 Hz, it was confirmed through the gain and phase lag graphs. Finally, from coherence graph, the influence of robot was smaller and shaper than other signals such as noise of power supply. Therefore, it can be considered the influence of robot can be distinguished from other signals. It was confirmed all cases indicate similar results. Moreover, in all experimental cases, the influence of the air pad was not confirmed at frequency under 50 Hz. Therefore, it can be possible to acquire the vibration characteristics of bridges when measuring the acceleration of bridges using the inspection robot.

3.2.4.2. Performance Test of the Vibration Measurement Function

In this test, the robot was also attached next to an acceleration sensor that was attached directly to the bottom flange of the existing bridge, as shown in **Figure 3.16**. The left-hand picture shows the acceleration sensor attached directly to the bridge, and right-hand picture displays the setting position of the inspection robot. Measurements were carried out for 5 minutes, with a sampling

frequency of 1000 Hz. **Figure 3.17(a)** shows the acceleration Fourier spectrum of both acceleration sensors. The blue line shows the acceleration sensor that was attached directly to the bridge, and green line shows the data obtained by robot acceleration sensor. Moreover, the magnified region shown in the lower side of **Figure 3.17(b)** highlights the important frequency bands, excluding low frequency and high frequency from bridge vibration. As shown in the previous subsection, the influence of robot vibration by the air pad was not confirmed, and it was confirmed that the natural frequency of the bridge can be obtained by the acceleration sensor installed on the inspection robot.

3.2.5. Hammering Test for Concrete Components in Steel Bridges

According to road administrators, if the inspection robot can perform hammering test in the regular inspection process, the inspection robot can reduce burden of inspectors. Moreover, it was confirmed in the previous investigation, the inspection robot is able to attach surfaces tightly and vibration of robot itself can be distinguished from other signals. However, there is currently no hammer installed on the inspection robot hence, hammering test was simulated manually and vibration and sound generated by inspector's hammer blow were obtained. Then a method to obtain information regarding vibration or sound change, has been investigated for future use.

Concretely, the hammering test was conducted manually, and test whether the sensors installed to the inspection robot can acquire the presence or absence of the internal defect in concrete parts of steel bridges, was conducted. In addition to the acceleration sensor, a small microphone was installed to the inspection robot for this test, and the sound data was also analyzed. This function is also as an optional function, therefore, an investigation was conducted based on experiments that have been conducted. The hammering test was conducted with the trial bridge mentioned in Chapter 2. On the trial bridge, there is a wall that made a deliberate defect inside the concrete made for hammering test exercises, and then experiments were conducted there. A specification of the microphone is shown in **Table 3.2**.

For this experiment, the inspection robot was attached close to the hitting points during hammering tests. The experiments that measuring vibration and sound with the acceleration sensor and the microphone were conducted (**Figure 3.18**). In this test, wall surface for hammering test on an inside of an abutment was used, and measurements were made at places where the presence or absence of internal defects was known. The results of the vibration data obtained by the acceleration sensor with respect to the internal defect surface and the healthy surface are shown in **Figure 3.19(a)** and **Figure 3.19(b)**, respectively. The acceleration sensor installed to this inspection robot is a MEMS type sensor, and data up to 1500 Hz can be acquired. From **Figure 3.19(a)** and **Figure 3.19(b)**, it can be confirmed that the surface with internal defects has peaks with many frequency components. Moreover, it can also be confirmed that the frequency

range showing the peak is low on the surface having the internal defect. It was also confirmed the sound with the internal defect was lower than without defects at the time of hammering test, however, the sound was assumed to indicate a peak in a higher frequency range compared to the results of acceleration sensor. For this reason, it is expected that there is another frequency range shows sharp peak which cannot be acquired by this acceleration sensor yet, it can be considered the differences in applicable frequency range are able to acquire by the acceleration sensor.

On the other hand, as a results of hammering test using the microphone are shown in **Figure 3.20**. It was confirmed the sound at the surface with the internal defect mixed with more sound component than the sound at the surface without internal defect similar to the result of the acceleration sensor as shown in **Figure 3.19**. Furthermore, it was indicated that the sound of the defect part is low as well as confirmed by the acceleration sensor. The peak shows around 2000 Hz and the relationship between the real pitch and the frequency is also in good agreement.

Finally, the results indicate that it is possible to detect internal defects by both acceleration sensor and microphone. An advantage of using vibration data instead of sound data for hammering inspection, since the path through which vibration propagates is not an air but an individual, attenuation is smaller than that of sound recording and data analysis of three axes is possible. If data analysis method of hammering test using acceleration is established, more detailed analysis may be possible by using data of three axes. In addition, if the acceleration sensor is used for hammering test, the inspection robot can install other inspection devices to the space of the microphone. Moreover, results indicate the possibility of acquiring structural behavior changes by deterioration of decks using obtained acceleration data.

3.2.6. Inspection Simulation based on the Currently Proposed Robot

In this section, the robotic inspection functions which the proposed inspection robot can perform have been further discussed. The capacity of the proposed inspection robot, such as movement speed, that was determined in Chapter 2 has been used as reference. In this subsection, the inspection time has been calculated assuming that an inspection is performed within a range of (W) 240 mm × (L) 200 mm after the proposed inspection robot has moved five meters above a set position. **Table 3.3** shows information regarding to the movement and inspection duration of the proposed inspection robot during the simulated inspection. **Table 3.4** shows the calculation results. Case 1 assumes that location identification is performed during each movement. On the other hand, since the movement distance of forward movement can be calculated by the number of movements (one forward movement is equal to 20 mm), Case 2 assumes that location identification is not performed during the movement up to five meters above the initial set position. Moreover, in Case 2, although pictures of the surface are taken after each movement, location identification is only performed after the inspection is completed. During the simulated inspection,

the time to take pictures is included in the measurement time of 2.5 seconds, as well as the movement time for both Case 1 and Case 2. Currently, movement takes up most of the total operation time for inspection.

However, the speed of the proposed inspection robot and the distance it can move in one movement can still be improved, and this would significantly reduce the total operation time. The main advantage of the proposed inspection robot is that it can collect information for each measurement point, however many there are. It is considered that the data from this simulated inspection can be used to optimize maintenance planning.

3.3. Summary

In this chapter, functions of the robotic inspection system implemented on the inspection robot developed in Chapter 2 was examined. Small inspection equipment applicable to the proposed inspection function was implemented and its performance was also verified. Summaries of each inspection function is shown as follows.

- Visual inspection function
  Visual inspection was carried out using images taken by the small CCD camera installed on the front of the inspection robot. From the results of performance tests of visual inspection, it was confirmed that obtained images from the extremely short distance have adequate quality for visual inspection. By this visual inspection function, it became possible to observe detailed surface conditions such as corrosion of steel members and cracks of concrete decks.
- Location identification and mapping function
  When the inspection robot is used at areas that are invisible or the location of existing corrosion or cracks, inspectors need to know the location of the robot. In consideration of the size of the robot and the situation of inspection sites, in this research, a location identification function using obtained images by visual inspection camera was implemented to the inspection robot. This function traces the movement trajectory of the inspection robot by calculating the movement of the image before and after the robot movement. Furthermore, using values obtained by the location identification function, a mapping function that connects the obtained images as a map was also implemented. The image obtained by the mapping function is preserved as an inspection record. Thus, it is a function assumed to use for judging the progress situation of corrosion and cracks.
- Crack detection function
  A function to detect cracks using Gabor wavelet transformation applying to the image obtained

by the visual inspection camera as an optional function was implemented. The visual inspection camera has a narrow filming range, therefore, it is possible to check cracks of over 0.2 mm visually. As an advantage, this function visually emphasizes the crack part and the crack width and length can be determined from the image.

- Vibration measurement function

  This is a function to obtain bridge vibrations using the acceleration sensor installed to the inspection robot. Laboratory experiments were conducted to investigate whether the vibration of the robot itself affects the acquisition of natural frequency of bridges. As a result, the influences of obtaining bridge vibrations due to the inspection robot, mainly the air pad was not confirmed. It is because natural frequency of the robot is around 150Hz and it is higher than natural frequency of bridges. Moreover, the possibility of acquiring bridge vibration was confirmed by performance test at existing bridge.

- Hammering test function (optional function)

  Currently, the inspection robot has no hammer for hammering test. However, for the future use, the method to detect the internal defects of concrete components of steel bridges using the vibration and the sound, which becomes the basis after introducing the hammering system in the future, was verified.

Performance and applicability of all functions were confirmed by experiments at the target surfaces, the existing bridge or the trial bridge mentioned in Chapter 2. In the next chapter, a corrosion damage evaluation method will be investigated. It is assumed that the method will be used as an independent inspection method and also as a detailed inspection function of the inspection robot.

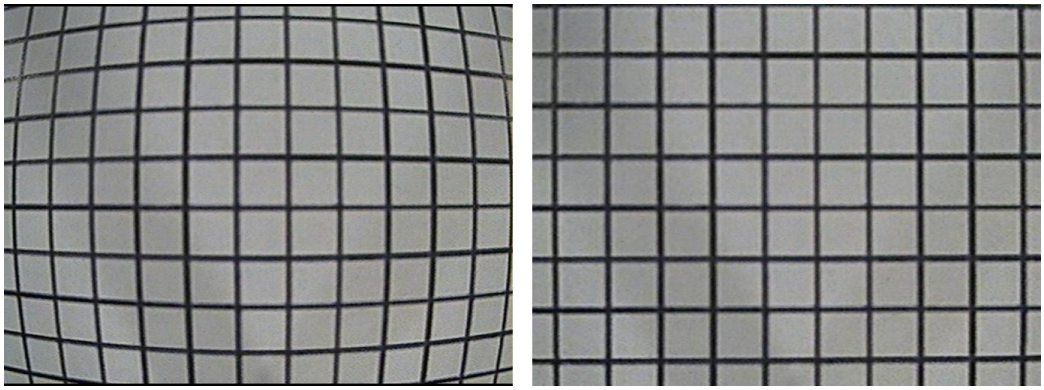

Figure 3.1 Original image taken by the visual inspection camera and image after applying distortion correction

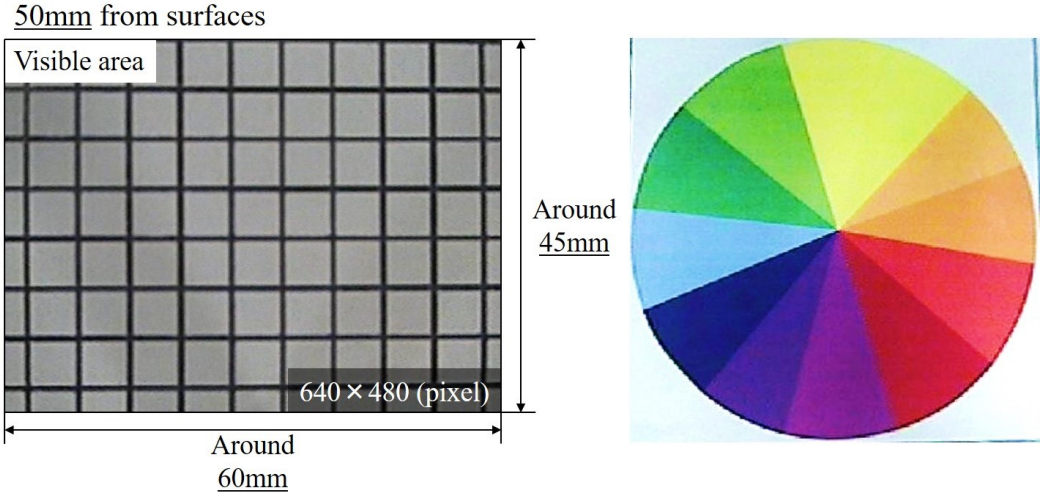

Figure 3.2 Filming range and color discrimination of the visual inspection camera

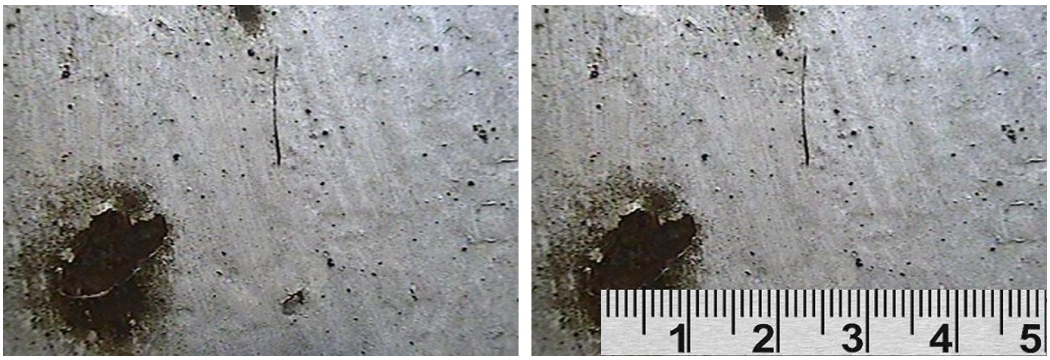

Figure 3.3 Image taken by the visual inspection camera at vertical member of truss in existing bridge

Figure 3.4 Images from both the visual inspection camera and surrounding camera

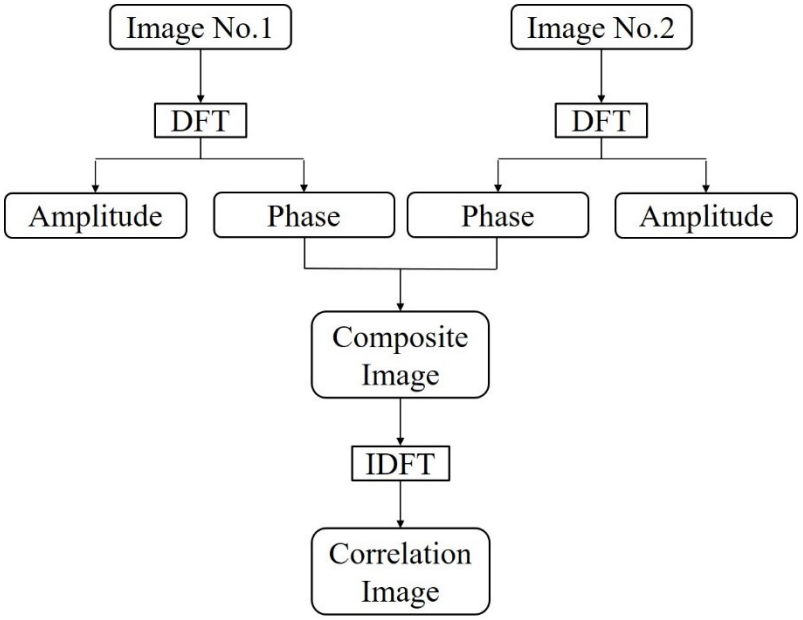

Figure 3.5 Flow of the POC method

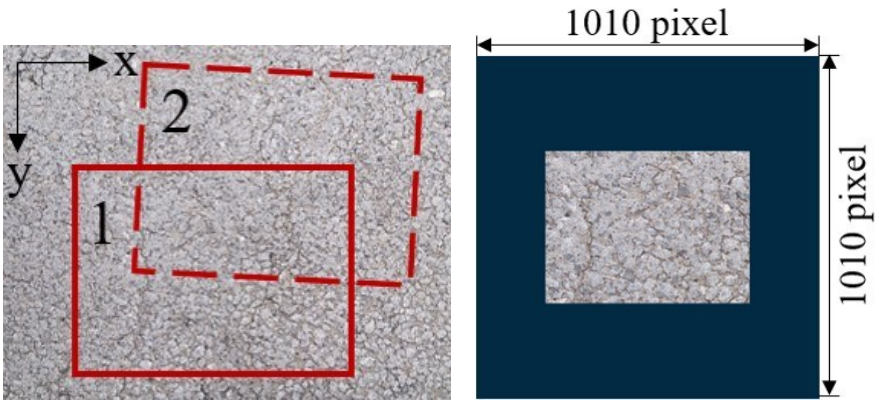

(a) (b)

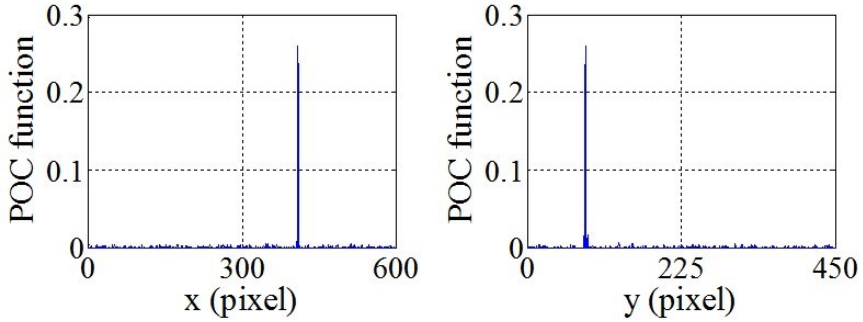

(c)

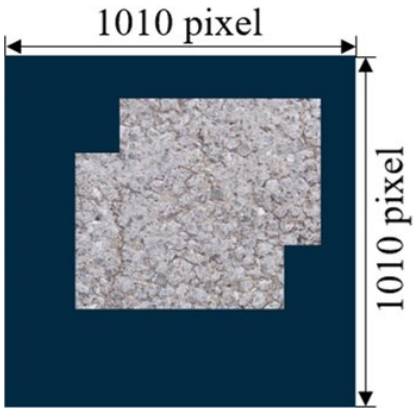

(d)

Figure 3.6 Example of applying the location identification and mapping function, (a) Images taken at the initial and after one movement of the inspection robot, (b) Initial image attached on the base map, (c) Result from applying the location identification function, (d) Image from applying the mapping function

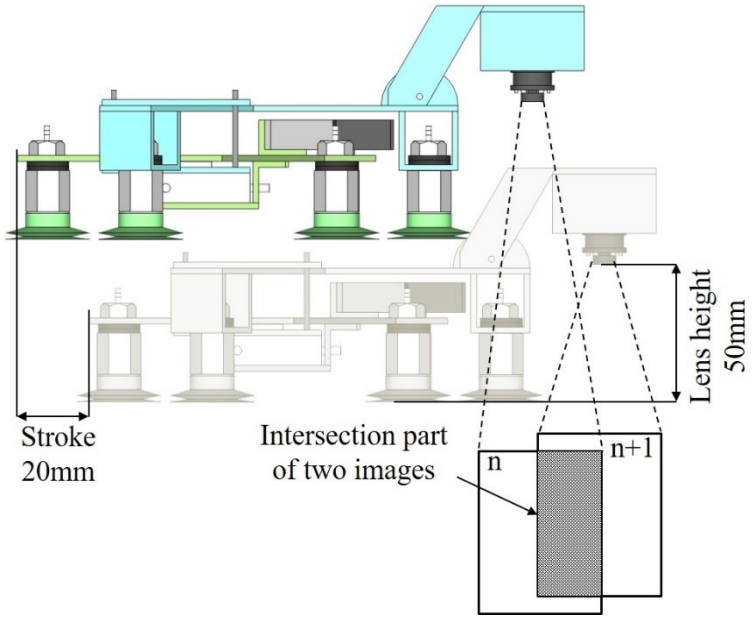

Figure 3.7 Schematic image of the location identification method using the inspection robot

Figure 3.8 Initial and end position of the robot in the performance test

Table 3.1 Result of location identification after modification

No.	x (pixel)	y (pixel)	x (mm)	x (mm)	θ (degree)
1	0	0	0	0	0
2	35	198	1.8	19.8	0.9
3	-44	202	-2.3	20.2	-0.5
4	-26	181	-1.3	18.1	-1
5	250	20	12.9	2	9.1
6	280	-29	14.5	-2.9	18.6
7	97	157	5.0	15.7	19.1
8	96	156	5.0	15.6	18.8
9	104	155	5.4	15.5	18.2
10	100	159	5.2	15.9	18.7
11	110	152	5.7	15.2	19.3
12	120	148	6.2	14.8	19.7
13	115	150	5.9	15	20.5
		Total	63.9	164.9	20.5
		Real	61	165	19
		Error	-2.9	0.1	1.5

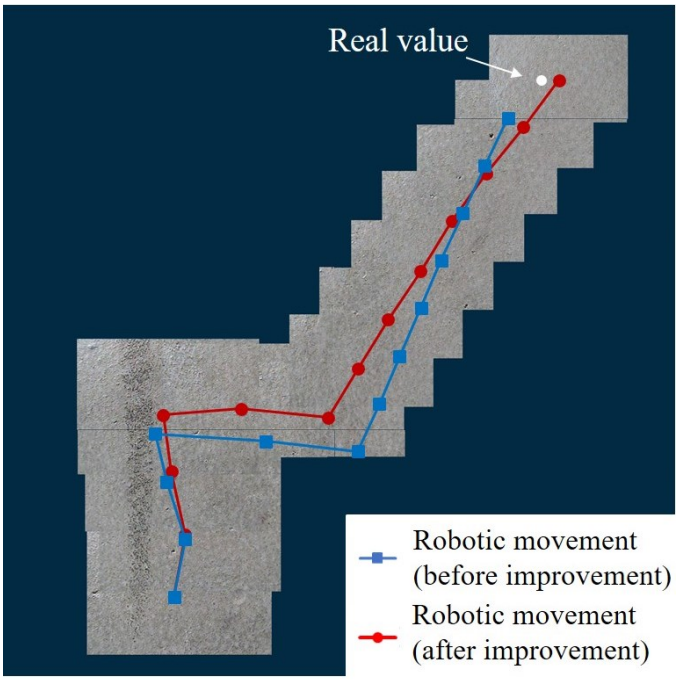

Figure 3.9 Image from applying the mapping function

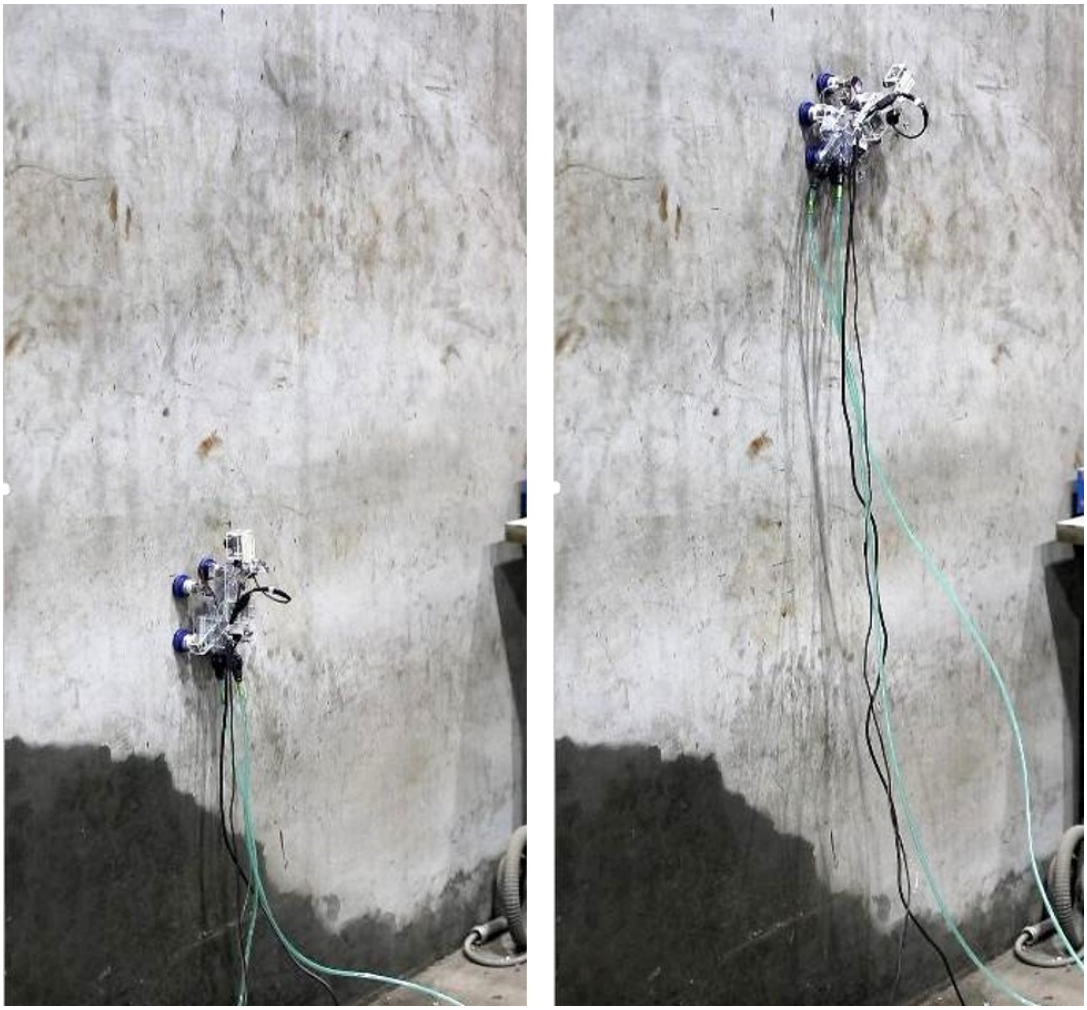

Figure 3.10 Initial and end position of the robot in the second performance test

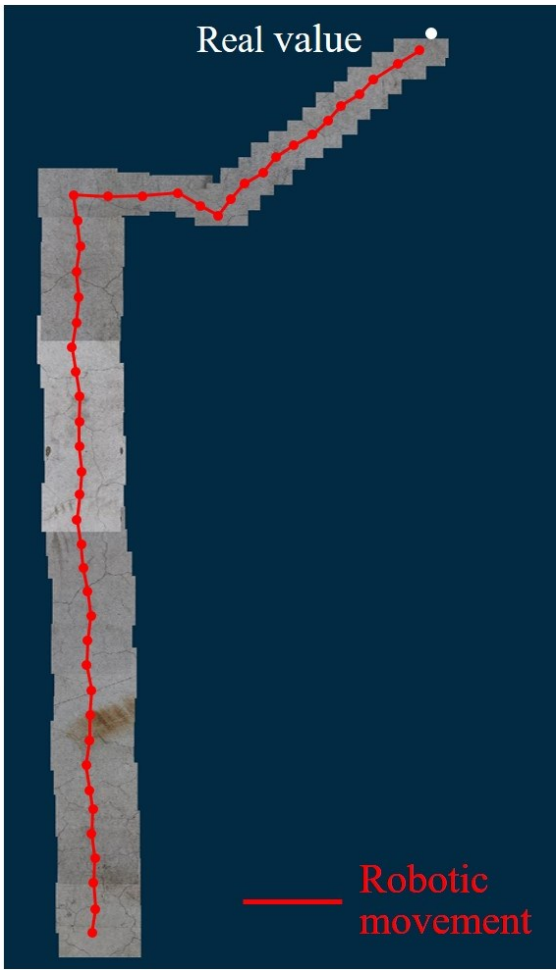

Figure 3.11 Mapping result of the robot from the second performance test

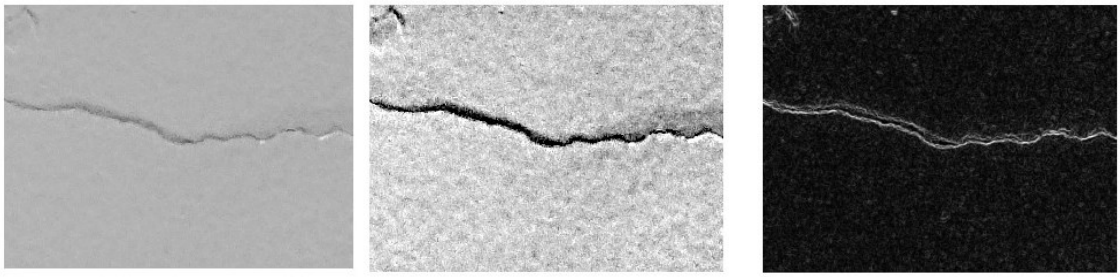

(a) (b)

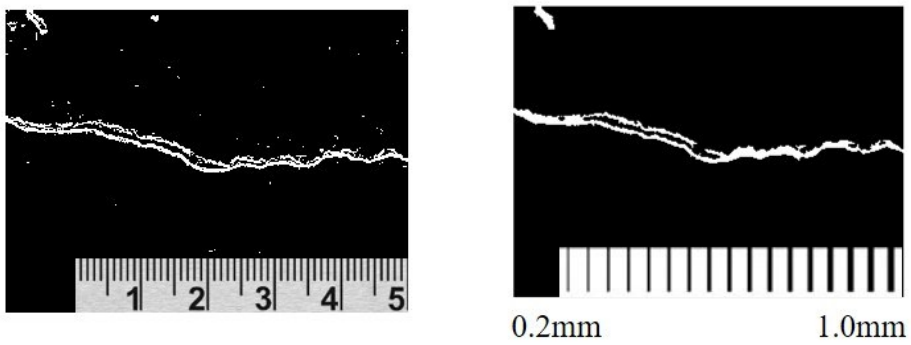

(c) (d)

Figure 3.12 Method to detect cracks in concrete components of steel bridges, (a) Original image and edge emphasis process, (b) Process of applying Gabor wavelet transformation, (c) Crack assessment process, (d) Noise reduction process

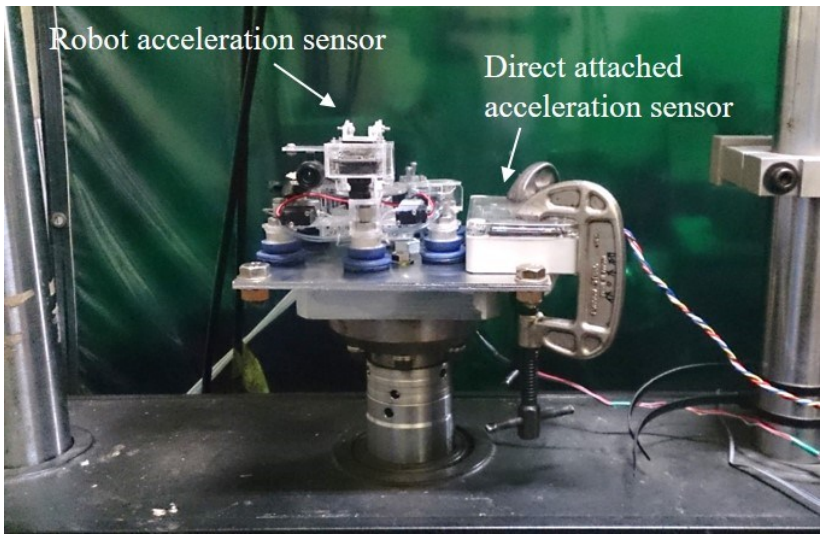

Figure 3.13 Sensor arrangements for the laboratory experiments to evaluate vibration characteristics of the inspection robot

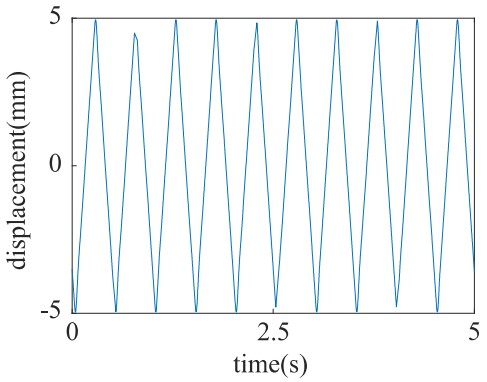

(a)

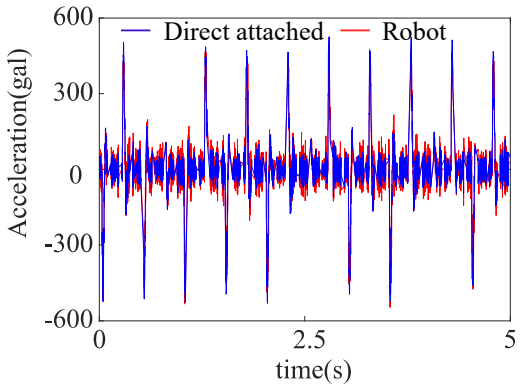

(b)

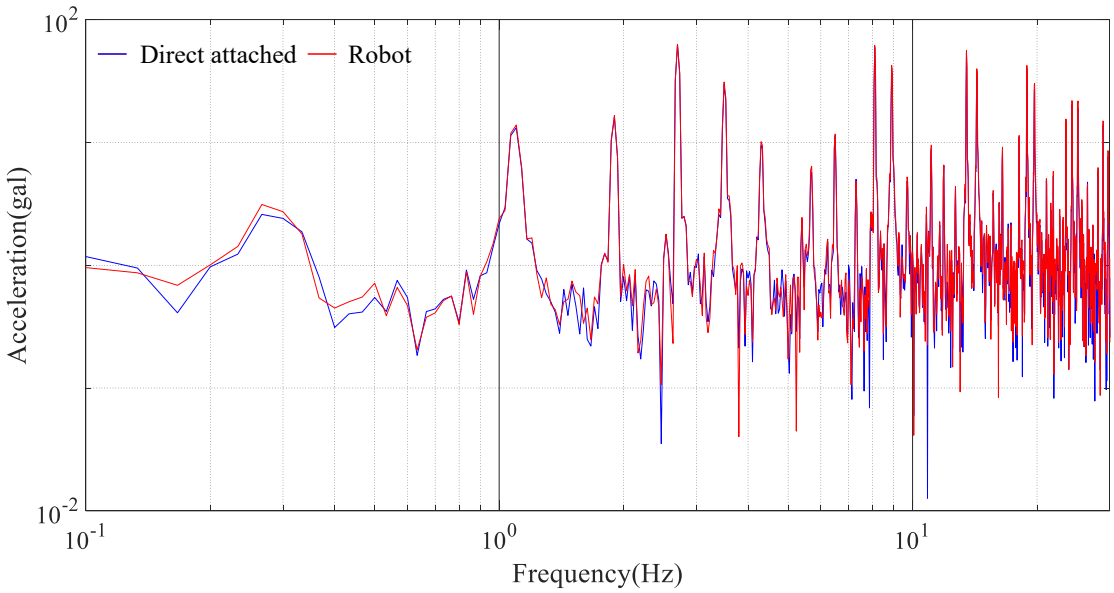

(c)

Figure 3.14 Input and output signal of the experiments, (a) Input triangular wave of 2 Hz, (b) Output acceleration wave, (c) Acceleration Fourier Spectrum from obtained acceleration data

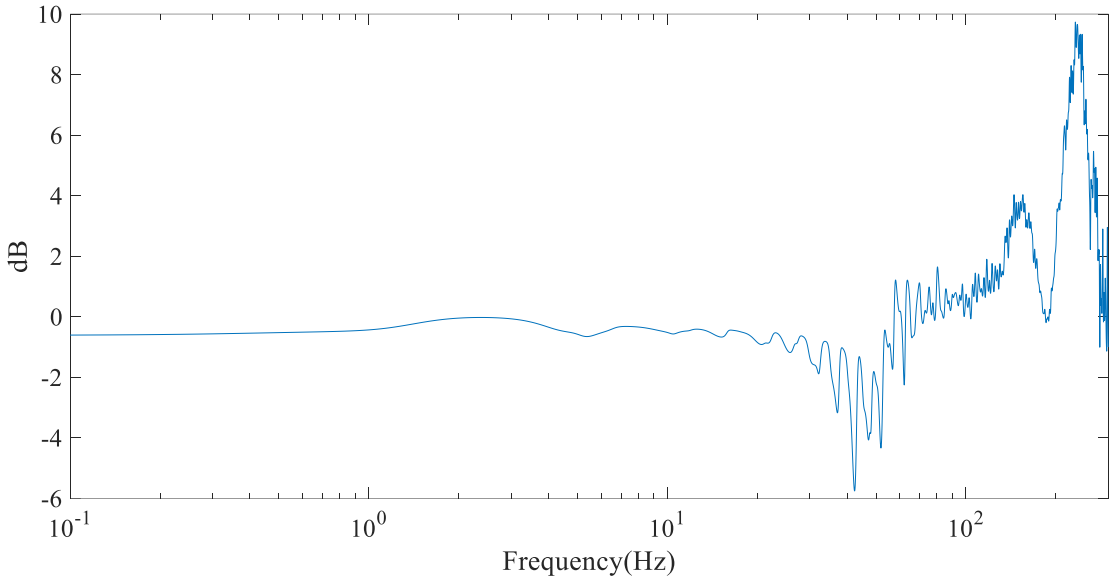
10
8
6
4
2
0
-2
-4
-6
dB
10^{-1}
10^{0}
10^{1}
10^{2}
Frequency(Hz)

(a)

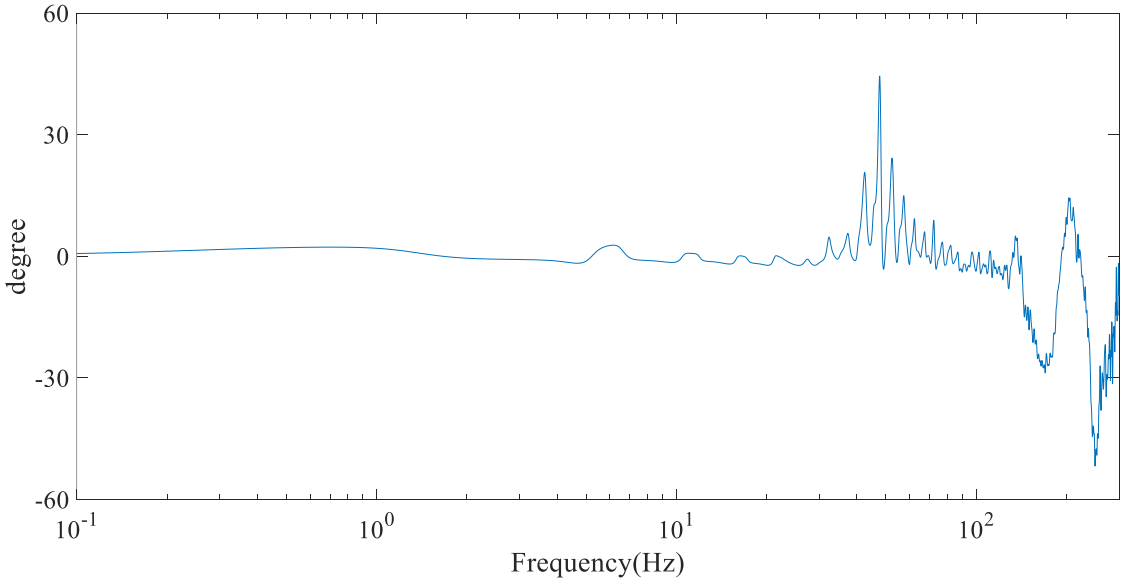
60
30
0
-30
-60
degree
10^{-1}
10^{0}
10^{1}
10^{2}
Frequency(Hz)

(b)

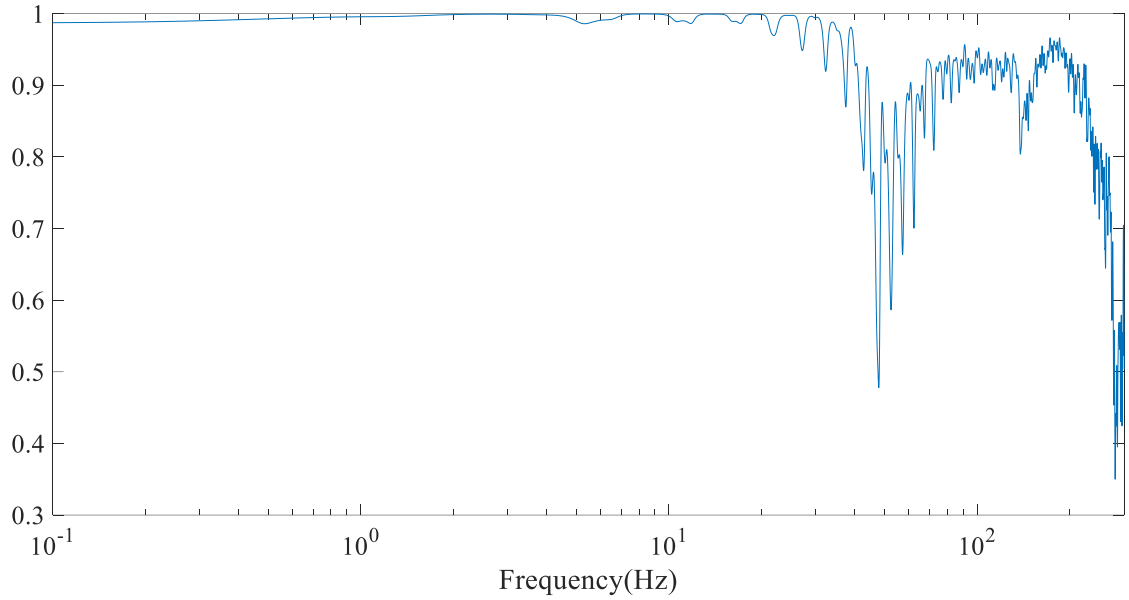

(c)

Figure 3.15 Gain, phase lag, and coherence as evaluation indexes, (a) Gain, (b) Phase lag, (c) Coherence

Figure 3.16 Measurement conditions when obtaining bridge vibration

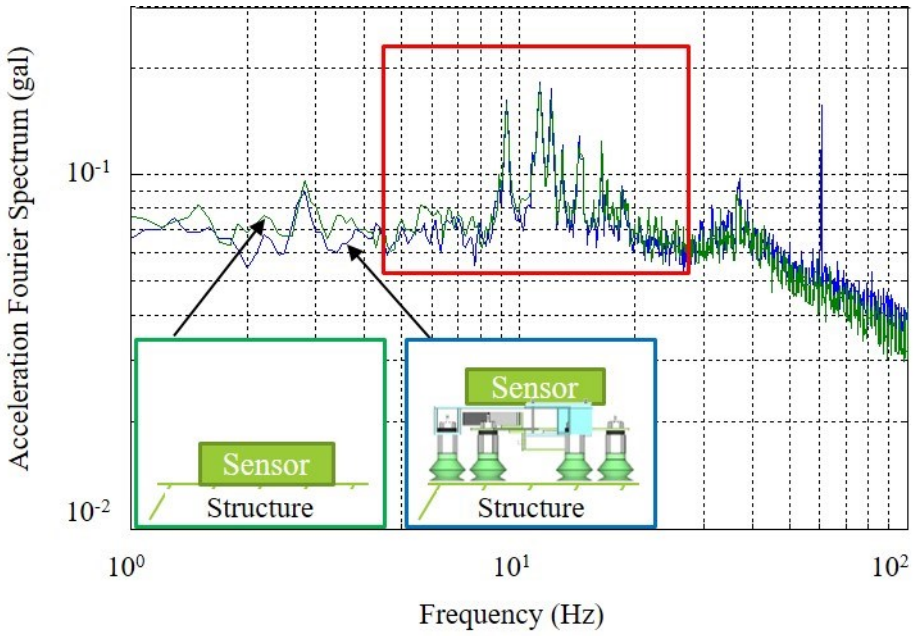

(a)

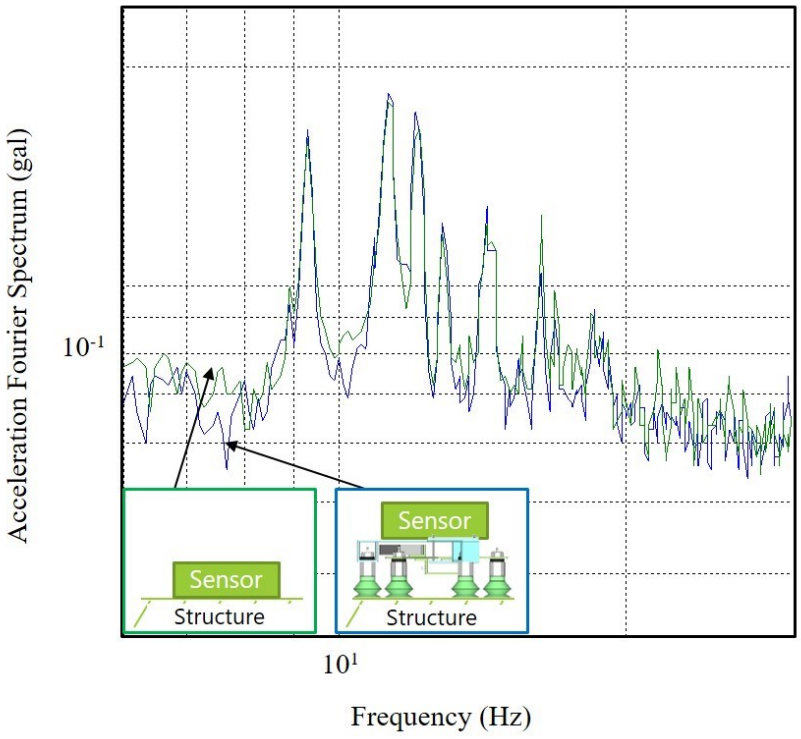

(b)

Figure 3.17 Experimental results of measuring bridge vibration, (a) Full Acceleration Fourier Spectrum, (b) Magnification

Table 3.2 Specification of microphone

Micro amplifier	Offset voltage	±0.2 mV (max: ±1mV)
	Input bias current	±0.2 pA (max: ±10 pA)
	Input voltage noise	8 μVrms
	Input voltage range	±0.3 mV
	Input impedance	10^{13} || 6 Ω || pF
	Output	1 mV
	Power supply	2.2 to 5.5 V
	Temperature range	-40 to 85 ℃
Condenser microphone	Diameter	9.7 mm
	Height	6.7 mm
	Sensitivity (0 dB = 1V / pA)	-42.0±2.0 dB
	Directivity	Omnidirectional
	Power supply	1.5 V
	Operating voltage range	1.0 to 10.0 V
	Maximum current	0.5 mA
	Terminal	PIN
	Housing material	Aluminum
	S / N ratio	More than 60.0 dB
	Frequency range	50 to 16000 Hz

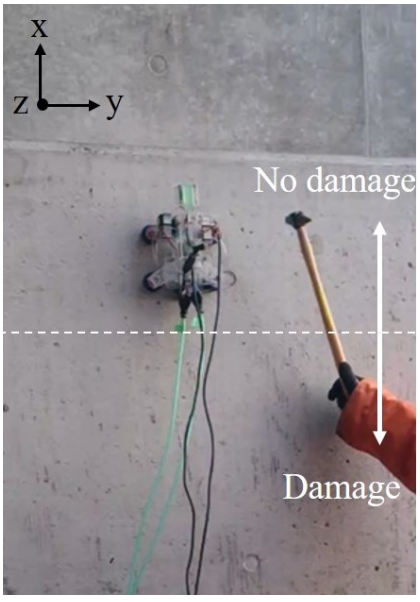

Figure 3.18 Condition of the robot during the hammering test

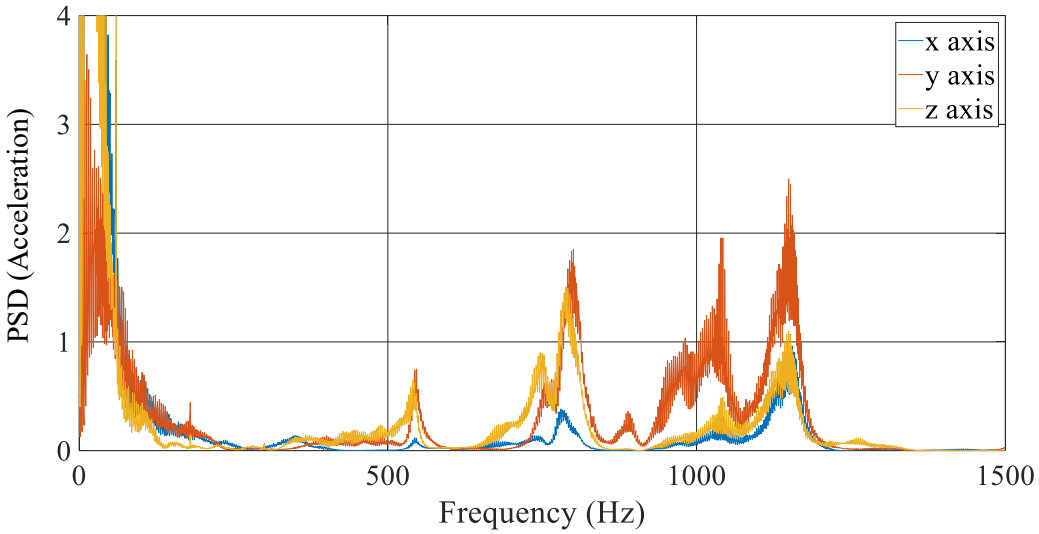

(a)

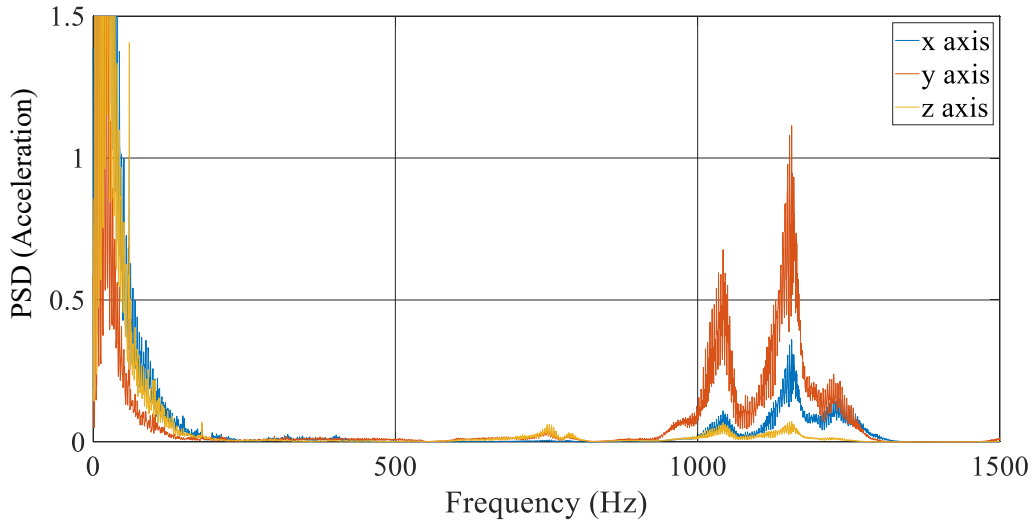

(b)

Figure 3.19 Hammering test results using the robot acceleration sensor, (a) Surface with an internal defect, (b) Healthy surface

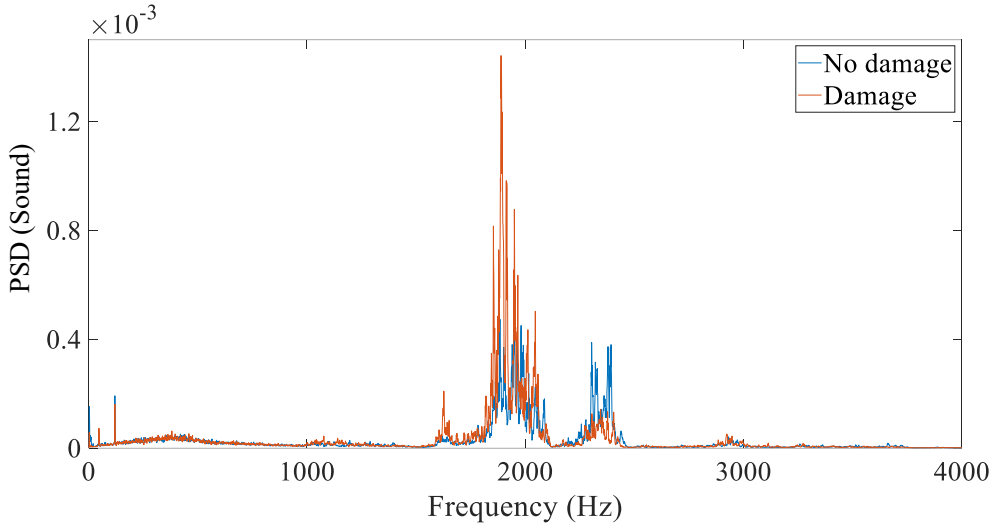

Figure 3.20 Hammering test results using the microphone

Table 3.3 Inspection condition and information of movement and inspection duration of the inspection robot

Inspection	
Target location	5 meters above set position
Measurement area	Width: 240 mm / Length: 200 mm
Inspection robot	
Movement time (Forward movement)	3 seconds
Movement time (10 degrees rotation)	5 seconds
Location identification time	5 seconds (average)
Measurement time	2.5 seconds
Time for taking pictures	2 seconds

Table 3.4 Calculation results of inspection duration

	Number of movements (During measurements)	Movement time	Location identification time (Measurement time)	Total operation time
Case 1	298 (98)	1430 s	1490 s (including 245 s)	49 min
Case 2	298 (98)	1430 s	190 s + (245 s)	31 min

Chapter 4

Proposal of Corrosion Damage Evaluation Method

Abstract

Corrosion causes severe damage to steel bridges. Therefore, by focusing on corrosion damage, a method which is able to concurrently analyze various corrosion damage conditions such as local thickness reduction or the formation of a rust layer on steel members has been investigated in this chapter. A method based on eddy current testing has been proposed. In this research, a relatively low frequency eddy current between 1 and 1000Hz has been considered for the proposed corrosion damage evaluation method, which performs inspection from only one side of a steel members. This method has the potential to be a simple non-destructive testing method. Moreover, this method can be used both as an independent measurement system as well as one of the robotic inspection functions.

4.1. Overview

In steel bridges, corrosion causes severe damage which consequently lowers the safety and durability of the bridge. Recently, many cases of traffic restrictions, reinforcement repair works and replacement work due to severe corrosion damage on steel bridges have been reported [24,68,109,110]. If significant corrosion occurs on main structural members and impacts a large area, the economic burden increases as the area requiring maintenance increases. Therefore, an inspection and measurement system specifically for corrosion damage is important.

Corrosion tends to occur in areas that are narrow or complex in structure as these areas are often humid or are not rain-washed. However, it is difficult to perform inspections of narrow locations and places where the arrangement of members is complicated. Moreover, it has been made clear through past research that corrosion damage lowers the load-carrying capacity of steel members [69-77]. Hence, much research has been carried out to develop evaluation methods of the remaining load- carrying capacity by using the ratio of the designed thickness to the residual thickness of steel members [71-77]. If it was possible to obtain the residual plate thickness of steel members during inspection, it would enable the remaining load-carrying capacity to be evaluated using one of the aforementioned evaluation methods, and thus be an effective inspection method for steel bridges. However, evaluating residual thickness by visual inspection using conventional inspection processes have proven difficult. Caliper or ultrasonic testing is methods have attempted to evaluate residual thickness, however these testing methods are limited due to the requirement of surface treatment and the large number of sections that are difficult to access. Hence inspection methods which require surface preparation should be avoided. In this research, eddy current testing was investigated for corrosion damage evaluation as it is one non-destructive testing method which does not require surface preparation. However, methods using eddy current in previous research [86-96] required relatively large power consumption and the need of large equipment, which poses a problem during field measurements. Although the use of small probes has also been investigated, there are still problems as the actual thickness range that can be measured is small and so it is difficult to detect detailed damage conditions such as the thickness reduction due to local corrosion.

In this chapter, a new approach to corrosion damage evaluation based on eddy current testing has been proposed. The inspection system was made compact and potable to detect local information with greater ease. To obtain corrosion damage information such as rust thickness and residual plate thickness, relatively low frequency eddy current, between 1 and 1000 Hz, was applied. Corrosion of steel members in actual structures can be distinguished by three patterns, where corrosion occurs on either the front or back surfaces or both surfaces, as shown in **Figure 4.1**. Moreover, considering the accessibility of actual structures, a method to acquire corrosion

damage conditions by taking measurements from either the front or back surface of member only was also examined as shown in **Figure 4.1**. To develop the proposed corrosion damage evaluation method, firstly, differences in output signal characteristics due to damage conditions were clarified using numerical simulation. Further data analysis was then carried out to investigate the differences in output signal characteristics. Next, a sweep wave that can obtain various information regarding plate thickness during one excitation was designed as the excitation waveform. An evaluation method using either a detected voltage or both a detected voltage and phase as indexes was then examined. The phase in this research focuses on the phase lag of an input current with respect to the detected voltage. Finally, based on the results of all the aforementioned steps, two corrosion damage evaluation methods that consider the characteristics of corrosion damage were proposed. One method uses only the detected voltage to evaluate corrosion damage, and the other uses both the detected voltage and the phase. Performance and efficiency of the two proposed methods were clarified by experiment. Furthermore, the proposed methods have been developed to be used as both an independent measurement system as well as one of the robotic inspection functions. Thus a method to install an eddy current probe onto the inspection robot and its consequent performance was also examined.

4.2. Basic Concept of Eddy Current Testing Method

Eddy current testing is one electromagnetic testing method used in non-destructive testing, and makes use of electromagnetic induction to detect and characterize surface and sub-surface flaws in conductive materials. Eddy current flows through conductive material surfaces when a coil that generates an alternating magnetic field is placed on the surfaces of conductive materials as shown in **Figure 4.2**. The conductor then generates an electromotive force that hinders the magnetic flux change through the conductor. This current is called eddy current from its shape. The eddy current phenomenon can be expressed by the model shown in **Figure 4.3**. The secondary coil substitutes a target conductor and hence can be considered as the resistance of the measurement target. **Figure 4.3(b)** shows a circuit diagram of **Figure 4.3(a)**. The left side of **Figure 4.3** is a primary coil and the right side is a secondary coil. The secondary coil represents the measurement target. In **Figure 4.3**, V_1 indicates the AC power source with a sinusoidal wave, and R_1 and R_2 indicate resistance, I_1 and I_2 indicate current, L_1 and L_2 show inductance, and ωL_1 and ωL_2 are reactance of the primary and secondary coil respectively. When an alternating current is passed through the primary coil, the inductance in the primary coil side L_1 creates a magnetic flux. An electromotive force is then generated in the inductance L_2 by the magnetic flux, and a current I_2 flows through the resistance R_2 connected to the inductance L_2. It should be note that R_1 is the coil resistance,

and the resistance of the measurement target is R_2. A secondary current, which flows to the secondary coil side, generates a secondary magnetic flux in a direction the cancels the magnetic flux of the primary current by the law of electromagnetic induction. This phenomenon changes the electromotive force due to the self-induction of the primary circuit. Therefore, the electromotive force of the primary circuit varies depending on the value of the resistance R_2 of the secondary circuit.

Penetration depth δ, which is considered to be an important parameter in obtaining plate thickness information, is determined from the frequency f of the excitation current, the relative permeability μ and the electric conductivity σ of the target conductors. The penetration depth δ represented by the following equation is the depth at which an eddy current of constant strength is generated in a target conductor and shows the value at which the eddy current is $1/e$ of the value at the surface. In addition, an eddy current can also exist deeper than the penetration depth, and its depth changes due to the presence of defects.

$$\delta = \frac{1}{\sqrt{\pi f \mu \sigma}} \qquad (m) \tag{4.1}$$

Based on Equation (4.1) the penetration depth becomes larger if a lower frequency is used. In addition, when performing the eddy current testing, the penetration depth is affected by phenomena such as eddy current loss in high frequency bands, as described later. In this research, the method to acquire corrosion information such as thickness of steel members was examined considering this particular phenomenon.

Detected voltage v_v is an important parameter in eddy current testing. The relationship between the detected voltage v_v and phase transition ϕ of the voltage based on a current and also impedance Z is expressed by the following equation.

$$v_v = V_m \sin(\omega t + \phi) \tag{4.2a}$$

$$Z = \sqrt{R^2 + (\omega L)^2} \tag{4.2b}$$

$$V_m = Z I_m \tag{4.2c}$$

Analysis and experimental results in this research have been evaluated using V_m in Equation (4.2c). That there are cases where evaluation has been performed by using an impedance plane in conventional eddy current testing [111,112] for surface or sub-surface crack detection. Therefore, rather than just using the detected voltage as an evaluation index, using the phase between the input current and the detected voltage as an evaluation index and the corresponding evaluation method will also be examined.

4.3. Numerical Simulation on Characteristics on Low Frequency Eddy Current

In this section, an analysis is performed assuming a difference in damaged condition due to corrosion of a steel plate using low frequency eddy current of 1 to 1000 Hz. The characteristics of the detected voltage and the phase in the eddy current testing is grasped in order to acquire the corrosion damage information such as thickness of rust layer and residual plate thickness. In this analysis, using a carbon steel flat plate model to obtain corrosion damage information. The rust layer and the residual plate thickness were modeled as lift-off, which is the relative distance between coil and conductor surface and plate thickness (**Figure 4.1**). Analysis was carried out using plate thickness, lift-off and excitation frequency as parameters, thus the influence of each parameter change on the detected voltage and phase was investigated.

The lift-off in eddy current testing includes position change by operations, coating films of members, corrosion depth due to corrosion products, and their combinations, yet operation problems are not handled in this research. Generally, since members are painted, lift-off is assumed corrosion depth and coating films. Moreover, there are also materials, which are without coating films such as weathering steels [19,21-23] so that lift-off in this study is treated as "corrosion depth or a composite of coating films and corrosion depth". In this research, 2-dimensional axisymmetric analysis by general-purpose physics simulation software COMSOL Multiphysics [113-115] was used.

4.3.1. Analysis Conditions

Since the eddy current testing is a non-destructive inspection method using electromagnetic phenomena, governing equation is given by Maxwell's equation. The frequency used for the eddy current testing in this research is a relatively low frequency therefore, terms relating to the displacement current in the Maxwell equation can be neglected. Equations satisfying the magnetic field are shown as follows:

$$\nabla \times \boldsymbol{B}/\mu = \boldsymbol{J} \tag{4.3a}$$

$$\nabla \cdot \boldsymbol{B} = 0 \tag{4.3b}$$

$$\nabla \times \boldsymbol{E} = -\partial \boldsymbol{B}/\partial t \tag{4.3c}$$

where $\boldsymbol{B}$ is magnetic flux density, $\boldsymbol{J}$ is current density, $\boldsymbol{E}$ is electric field, and μ is permeability. When conducting numerical analysis based on Equation (4.3a)-(4.3c), finite element analysis [111,113-116] on electromagnetism is performed using vector potential A defined by $\nabla \times \boldsymbol{A} = \boldsymbol{B}$.

In the analysis, a model in which a coil is placed in the center of the carbon steel plate was established to investigate the detected voltage and the phase characteristics to the plate thickness and lift-off signal. The analysis model is shown in **Figure 4.4**, physical property values of the materials are shown in **Table 4.1**, specifications of a coil used in this analysis are shown in **Table 4.2**, and variables used in the analysis are shown in **Table 4.3**. The eddy current probe used in this research is a mutual induction system consisting of two coils that are excitation coil and detection coil for both analysis and experiment. In the analysis, an alternating current is input to the excitation coil, and the voltage obtained through the detection coil is evaluated as a measured value. The soft iron shown in **Table 4.1** is used for the core, and the excitation coil and the detection coil are coils shown in **Table 4.2** respectively. The analysis in this research is not aiming to reproduce the experiment, but to grasp the tendency of the detection signal for connecting through to the experiment. Therefore, the coil and the materials are not limited to specific type, and the conditions shown in the tables are assumed. In the analysis of eddy current testing, the mesh size influences the analysis accuracy. For the consideration of the mesh size, using the penetration depth shown in Equation 4.1 and making it less than half of the penetration depth confirmed to capture the influence of eddy current loss well [117,118]. The input current is up to 1000 Hz in this analysis, and then the penetration depth δ at 1000Hz is 0.65mm. **Figure 4.5** shows an influence of mesh division on an eddy current loss which will be described. The horizontal axis shows the width per mesh layer in the steel plate which the eddy current flows, and it is normalized by the penetration depth δ. The vertical axis shows eddy current loss normalized by the minimum eddy current loss value We. Since the eddy current distribution can be accurately reproduced when the mesh of the steel plate is divided finely, it can be confirmed that the eddy current loss converges to a fixed value. As a result, it is able to consider that the mesh of the steel plate should be divided smaller than the penetration depth δ. In this study, in order to apply the eddy current testing in the thickness direction, therefore, minimum mesh size is selected to use 1/3δ, which is more accurate than 1/2δ, taking into consideration calculation time. Finally, the minimum element size which is 0.2 mm and maximum element size of 2.0 mm were selected for the analysis. The mesh division of the analysis model focused near coil and plate is shown in **Figure 4.6** and full mesh model applied aforementioned process is shown in **Figure 4.4**.

The value of the plate thickness is 9 mm as a healthy condition, from which 1 mm by one step of thickness reduction is simulated. In the eddy current testing, the permeability change of the steel was considered influencing to measurement results, however, since it is assumed that the change is small in the low frequency area used in this study, the permeability is assumed to be constant in this analysis. Changes in plate thickness were set assuming thinning due to corrosion, and changes in lift-off were set with the assumption of a presence of rust layer and a coating film for corrosion prevention. An alternating current 0.1 A was input to the excitation coil. The heating

value due to the eddy current is also taken into consideration in the model constitution formula.

4.3.2. Fundamental Characteristics of Detected Voltage in Eddy Current Testing

In this study, basic characteristics of the eddy current are grasped with the excitation waveform as a sinusoidal wave and sweep wave. Using detected voltage as an index. Analysis was carried out by changing a plate thickness, lift-off, and frequency as parameters.

First, a relationship between the detected voltage and the frequency is shown in **Figure 4.7**. **Figure 4.7** shows the case that lift-off is 0 mm and plate thickness is 9mm. It was confirmed by the figures that the detected voltage increases with the frequency increases. Since the magnetic flux which is penetrated conductors increases toward high frequency side, eddy current also actively flows accordingly.

Next, a relationship between the detected voltage and the plate thickness at each frequency is shown in **Figure 4.8**. The graphs indicate that the detected voltage increases as the plate thickness increases. In this research, the plate thickness is written as 'thickness' in figures. **Figure 4.9** shows an eddy current density distribution obtained by analysis. **Figure 4.9(a)** shows the eddy current density distribution at plate thickness of 6 mm and 9 mm. The lift-off is unified at 0 mm in **Figure 4.8** and **Figure 4.9(a)**. **Figure 4.9(b)** shows the eddy current density distribution at plate thickness of 9 mm with lift-off 0 mm and 0.3 mm. Since thickness at 6 mm and 9 mm show similar distribution tendencies, eddy current that was supposed to occur in the area corresponding to reduce the plate thickness disappears. Therefore, the detected voltage is thought to decrease. In addition, when lift-off occur the effective area of eddy current at plate surfaces becomes slightly bigger. On the other hand, the graph of **Figure 4.8(d)** shows peak at thickness 7 mm and then decreases. Phenomenon, which a peak appears at the point where the detected voltage gradually increases with increasing the plate thickness and then decreases, are also reported by Yamada et al [119,120]. This phenomenon is considered to be related to an eddy current loss. The eddy current loss is a phenomenon that eddy current changes power consumed in the conductor into heat and dissipates energy. It can be expressed by the following equation.

$$W_e = \pi^2 B^2 f^2 d^2 / 6\rho \tag{4.4}$$

Where, W_e [W/m^3] is eddy current loss, ρ is resistivity and d [m] is plate thickness.

From the above equation, it is conceivable that the higher the frequency, the thicker the plate thickness and the larger the eddy current loss becomes. As a result, it is considered that energy dissipates and then the detected voltage decreases. A ratio of eddy current loss to total energy consumption in the eddy current testing is showed in **Figure 4.10**. It is confirmed that the ratio of eddy current loss increases from around 100 Hz as shown in **Figure 4.10**, and this eddy current

loss may affect thickness detection.

Finally, a relationship between the detected voltage and the lift-off at each frequency is shown in **Figure 4.11**. It is confirmed that the detected voltage decreases as lift-off increases regardless of the frequency. Hence, it is considered that the more the coil separates from the target, the less the amount of magnetic flux penetrating target conductors, so that a strength of eddy current weakens. As a results, the lift-off estimation has possibility in high frequency area which is considered to be high in the focused frequency in this research, and thickness estimation is considered to be able to perform in low frequency area such as 1 Hz or 10 Hz.

4.3.3. Fundamental Characteristics of Phase in Eddy Current Testing

In this subsection, phase characteristics due to lift-off and plate thickness change were also grasped same as detected voltage.

Figure 4.12 shows the relationship between the phase and the frequency. It is known that when the sinusoidal AC voltage is applied to the coil, the phase of the current is delayed by 90 degrees with respect to the voltage. According to **Figure 4.12**, the phase decreases from 90 degrees as the frequency increases. It is assumed that the degree of the phase change varies depending on the properties of the conductor material and the coil to be applied. However, it is thought that it can be applied to various materials by grasping this phase characteristic for each material. As the frequency is higher, the eddy current prone to flow, further it influences the phase of the detection signal. Therefore, it is considered that the phase change is also affected by the frequency change.

Relationships between phase and lift-off at each frequency are shown in **Figure 4.13**. Here, the plate thickness is also unified to 9 mm which is a healthy condition. As can be seen from **Figure 4.13**, it can be confirmed that the phase increases with the increase of lift-off regardless of frequency. In the eddy current testing, the resistance of conductor affects to the detected voltage signal, therefore, the phase change due to the lift-off is considered to be a phenomenon caused by the change in the degree of magnetic coupling between the coil and the conductor.

Relationships between phase and plate thickness at each frequency are shown in **Figure 4.14**. The lift-off is unified at 0 mm which is a healthy condition. It is confirmed by the figures that the phase decreases with increasing plate thickness moreover, it is also confirmed that the difference is larger as the frequency is lower at 1 Hz or 10 Hz. It is similar tendency with the detected voltage, therefore, it can be considered the phase lag of the detected voltage changes similar to the its amplitude. The eddy current penetrates from the conductor surface toward the inside however, its transmission speed is a finite value determined by some parameters such as frequency. That is, the eddy current is transmitted at a finite speed thus the phase delays as it enters the interior.

In a case where the detected voltage is used as an index, eddy current loss, which is a

phenomenon that the eddy current changes power in the conductor into heat and energy dissipates, was confirmed. In the frequency range exceeding 100 Hz, the detected voltage tends to decrease due to energy dissipation owing to the influence of the eddy current loss. On the other hand, when the phase is used as an index, the difference in phase due to plate thickness change becomes smaller as the frequency becomes higher so that it is considered that measurement at 1000 Hz is difficult. Yet, since there is no change in slope, it is conceivable that the influence of eddy current loss is less likely to be affected than the detected voltage.

In the eddy current testing, it is known that the effect of electromagnetic induction decreases in the low frequency, the generation of eddy current weakens, the effect of permeability is strong, and the noise becomes large. It is considered that the effect of magnetic permeability is affecting that the difference of the phase is larger at 10 Hz than 1 Hz. In addition, it is known that electric conductivity of conductors also affects eddy currents. As the conductivity increases, eddy currents flow easily, thus sufficient eddy current can be flown even if the frequency is set to a relatively low frequency. Since the flow ability of the eddy current depends on conductors, it is not necessarily the same trend in all materials. However, it is assumed that the aforementioned tendency does not change significantly because the permeability and the electric conductivity are related to penetration depth and strength of the eddy current. Hence, it is considered to be independent of changes in plate thickness and lift-off. Note that, it is conceivable that this tendency is changed depending on the structure and material of the coil.

Based on the above analysis results and consideration, by using the phase as an index, the possibility of plate thickness was considered to be able to obtain even at high frequencies in this research such as 100 Hz and 500 Hz which is available of estimating lift off by detected voltage. This idea suggests a possibility to be able to perform a short time measurement.

Taking the all above analysis results comprehensively into consideration, the effect on lift-off and plate thickness of the detected signal can be expressed as in **Figure 4.15**. The curve in **Figure 4.15** is the transition of the detected voltage and the angle αbetween the detected voltage and the input current I, which is criterion, is shown as a phase. R represents a resistance, XL represents reactance, and V_R and V_L represent voltages applied to both ends of the resistance and the reactance, respectively. The model in **Figure 4.15** is an example simulating the fact that the damage progresses in the direction of the arrow and the thickness reduction occurred after the formation of the rust layer.

4.4. Proposal of Corrosion Damage Evaluation Method Focusing on Difference of Dynamic Magnetic Field Characteristics due to Damage Condition

In this section, based on the detected voltage characteristics and the phase characteristics caused by the differences in plate thickness and lift-off revealed by the numerical simulation in the previous section, methods which is for simultaneous estimation of the lift-off and the plate thickness from the obtained detected signal is proposed and investigated. From the analysis result in the previous section, it was confirmed the lift-off has a possibility to obtain by detected voltage in high frequency area such as 100 Hz or more. Moreover, it was confirmed that the plate thickness can be estimated low frequency with the detected voltage. In addition, using phase, the plate thickness is able to estimate in the high frequency over 100 Hz which was difficult to obtain by the detected voltage. Therefore, in this research, two corrosion damage evaluation methods were proposed and investigated their applicability. One method uses only detected voltage for estimating both the lift-off and the thickness, and the other uses both detected voltage and the phase. In the proposed methods, assuming the thickness reduction due to corrosion represents as plate thickness change and the existence of rust layer or a coating film for anticorrosion is assumed to be a lift-off change. Therefore, using proposed methods, it becomes possible to judge whether the damage is thickness reduction or formation of rust layer through measurement and further estimate degrees of damage. Characteristics of two methods are summarized in **Table 4.4**.

4.4.1. Investigation of Input Waveforms and Evaluation Indexes used in Proposed Method

In this research, in order to make a simple analysis method, a waveform that can acquire information such as depth and surface shape by one-time measurement was considered. As shown in Equation 4.1, since a penetration depth is frequency dependent, it is possible to obtain more information at once by having multiple frequency components. In previous research, pulse waves are widely used for thickness detection [86-90]. Nonetheless, since sweep waves whose frequency varies with passage of time [121,122] also contains many frequencies and the spectrum is already known, thus in this study sweep waves in addition to sine waves are selected. Considering number of waves at low frequency area, log sweep was adopted for excitation wave. Since the sweep waves have many frequency components and signal varies with time, it has possibility of detecting new information which cannot be obtained by sine waves. In order to make effective use of sweep wave, wavelet transformation which can see signal in time-frequency domain is attempted to use in this study. In addition, the wavelet transformation is effective in reducing electric noise therefore, reduction in S / N ratio can be expected in experiments using low frequency area. Even when using other waveforms in the future, it is considered possible to evaluate by the same

method, and it can be a simple method aimed at this research. In this study, Mexican hat with high versatility is adopted for mother wavelet, and expressed by following equation.

$$W_\psi[x(t)] = \frac{1}{\sqrt{a}}\int_{-\infty}^{\infty} x(t)\overline{\psi(\frac{t-b}{a})}dt \quad (4.5a)$$

$$\psi(t) = (1-t^2)e^{-0.5t^2} \quad (4.5b)$$

Where, $x(t)$ is original wave, $W_\psi[x(t)]$ is wavelet coefficient, a is scale parameter, b is shift parameter and $\psi(t)$ is mother wavelet which is Mexican hat. To analyze obtained detected voltage when the detected voltage is the evaluation index, wavelet transformation is applied and wavelet coefficient is used as an index instead of original detected voltage data. Example results applying wavelet transformation is shown in **Figure 4.16**. **Figure 4.16(a)** shows the case of exciting 1 to 100 Hz of sweep wave to the steel plate with plate thickness of 9 mm and lift-off of 0 mm. Figure 4.16(b) indicates the thickness signal strength using plate thickness 9mm and 8 mm. It can be confirmed that wavelet transformation can analyze data with time information. In this research, maximum values were used as evaluation index in each frequency. Then, relationships between wavelet coefficient and plate thickness at each frequency are shows in **Figure 4.17**. The tendency shows similar to **Figure 4.8** and **Figure 4.11** which are not applied wavelet transformation. Moreover, the value after applying wavelet transformation increases ten times more than original detected voltage data was confirmed. Thus, it was confirmed that the wavelet coefficient can be applied.

4.4.2. Corrosion Damage Evaluation Method Focused on Detected Voltage Characteristics

This method which uses only detected voltage as an evaluation index named hereafter CDE method (VV). From the detected voltage characteristics shown in the previous section, it was revealed that the lift-off change has a greater influence on the difference of the detected signal than the plate thickness change. CDE method (VV) is discussed using the influence of the differences of detected signals which applied wavelet coefficient.

In order to see the influence on the detected voltage signal due to the plate thickness change and the lift-off change for each frequency, a sweep wave of 1 to1000 Hz was excited. First, ΔWC_t and ΔWC_L shown in the following formulas were obtained as plate thickness signal intensity and lift-off signal intensity focusing on the change in detected voltage accompanying each lift-off and thickness change.

$$\Delta WC_t = WC(d) - WC(d_0) \quad (4.6a)$$

$$\Delta WC_L = WC(l) - WC(l_0) \quad (4.6b)$$

Where, d_0 is the reference value of the plate thickness, l_0 is the reference value of the lift-off, and d and l are the measured values, respectively. The plate thickness signal intensity when the plate thickness changes 1 mm and the lift-off signal intensity when the lift-off changes 0.3 mm are as shown in **Figure 4.18(a)** and **Figure 4.18(b)** respectively. In **Figure 4.18** conditions that lift-off of 0 mm and 0.3 mm, and plate thickness of 9 mm and 8 mm was used. In these figures, the most disadvantageous conditions within the range assumed in this research are shown as an example. However, since the lift-off change influences on the difference of the detection signal more than the change in the thickness, the thickness reduction of 1 mm considered to have the smallest difference in thickness signal strength was adopted as one of the disadvantageous conditions. In order to confirm the degree of influence of each difference, the ratio of the plate thickness signal strength and the lift-off signal strength is taken and the relationship with the frequency is shown in **Figure 4.18(c)**. The vertical axis in **Figure 4.18(c)** is a thickness lift-off signal intensity ratio (hereafter called TL signal ratio). The TL signal ratio shows a tendency to decrease as the frequency increases. Furthermore, it was confirmed that on the high frequency side most of the signals are caused by the lift-off, whereas on the low frequency side the ratio including the signal due to the plate thickness increases.

Target frequencies for estimating both the lift-off and the plate thickness is determined using these features. In this research target frequency is from 1Hz to 1000Hz. Based on the above characteristics, since the TL signal ratio (**Figure 4.18(c)**) is sufficiently small which means influence of plate thickness change is negligibly small and lift-off information is contained in a large amount, frequency is selected as a lift-off estimation frequency (f_L). In the selection of the lift-off estimation frequency, the frequency range which includes the influence of the eddy current loss needs to be excluded. Frequency range where eddy current loss is dominant shows the negative value in **Figure 4.18(c)** and is excluded. Lift-off signal strength is much bigger than thickness signal strength, therefore, excluding high frequency area influences by eddy current loss, 100 Hz is considered to be a lift-off estimation frequency (f_L). Using the sweep waveform is considered to be effective for calculating the TL signal ratio over a wide frequency range. Moreover, it is possible to capture the tendency considered to be different depending on the material at once. On the other hand, the frequency with the largest information on the thickness is 1 Hz. Therefore, a plate thickness estimation frequency (f_t) can be 1 Hz. However, in an actual measurement, the detected voltage in low frequency is small therefore, influence of experimental noise needs to be consider. The amplitude order of the 1 Hz sinusoidal wave is 10^{-3}, whereas the noise order was 10^{-4} and the value TL signal ration at 10Hz is close to 1 Hz. Therefore, in this method, the phase that can be more stably detected in the high frequency area is used as the index for plate thickness estimation. Finally, 10 Hz is selected for plate thickness estimation frequency (f_t). As summarize, a lift-off estimation frequency (f_L) has selected 100 Hz and a thickness

estimation frequency (f_t) was selected 10 Hz.

Figure 4.19(a) show a lift-off estimation curve (VV), that is the relationship between wavelet coefficient and lift-off at 100 Hz determined as the lift-off estimation frequency. It was confirmed that all lines show similar trend irrespective of plate thickness. From this relationship, it is possible to approximate the wavelet coefficient-lift-off relation used exponentially. **Figure 4.19(b)** shows a thickness estimation curve (VV), that is the relationship between wavelet coefficient and plate thickness at 10 Hz, which is the thickness estimation frequency. Regarding the wavelet coefficient-plate thickness relation, linear interpolation is used to perform approximation with multiple straight lines. Since the wavelet coefficient-plate thickness relationship changes not only by frequency but also by liftoff, the coefficient of the approximation curve is set as a function of the lift-off. **Figure 4.19(b)** is a result obtained by interpolating values of 0.2 mm from the results of lift-off 0.1, 0.3 mm then superimposing them.

Based on the above results, a flow for estimating lift-off and plate thickness in CDE method (VV) is shown in **Figure 4.20**. First, a database which is reference data used for measurement is constructed. Specifically, a sweep wave is excited in a calibration specimen so that data obtained by changing the frequency, plate thickness and lift-off is acquired. It is preferable that the calibration specimen is made of the same material as measurement targets. Thereafter, a TL signal ratio graph is created from the acquired data, and then frequencies f_L for estimating lift-off and f_t for estimating thickness are selected. Furthermore, a wavelet transform is performed on the detected voltage signal. The wavelet coefficient-lift-off relationship, which called hereafter lift-off estimation curve (VV), is created using the detected voltage at frequency f_L, and the wavelet coefficient -plate thickness relationship, which called hereafter thickness estimation curve (VV), is similarly created using the obtained lift-off in addition to detected voltage at frequency f_t. The process up to here becomes a database which uses when applying this method to measurement targets. Next, a measurement is performed on the actual measurement targets so that wavelet transformation is also applied to the detection waveform obtained there. The frequency step wave which connects two waves with lift-off estimation frequency and thickness estimation frequency was proposed to use in this method. The lift-off is estimated from the lift-off estimation curve (VV) and the value of the obtained detection waveform at the frequency f_L. Finally, using the thickness estimation curve (VV) and the value of the obtained detection waveform, the plate thickness is able to be estimated. Since t_{fL} in **Figure 4.20** represents from the surface to the healthy part on the back side, it is necessary to subtract the detected lift-off amount from the actual plate thickness t. Hereafter, corrosion damage evaluation method using detected voltage as the index named CDE method (VV).

4.4.3. Corrosion Damage Evaluation Method Focused on Phase Characteristics

In the CDE method (VV), in order to avoid the phenomenon of eddy current loss at frequency at 100 Hz where the eddy current loss becomes big at plate surfaces, thickness estimation frequency was selected in the low frequency side. In the previous section about analysis, the possibility of thickness estimation at high frequency area using phase was indicated. Therefore, in this section, CDE method (VP) which uses the phase for thickness estimation is investigated and proposed.

In the beginning of obtaining database is the same as CDE method (VV) until obtaining lift-off. In the CDE method (VV), the lift-off estimation has little error and has sufficient accuracy in the experiment discussed in next section so that the lift-off is estimated also using the detected voltage in this method. In addition, in the CDE method (VV), wavelet transformation is applied to the obtained detection signal with the main objective of noise reduction in the low frequency area, so that its coefficient was used as an index. To obtain the database, wavelet transformation is applied as it is because sweep wave is used and also including low frequency area. Besides, in lift-off estimation, it is assumed that only frequency area in which noises are difficult to be generated is assumed to be used, thus, to simplify data processing by using the originally detected voltage as an index. In contrast, in thickness estimation, attempting to use the phase which confirmed the acquisition potential in the previous chapter in the high frequency area. Applying a hybrid system which uses two indicators, it is considered that multilateral evaluation becomes possible. The lift-off estimation frequency was determined 100 Hz in the CDE method (VV). Therefore, in this method, attempting to use same frequency as lift-off estimation frequency to estimate thickness using phase. In this method, lift-off estimation frequency and thickness estimation frequency are same thus these two frequencies are collectively used as a corrosion damage estimation frequency (f_c).

After selecting the corrosion damage estimation frequency, a sinusoidal wave based on the selected frequency is input to the calibration specimen to obtain the lift-off estimation curve (VP) using detected voltage as an index and the thickness estimation curve (VP) using phase as an index are calculated. A lift-off estimation curve (VP), that is the relationship between detected voltage and lift-off at 100 Hz, which is the corrosion damage estimation frequency (f_c) is shown in **Figure 4.21**. As shown in **Figure 4.21**, it was confirmed that the same tendency is exhibited regardless of thickness even when the detected voltage obtained without applying the wavelet transformation. Therefore, it was indicated that the estimation can be performed at the corrosion damage estimated frequency without applying the wavelet transformation. Since it was also confirmed that this relation can be well approximated by an exponential function, this approximate curve is taken as a lift-off estimation curve (VP). On the other hand, **Figure 4.22** shows the relationship between the phase and thickness at frequency 100Hz. **Figure4.22** shows that each curve had similar intervals by lift-off and showed the same tendency. In addition, these

thickness estimation curves (VP) are subjected to poly-linear approximation by linear interpolation. Since this thickness estimation curve (VP) varies not only by frequency but also by lift-off, the coefficient of the approximation curve is set as a function of the lift-off. Thus, the thickness estimation curve (VP) is calculated using the value obtained by the lift-off estimation. All the points in the figure are values obtained by analysis. A broken line shown in Figure 4.22(c) is as an example curve obtained by interpolation from the value obtained by poly-linear approximation when the lift-off is assumed to be 0.2 mm.

Finally, a sinusoidal wave with corrosion damage estimation frequency is input to the measurement target to estimate the lift-off from the value of the obtained detected voltage and the lift-off estimation curve (VP). Then, the thickness is estimated from the thickness estimation curve (VP) calculated using the obtained lift-off value. Although it is preferable that the database is obtained for each measurement target, it is considered that it can be applied to a structure of a steel type having close characteristics. Moreover, this method that is using the original detected voltage without applying the wavelet transform to the lift-off estimation, suggests that the time on the calculation process can be shortened. It is necessary to subtract the detected lift-off amount from the obtained thickness to obtain an actual residual thickness same as CDE method (VV). Above process shows the corrosion damage evaluation method using phase characteristics proposed in this research, and **Figure 4.23** shows the flow of this method.

4.5. Experimental Evaluation of Proposed Corrosion Damage Evaluation Method

In this section, in order to examine the applicability of the two corrosion damage evaluation methods proposed in the previous section, an experiment was conducted to apply the proposed method to a steel plate having corrosion damage. A database was obtained using a stepped steel plate assuming thickness reduction due to corrosion as a calibration specimen and the rust thickness and residual thickness of the actual corroded specimen were estimated. All the experiments were carried out in this study five times in each place and evaluated using the average value. It was confirmed that the variation in five trials was about ± 0.0003 mm. A transfer function is used to calculate the phase in the experiment. The relationship between the input and the output waveform is expressed as follows using the transfer function. In the experiment, the transfer function is calculated from the power spectral density of the input and output waveform. Then the phase is calculated by using the obtained transfer function.

$$V(s) = G(s) \times U(s) \tag{4.7a}$$

$$G(s) = P_{yx}(f) \times P_{xx}(f) \tag{4.7b}$$

$$\phi = \arg(G(s)) \tag{4.7c}$$

Where, $G(s)$ is the transfer function, $U(s)$is the Laplace transform of the input waveform, $V(s)$ is the Laplace transform of the output waveform, $P_{yx}(f)$ is the cross power spectral density and $P_{xx}(f)$ represents the power spectral density of the input waveform. In the experiment, the phase is calculated by using Equations (4.7b) and (4.7c).

4.5.1. Measurement System

The measurement system used in this research realizes measurement with a small eddy current probe. It consists of a measurement probe (magnetic coil), a signal generator that generates an input wave, a data logger that records detection signals and laptop computer which control the signal generator and the data logger (**Figure 4.24**). This system is considered to be a mechanism with a simple configuration, further high filed applicability from the standpoint of power consumption.

Table 4.5 shows the specifications of the measurement probe used in this research. As shown in the table, the probe used in this study is compact and can obtain detailed information even compared with the existing plate thickness measurement system, in addition, it can be used for narrow members. The coil can connect four cables. Therefore, it can be confirmed there are two coils such as excitation coil and detection coil same as analysis. The calibration specimen used in this research shown in **Figure 4.25**. Assuming a thickness reduction of 1 mm, the calibration specimen is made into a four-step staircase shape from 9 mm to 6 mm. Here, the thickness of 9 mm is regarded as a healthy part. Lift-off in the experiment is measured in units of 0.1 mm by inserting a plastic gauge between the calibration specimen and the coil. Since the signal generator used in this research is voltage control, the input current is obtained by connecting a shunt resistor (**Figure 4.24**), which is a resistor for current detection to detect the circuit current, in series with the circuit and measuring the potential difference across the resistor.

4.5.2. Measurement to Obtain Database

4.5.2.1. Selection of focused frequencies

First, using a calibration specimen to obtain detection signal with changing the lift-off from 0 mm to 0.3 mm at each plate thickness of 9 mm to 6 mm by inputting sweep wave. Considering the analysis result, log sweep wave which changes from 10 Hz to 500 Hz is generated for 500 seconds in order to aim at a database of higher accuracy. The signal generator using in this research is voltage control therefore, amplitude of all waves using in this experiment was selected 5V. Since

it is voltage control, input current is not stable at each measurement. Therefore, in this experiment the output signal obtained was calibrated by setting the input current to the same amplitude. The following results show the values after applying calibration.

Figure 4.26 shows the plate thickness signal strength (ΔWC_t) using plate thickness of 9 mm and 6mm at the lift-off of 0 mm. The thickness signal strength is not shown negative values in the experiment yet the tendency is similar to the analytical results. **Figure 4.27** shows the lift-off signal strength (ΔWC_L) based on the lift-off of 0 mm and 0.3 mm when the thickness is 9 mm. Although it showed a peak at 500 Hz in the analysis, it was confirmed that the calibration specimen showed a peak at 100 Hz and gradually decreased. The result that the peak is shown at a certain point then decrease is similar to the analysis. The difference between the analysis and the experiment is considered to be attributable to the assumption that there are some differences in the core material and the core structure of analysis and experiment. In addition, the material or physical properties were assumed values, therefore, they are not exactly same as the experiment. The influence of experimental equipment is also considered.

Figure 4.28 shows the TL signal ratio obtained by the experiment. At low frequency area, the influence of thickness signal strength is large, and the tendency that the influence of the lift-off signal strength became stronger toward higher frequencies was confirmed. This trend is similar to the analysis. A rattling of the signal on the high frequency is considered to occur by the thickness signal being unstable due to the influence of the eddy current loss.

The frequency at 100 Hz which the TL signal ratio is sufficiently small and has the largest lift-off signal strength is considered to be appropriate as both the lift-off estimation frequency for the CDE method (VV) and the corrosion damage estimation frequency for the CDE method (VP). In addition, the frequency where includes the much thickness information is considered to be 10Hz. The frequency at 10 Hz is appropriate to the thickness estimation frequency. From the above, it can be possible that thickness and lift-off can be estimated by the proposed methods in the previous chapter. It is conceivable that the lift-off signal strength, plate thickness signal strength and the TL signal ratio are different depending on the materials so that it is necessary to obtain it in advance as a database. It becomes an advantage that it is possible to confirm the effect of magnetic permeability or eddy current loss since it is possible to see various frequency bands individually by exciting a sweep wave.

4.5.2.2. Obtaining lift-off and thickness estimation curve in CDE method (VV)

Data at the excitation frequency of 100 Hz are extracted using 16 different detection signals respect to lift-off change and thickness change obtained initially. The TL signal ratio shows the frequency with the largest information on the thickness is considered to be 10 Hz. The reason which 1 Hz is not selected even the thickness information is more than 10 Hz is noise effect as

mentioned in previous section. Therefore, the results of the experiments show the lift-off estimation frequency (f_L) is 100 Hz and thickness estimation frequency (f_t) is 10 Hz in the calibration specimen. **Figure 4.29** shows the lift-off estimation curve (VV) which is the wavelet coefficient-lift-off relationship at 100 Hz and **Figure 4.30** shows the plate thickness estimation curve (VV) which is the wavelet coefficient-thickness relationship at 10 Hz. It can be confirmed that the same trend as the analysis is shown. In addition, in **Figure 4.30**, it was confirmed that it was possible to superimpose values of 0.2 mm interpolated from the results of lift-off 0.1, 0.3 mm by the same method as the analysis. Moreover, in this method, possibility of estimating thickness thicker plate was considered because the penetration depth in low frequency is larger than high frequency. **Figure 4.31**, **Figure4.32** show the lift-off estimation curve and thickness estimation curve using thicker calibration specimen with steps from 16 mm to 19 mm. This result indicates that the possibility of thickness estimation of thicker plate using CDE method (VV). Moreover, **Figure4.31** indicates lift-off is able to estimate without considering thickness.

4.5.2.3. Obtaining lift-off and thickness estimation curve in CDE method (VP)

To obtain lift-off and thickness estimation curve, sine waves applied to excitation wave. However, to confirm the condition of measurement sites, using sweep same as obtaining the TL signal ratio was used to obtain calibration reference. The condition of performing measurement is always different such as AC frequency or condition of ground. Specifically, sweep waves are excited to the calibration specimen (for example, with a thickness of 9 mm and a lift-off of 0 mm, etc.) as a reference, before starting measurement and then, the result is compared with the reference data obtained by this experiment. By subtracting it as an error due to measurement conditions, errors in the experimental environment can be eliminated. As an example of obtaining data, **Figure 4.33** shows the relationship between the phase and the frequency of thickness 9 mm with lift-off 0 mm and lift-off 0.3 mm and 8 mm with lift-off 0 mm. The results indicate that the tendency of analysis is able to capture by experiments, further the phase differences related to lift-off and thickness are well obtained.

Obtaining the TL signal ratio confirmed that the corrosion damage estimation frequency is appropriate at 100 Hz for the specimen used in this method. **Figure 4.34** shows the relationship between detected voltage and lift-off which is the lift-off estimation curve (VP). From the fact that the detection signal becomes smaller as the lift-off becomes larger, which is a feature when using the detection voltage as an index, it can be considered that the thickness of rust layer of the measurement target can be estimated using **Figure 4.34**. In addition, the proposed CDE method VP) which is not applied wavelet coefficient shows the similar lift-off estimation curve (VV) as CDE method (VV) which perform wavelet transformation to detected voltage, thus it is considered to be able to shorten the time in data processing and to have high applicability in the

field measurement.

Figure 4.35 shows the relationship between the phase and the thickness which is the thickness estimation curve (VP). It showed the same trend as the analysis in which the amount of change increases with decreasing plate thickness. Although there was concern that the difference in the amount of phase change in the analysis was small, it was confirmed that it shows a sufficient difference for estimation. All the points in the figure show the experimental values furthermore, the broken line at the lift-off of 0.2 mm shows the curve calculated by poly linear approximation using the values of lift-off 0.1 mm and 0.3 mm. Since it was confirmed that the approximate curve shows good agreement with the lift-off of 0.2 mm in the experiment, it was confirmed that the thickness estimation curve can be calculated from the lift-off value obtained from the lift-off estimation curve. As mentioned above, it is able to estimate the residual thickness of measurement target using the relationship of **Figure 4.35**.

It was confirmed the phase at 100 Hz taken out from the sweep wave and the phase obtained using sine wave at 100 Hz were equivalent. Therefore, the values obtained by exciting the sine wave to measurement targets can be used to estimate the plate thickness and the lift-off by applying the values to estimation curves.

4.5.3. Measurement Experiment using a Corrosion Specimen

From the above results obtained by experiments using the calibration specimen, it shows the possibility of estimating lift-off and plate thickness with both CDE methods. In this section, an estimation of the rust thickness and the residual thickness of a steel plate which has corrosion damage collected from the actual structure (hereafter named corrosion specimen) using the lift-off estimation curves and the thickness estimation curves was performed. Corrosion specimen using in this experiment shows in **Figure 4.36**. P1, P2 and P3 indicate the measurement points. The probe was placed directly at the measurement point to carry out the measurements. The rust layer was not removed and the back surface shape was measured using a laser displacement meter. Moreover, it was evaluated as thickness reduction due to corrosion. The rust layer as the lift-off in this experiment was measured using a film thickness meter. **Figure 4.37** shows the back surface shape of the corrosion specimen measured with a laser displacement meter. The rust thickness and the residual thickness of the corrosion specimen were determined from the measurement results of the laser displacement meter and the film thickness meter, thus the obtained values were used for the evaluation. Note that the measurement with the laser displacement meter is a value including the rust layer, so that the residual thickness is evaluated by subtracting the rust layer. Since the residual thickness in the proposed method assumes the average value of the probe area which is the influence range of the eddy current as the measurement value, a value averaged by the area of the coil around the measurement point is calculated as the residual thickness of the

corrosion specimen. Excitation wave in the CDE method (VV) uses two wave which are lift-off estimation frequency and thickness estimation frequency. Considering each wave number, a 100 Hz wave for 5 seconds and a 10 Hz wave for 30 seconds was decided to generate. For the CDE method (VP) uses the data obtained by the lift-off estimation frequency. Although it is possible to shorten the measurement time, it was set to include many wavenumbers to improve accuracy in this experiment.

Figure 4.38(a) shows the lift-off estimation result and **Figure 4.38(b)** shows the plate thickness estimation result. Both the lift-off estimation and the plate thickness estimation is evaluated using wavelet coefficient of detected voltage in the CDE method (VV). The lift-off estimation is used the original detected voltage without applying the wavelet transform then thickness estimation is performed using the phase in the CDE method (VP). The values of Real in the figure was obtained by the film thickness meter and the laser displacement meter. As shown in **Figure 4.38(a)**, the rust thickness of Real and the rust thickness calculated as the lift-off by the CDE methods were all evaluated to be less than 0.1 mm, so that good agreement results were obtained. The errors of both CDE methods are almost same. Therefore, it can be considered that since frequency at 100 Hz includes not big noise, process of applying wavelet transformation can be excluded in the lift-off estimation process of CDE method (VP). The measurement values obtained by the both CDE methods are calculated using a database therefore, the values are set to conform to the measurement accuracy of the film thickness meter.

On the other hand, in thickness estimation in the voltage method, it was confirmed that the maximum error was around 8%. In this research, the errors less than 10% is considered to be accepted. Therefore, CDE method (VV) was confirmed to have enough accuracy. As for the thickness estimation in CDE method (VP), it was also confirmed that error of each measurement point can be calculated with an accuracy of less than 5% as shown in **Figure 4.38(b)**. Therefore, it is able to confirm that the errors are reduced by the CDE method (VP).

It was also confirmed that the influence of measurement error did not significantly affect the estimation results. As a result, it has been indicated that the thickness of rust layer and the residual thickness of the corroded steel member can be experimentally well evaluated by both CDE method proposed in this research. In the CDE method (VV), it was necessary to use two different frequencies. However, it was confirmed that by using proposed CDE method (VP), it is possible to obtain two corrosion damage information such as rust thickness and residual plate thickness only with one frequency. In fact, the maximum error is about 5% and the measurement time per point is around 5 seconds thus, the measurement realized labor saving by improving the accuracy and shortening the measurement time. On the other hand, using low frequency to estimate thickness in the CDE method (VV), it has possibility of applying thicker plate (**Figure 4.31, Figure4.32**). Moreover, since there are some differences in factors such as eddy current loss or

electrical conductivity which influence the detected voltage and phase respectively, and degree of influence, it is conceivable that each CDE method can be selected according to the characteristics of measurement targets. On the other hand, the error characteristics at each measurement point are consistent in both methods hence the influence of the measurement error in the laser displacement meter or the film thickness meter realized as Real in **Figure 4.38** is considered. Furthermore, in the eddy current testing, the eddy current decreases as it proceeds to the inside of the plate, so that there is a possibility that the eddy current does not coincide with the probe area. Although it is reported that the influence of the rust layer is small in the measurement with an electromagnetic type thickness meters [123], there is a possibility that rust having electric conductivity may be contained in the corrosion product. Thus it is necessary to investigate for the future works. Additionally, the lift-off estimation using the amount of phase change is considered to be possible from the analysis result, even though it was not considered in this research, therefore, it will also be investigated in the future works.

4.6. Application of Proposed Corrosion Damage Evaluation Method to Robotic Inspection

According to the above experiments, the corrosion damage evaluation method was established as one inspection method. In this section, implementing this CDE method to the robotic inspection function was investigated. The problem of implementing this method directly to the inspection robot is the size of the probe. The needs of the inspection robot are to perform inspections on the part that is narrow or difficult to access, so the inspection robot is made relatively small. In order to keep this concept and to reduce a burden on the robot, a smaller probe than probe used in the previous section was decided to introduce. The specifications of the small probe are shown in **Table 4.6**. The probe used up to the previous section is referred to as a φ23.7 probe, and the probe used for installing to the inspection robot is named a φ10 probe. It is assumed that detection system is same as the φ23.7 probe which is the mutual induction system consisting of the excitation coil and the detection coil. In this section, database acquisition experiments using small coil were conducted to confirm the applicability of φ10 probe and the versatility of CDE method. All conditions except the probe type. CDE method (VP) has ability to measure each point faster than CDE method (VV). Therefore, in this study, a verification experiment on the CDE method (VP), which is a more convenient method considering the installation to the inspection robot was conducted.

4.6.1. Measurement to Obtain Database

In the same way as acquiring the database with the φ23.7 probe, first obtain the TL signal ratio to select corrosion damage estimation frequency. Sweep waves are input to the calibration specimen to obtain the detection signal which is acquired by changing the thickness and lift off, respectively. **Figure 4.39** shows the lift-off signal strength (ΔWC_L) using the lift-off of 0 mm and 0.3 mm when the thickness is 9 mm. Although it does not show a clear peak as the φ23.7 probe, the tendency that it rises to 300 Hz and then shows a downward trend was confirmed. For this reason, it is assumed that the lift-off of the detection signal and the strength with respect to the plate thickness change depending on the probe specification such as the shape or the material of the core. **Figure 4.40** shows the TL signal ratio of φ10 probe. At the low frequency, the influence of the plate thickness signal was large, and as the frequency became higher, the tendency was predominantly governed by the influence of the lift-off. The corrosion damage estimation frequency in the φ10 probe is 300 Hz since the lift-off signal strength is sufficiently large and the influence of the plate thickness disappears. In addition, the frequency area where the TL signal ratio shows negative value is excluded. Since the penetration depth at 300 Hz becomes smaller than 100 Hz, it may possible to be difficult to detect the plate thickness. However, the penetration depth is a reference value therefore, 300 Hz is selected for φ10 probe and experiments to obtain plate thickness estimation curve and lift-off estimation curve are attempted to obtain.

Figure 4.41 shows the relationship between detected voltage and lift-off which is the lift-off estimation curve (VP_φ10). The wavelet transformation was not performed to detected voltage. The value of the detected voltage in the φ23.7 probe was 1.0 V with the lift-off of 0 mm however, it was 0.06 V in the φ10 probe. Although the detected voltage was small even at 300 Hz, it was confirmed that the graph shows the same trend as lift-off estimation curve obtained using φ23.7 probe. This result indicates the possibility of lift-off estimation using obtained curve shown in **Figure 4.41**.

Figure 4.42 shows the relationship between the phase and the frequency. The area of low frequency such as under 100Hz is excluded due to noise and too small detected voltage to use for evaluation. The graph indicates the same tendency which shows the phase becomes small as the frequency increases, as φ23.7 probe (**Figure 4.33**). **Figure 4.43** shows the relationship between the phase and the plate thickness which is the plate thickness estimation curve (VP_φ10). The phase becomes large as the thickness becomes small. This is the same tendency as φ23.7 probe. However, the phase becomes small as the lift-off becomes large. This is the opposite tendency to the φ23.7 probe. The possible reason of this difference is coil specification such as size, number of turns or position of both detection coil and inducing coil. To confirm the size effect of coils, a further smaller coil which the diameter of the probe is 7 mm is used. Results indicate the same tendency as the small coil. Therefore, aforementioned reason can be considered. On the other

hand, regardless of this difference, it can be confirmed the clear difference with both the lift-off and the thickness. Hence, it is able to consider the possibility of estimating thickness with obtained thickness estimation curve.

All the points in the figure show the experimental values furthermore, the broken line at the lift-off of 0.2 mm shows the curve calculated by poly linear approximation using the values of lift-off 0.1 mm and 0.3 mm. Since it was confirmed that the approximate curve shows good agreement with the lift-off of 0.2 mm in the experiment, it was confirmed that the thickness estimation curve can be calculated from the lift-off value obtained from the lift-off estimation curve. As mentioned above, it is able to estimate the residual thickness of measurement target using the relationship of **Figure 4.43**.

4.6.2. Measurement Experiment using a Corrosion Specimen

In this section, using the above estimation curves of lift-off and thickness obtained by experiments using the calibration specimen, the applicability of the φ10 probe to corrosion specimen was confirmed. The corrosion specimen and other conditions except the probe are same as the previous experiments. In the φ10 probe experiments, the corrosion damage evaluation frequency of 300 Hz was used therefore, the measurement time per each point can be reduced to 1 second.

Figure 4.44(a) shows the lift-off estimation result and **Figure 4.44(b)** shows the plate thickness estimation result. Since the size of the probe became small, the effective area of eddy current became also small. Therefore, the values of Real are slightly changed and the φ10 probe is considered to be able to obtain more local information than the φ23.7 probe.

As shown in **Figure 4.44(a)**, the thickness of rust layer in Real and the rust thickness calculated as the lift-off by the CDE method were all evaluated to be less than 0.1 mm, so that it can be considered the CDE method (VP) with the φ10 probe (named hereafter CDE method (VP_φ10)) has enough accuracy.

On the other hand, in plate thickness estimation using the φ10 probe, it was confirmed that the maximum error was around 7%. In this research, the errors less than 10% is considered to be accepted. Therefore, the φ10 probe was confirmed to have enough accuracy even at frequency 300 Hz. This results indicate the measurement time per point can significantly reduce. Moreover, the inspection robot has interval time in each movement. Therefore, this measurement time reduction can be advantage to install the φ10 probe to the inspection robot since it shows the possibility of inspection while robot is moving.

4.6.3. Investigation of Installing Method of Small Eddy Current Probe on the Proposed Inspection Robot

In the previous section, applicability of CDE method (VP_φ10) was confirmed. In this section,

concretely the method of installing this φ10 probe to the inspection robot was examined and the applicability in the condition where the φ10 probe was installed on the inspection robot was verified. Since various influencing factors such as vibration can be considered when installing the φ10 probe to the inspection robot, efficient installing method and applicability were verified using the corrosion test specimen. Furthermore, the movement performance of the inspection robot in the condition where the φ10 probe was installed, was confirmed on a corrosion surface and a concrete surface.

An attachment condition of the probe to measurement surfaces is important in case of installing the φ10 probe to the inspection robot to estimate rust thickness and thickness with good accuracy. In addition, it is necessary to eliminate the physical influence such as vibration or to subtract influences by comparison with the reference value obtained with calibration specimen. The experiments discussed in previous sections, the probes were placed directly on the specimen, and accuracy was secured without touching the probe during measurement. As mentioned earlier, as lift-off is greatly influenced and it is heavily involved in thickness estimation accuracy, therefore, constantly management of lift-off is the most important. At the time of air pad is attached or not attached to surfaces, the body of the inspection robot moves about 8 to 10 mm up and down.

The inspection robot advances while repeating attachment and non-attachment by the air pads. In this mechanism, during movements, it is considered difficult to measure while constantly controlling the lift-off, therefore, it is expected that the measurement is carried out when the robot is fully attached to surfaces in the end of each movement. Assuming that the measurement is performed in practice, data can be acquired at intervals of about 20 mm. In consideration of aforementioned conditions, the mechanism by which the probe attaches to target surfaces was investigated with the height of the robot fully attached as a reference.

In order to make fully attachment of the probe, a sponge air pad using a chloroprene sponge used for a sponge bellows air pad was applied. Diameter of this sponge air pad is 15 mm. A probe holder for attaching the φ10 probe to the inspection robot was made using a 3D printer and attached it to the back side of the inspection robot. The probe holder has four sponge air pads which is for actualize fully attachment. The probe holder and the condition of installing it to the inspection robot are shown in **Figure 4.45**. As shown in the figure, when the inspection robot is not attached to surfaces, the probe holder is floating from the surface about 10 mm. It is considered to be able to remove the influence of lift-off at the maximum by attracting the sponge air pad to make a state of firmly attaching to target surfaces when the inspection robot is fully attached to surfaces.

4.6.4. Confirmation of the Robotic Movement while Installing Small Eddy Current Probe

As shown in **Figure 4.45**, the probe is connected to the inspection robot with special probe holder. The probe holder was designed aiming not to be heavy as to affect the movement of the inspection robot. However, during the movement of the inspection robot, it was necessary to pull up the probe holder with only the force of the piston of the air cylinder. The probe holder is floating when the inspection robot is moving, hence, it was conceivable to influence the smooth movement of the inspection robot. Therefore, the movement performance of the inspection robot was confirmed at a corroded metal surface and a concrete wall surface.

Figure 4.46 shows the movement performance on the corroded metal surface and the mortar wall surface. It was confirmed that the robot moves forward and retreat more stable than before installing the φ10 probe. Since the left and right legs of the upper part in the inspection robot are fixed at a constant distance by the probe holder, even if excessive force is applied to the robot the air pad can always move in parallel with target surfaces. Problems were not confirmed even in the probe pulling up operation which was concerned to influence robotic movement. However, during the rotation motion, the robot rotates by expansion and contraction of the piston one by one it kept the air pads parallel to surfaces using aforementioned the bending force of the robot body. It was confirmed that the rotation angle was reduced and the re-attachment after the rotation became unstable due to the constraint of the movement of the upper part of the insertion robot body. This problem was able to solve by starting the movement from the lower part on which a probe holder is not installed at the time of the robot rotation movement. Yet this solution increases wasteful movement. Therefore, another effective installation method of the probe will be investigated in future works.

4.6.5. Application on a Corrosion Specimen using Proposed Robot

The influence of the air pump, the air compressor, a vibration due to the inspection robot on measurement data obtained by the φ10 probe which is installed on the inspection robot needs to be confirmed and eliminate the influences if necessary. Specifically, the results measured using the calibration specimen by the probe installed the inspection robot, named hereafter robot probe, are compared with the data acquired by the φ10 probe in the previous section. Data using the robot probe is acquired by changing the lift-off or thickness to check whether the two data have differences. Since the robot probe is brought into close contact with surfaces by the sponge air pad, it is not assumed that lift-off as a gap occurs. Moreover, since it is also necessary to adjust the installation height of the probe holder, before starting the measurement on target surfaces, it is important to do aforementioned process as a calibration.

The calibration method and the movement performance when the φ10 probe was installed to the inspection robot was examined. In this section, finally the applicability of CDE method

(VP_robot) which is the CDE method (VP) using the robot, was investigated using the corrosion specimen. It was confirmed that the vibration of the robot and the air compressor or the air pump had no influence on the lift-off or the thickness estimation. Since the corrosion specimen is small and it is difficult to attach the robot on the same surface, measurement was carried out by placing the corrosion specimen under the probe holder connected to the inspection robot and attaching the sponge air pads of the probe holder to the corrosion specimen. **Figure 4.47** shows the results of estimating the lift-off and the thickness of corrosion specimen using CDE method (VP_robot) as well as CDE method (VP_φ10). The conditions except installing the φ10 probe to the inspection robot are same as the measurement with the φ10 probe in the previous section. Therefore, for the purpose of comparing the measurement accuracy, the measurement result with the φ10 probe alone is also shown in **Figure 4.47**. In the CDE method (VP_robot), the values which were after applying calibration process was used as the evaluation value. It was confirmed that the evaluation results of each CDE method and the values of Real show good agreement respectively. Since the measurement result shows good agreement, it is considered that no problems with the installing method of the φ10 probe on the inspection robot were confirmed. Therefore, it is able to considered that the CDE method performed by the inspection robot has enough evaluating possibility.

4.7. Summary

In this research, CDE method using low-frequency eddy current that can acquire corrosion damage information such as thickness of rust layer and residual plate thickness more easily without accompanying surface preparation such as removal of corrosion products and coating films are more compact and more convenient was proposed. In order to propose a new method to evaluate the corrosion damage condition by inspection from either the front or back surface of the steel member, a study based on numerical simulation and experiment was conducted. Moreover, the small eddy current probe was installed to the robot to perform the corrosion damage evaluation method as the robotic inspection function. The corrosion damage needs to inspect prone to appear the sections which is narrow or difficult to access by inspectors. Therefore, it can be considered that combination of eddy current without needs of surface preparation and robotic inspection which can approach aforementioned sections are one good option to apply to the CDE method. The conclusions in this research are described below.

- Numerical simulation confirmed the tendency that the detected voltage becomes larger as the plate thickness becomes larger and the detected voltage becomes smaller as the lift off is

larger. The change related to the lift-off is relatively large than change with the thickness. At the high frequency area, a tendency was confirmed that the detected voltage shows a peak at a certain thickness and decreases thereafter despite thickness becomes large. The possibility that the penetration depth is reduced and the electromotive force is lowered due to the eddy current loss have been shown as one of the causes.

Numerical simulation focusing on the phase confirmed the tendency that the phase decreases as the plate thickness decreases and as the lift-off increases. On the other hand, the influence of eddy current loss to the phase confirmed smaller than detected voltage. Therefore, phase was selected as plate thickness estimation index.

- Based on the characteristics obtained in analysis, two CDE methods were proposed. One is CDE method (VV) that uses only detected voltage as an evaluation index and the other is CDE method (VP) that is combines the phase characteristics revealed by numerical simulation and the detected voltage characteristics was proposed. CDE method (VV) uses two different frequencies to obtain thickness of rust layer and residual plate thickness. For estimating rust thickness, high frequency area in this research was used and for residual plate thickness estimation, low frequency was used.

  In the proposed CDE method (VP), the lift-off is estimated by using the detected voltage and the phase is used for the thickness estimation. Therefore, the plate thickness can be estimated by using same sinusoidal wave for estimating lift-off.

  In addition, the influence of lift-off and plate thickness are different so that it is possible to determine whether the damage is the formation of a thinned or rust layer or not and to obtain both information simultaneously.
- By experiments using the calibration specimen for database acquisition, the detected voltage and phase characteristics clarified by the analysis were reproduced, then the lift-off estimation curve and the thickness estimation curve for both methods necessary for actual measurement were obtained. Especially in CDE method (VP) the possibility of estimating the lift-off directly using the original detection voltage without applying the wavelet transform was confirmed.
- Using the steel plate with corrosion damage collected from the actual structure, thickness of rust layer and residual plate thickness were estimated by using both CDE methods. The results indicated that these estimations are actually possible.
- The applicability of CDE method (VP) with the φ10 probe was also confirmed by preparing database and estimating rust thickness and residual thickness of the corrosion specimen. The results indicate the possibility of applying CDE method (VP) to the φ10 probe.

  Moreover, the applicability of CDE method (VP) using φ10 probe as the robotic inspection was successfully performed. The special probe holder which is for installing the φ10 probe to

the inspection robot was made using 3D printer. Performance of the robotic movement after installing the φ10 probe was confirmed at surfaces of corroded metal and concrete.
The applicability of the CDE method (VP_robot) was also confirmed using the corrosion specimen. The results were similar to the CDE method (VP_φ10). It can be considered the CDE method (VP_robot) is able to be one of the robotic inspection function.

All results indicate that the possibility of obtaining the thickness of rust layer and the residual plate thickness with a relatively φ10 probe is demonstrated. Moreover, it became possible to obtain more detailed information than the conventional plate thickness measurement system.
The CDE method (VV) has advantage that can apply to the thicker plate. The CDE method (VP) has advantage that can perform measurement in very short time. Since there are some differences in factors such as eddy current loss or electrical conductivity which influence the detected voltage and phase respectively, and degree of influence, it is expected that each CDE method can be selected according to the characteristics of measurement targets. The CDE method is also able to perform using the inspection robot. Therefore, it can perform at the places where the inspectors cannot reach before. It can be considered that all CDE methods have a possibility to be a versatile inspection method.

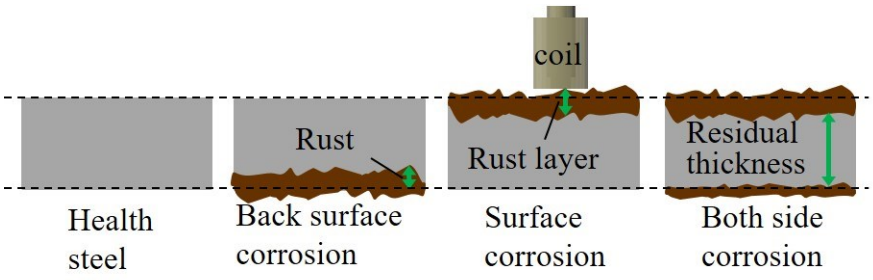

Figure 4.1 Corrosion damage pattern and an inspection method

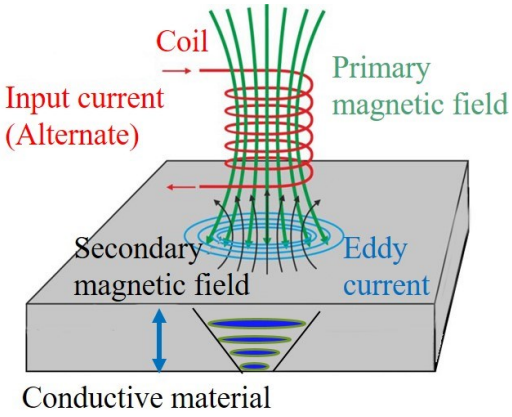

Figure 4.2 Eddy current mechanism

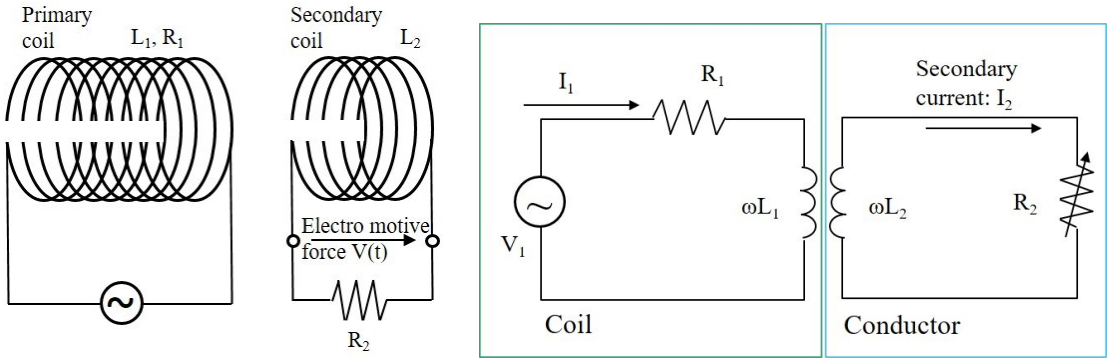

(a) (b)

Figure 4.3 Conceptual image of eddy current testing, (a) Conceptual image, (b) Circuit diagram

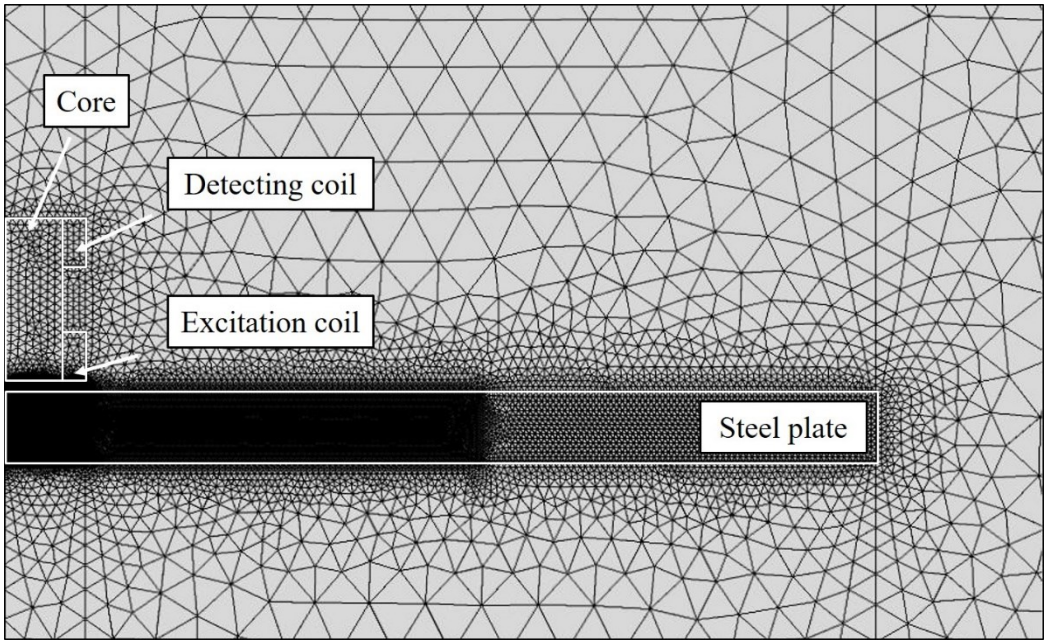

Figure 4.4 Analysis model

Table 4.1 Physical property values of material using in analysis

Material	Relative permeability	Electro conductivity [S/m]
Carbon steel	160	6.0×10^{6}
Air	1	0
Soft iron (without losses)	2000	1

Table 4.2 Specification of coil

Number of turns	400
Diameter [mm]	16.4
Height [mm]	3.7

Table 4.3 Variables used in analysis

Variables	Values using in analysis
Plate thickness [mm]	6, 7, 8, 9
Lift-off [mm]	0, 0.1, 0.2, 0.3
Excitation frequency [Hz]	1, 10, 100, 1000, Sweep wave 1 to 1000

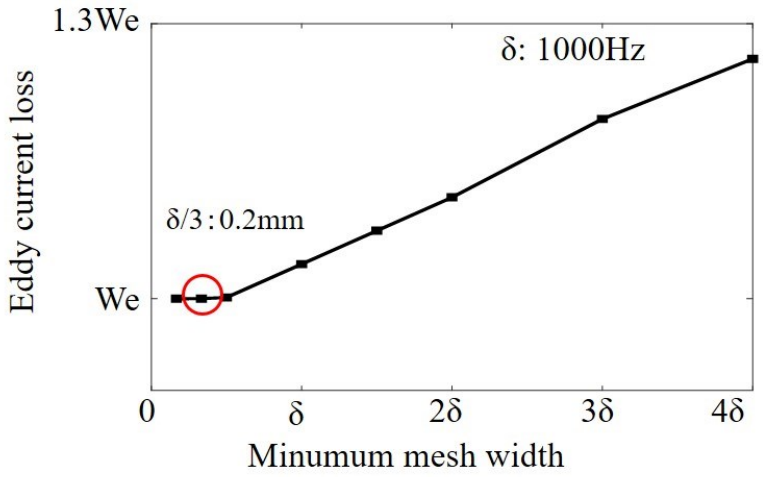

Figure 4.5 Influence of mesh division on eddy current loss

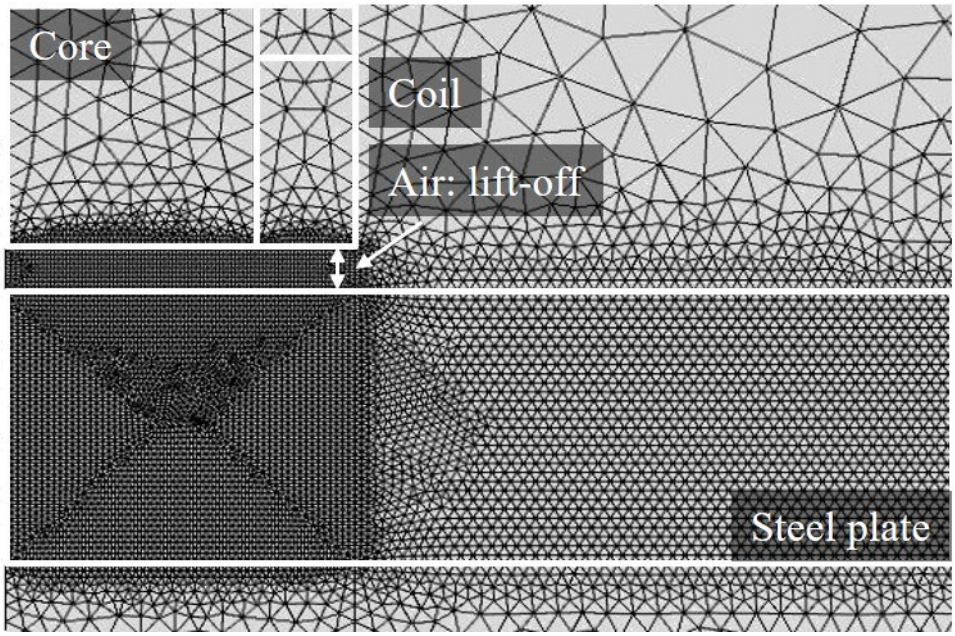

Figure 4.6 Detailed mesh division of analysis model

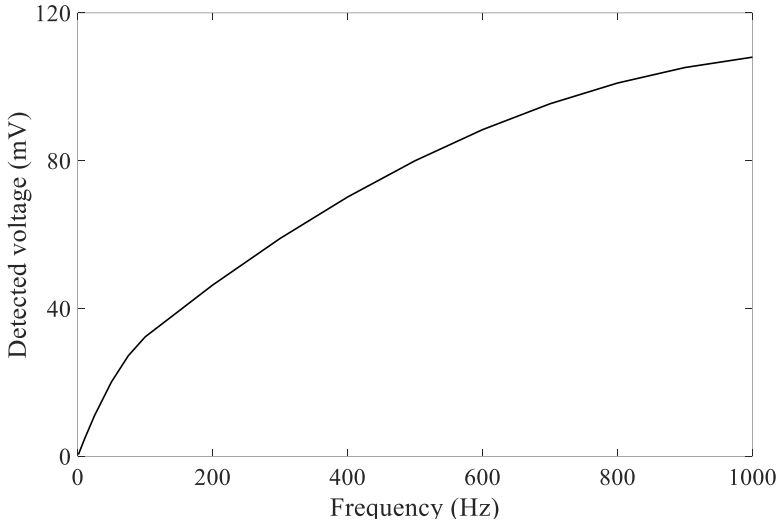

Figure 4.7 Relationship between detected voltage and frequency

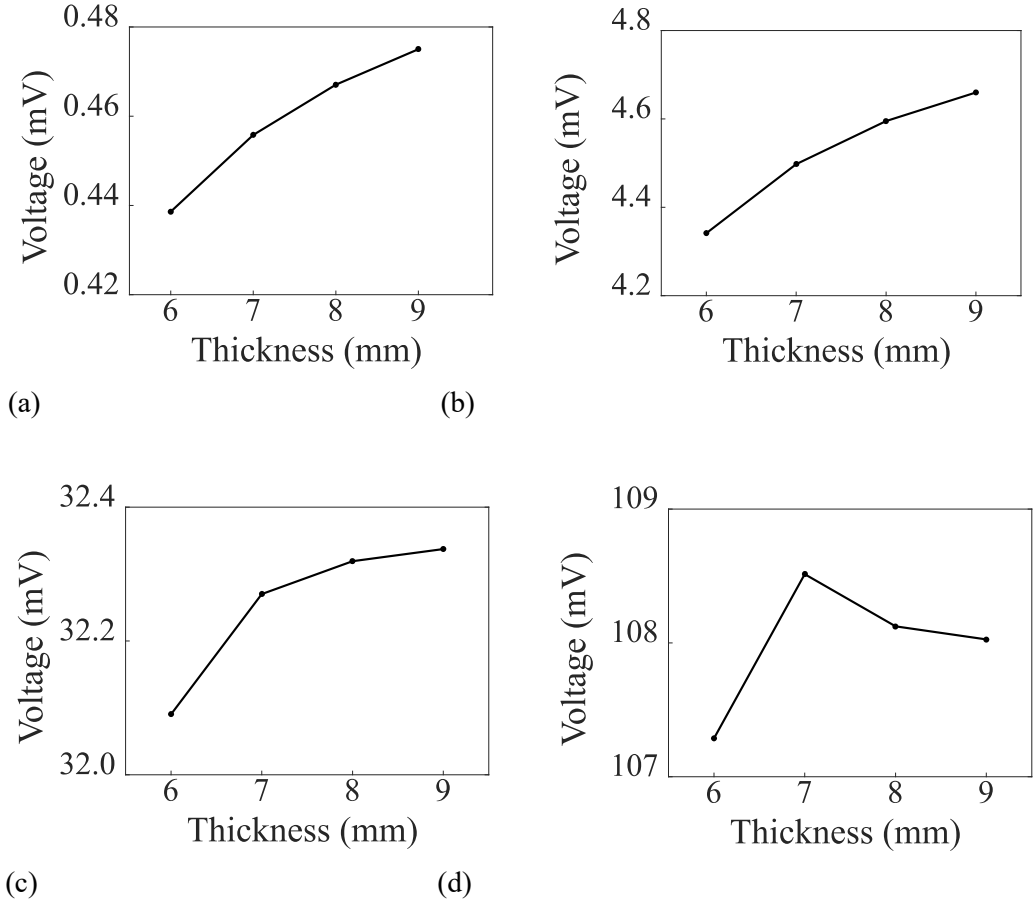

Figure 4.8 Relationship between detected voltage and plate thickness, (a) 1Hz, (b) 10Hz, (c) 100Hz, (d) 1000Hz

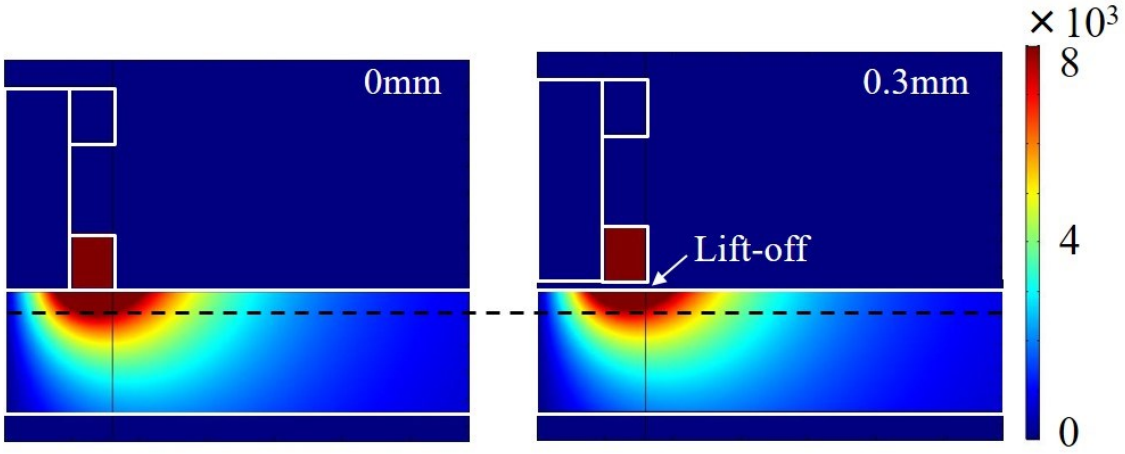

(a)

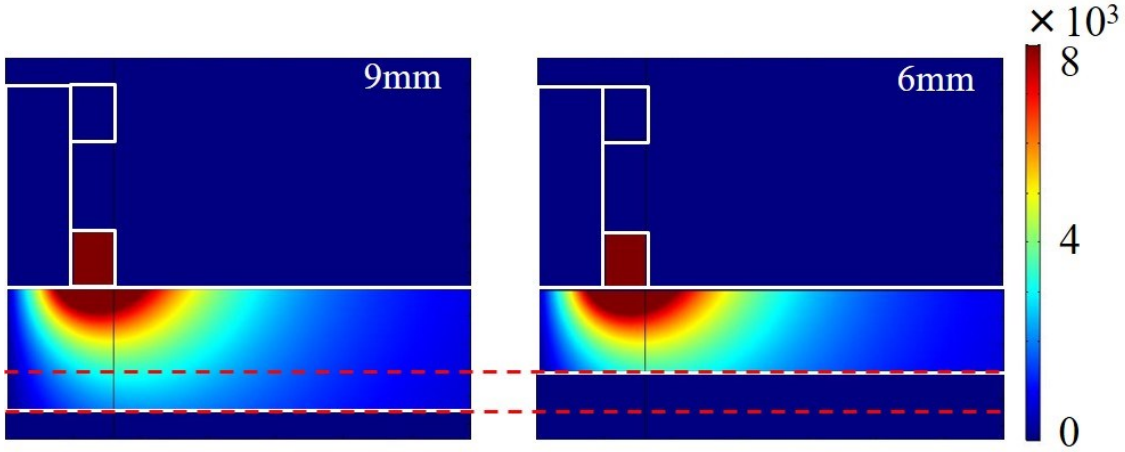

(b)

Figure 4.9 Eddy current density distributions, (a) Plate thickness of 6 mm and 9 mm with 0 mm lift-off, (b) Lift-off of 0 mm and 0.3 mm for 9 mm plate thickness

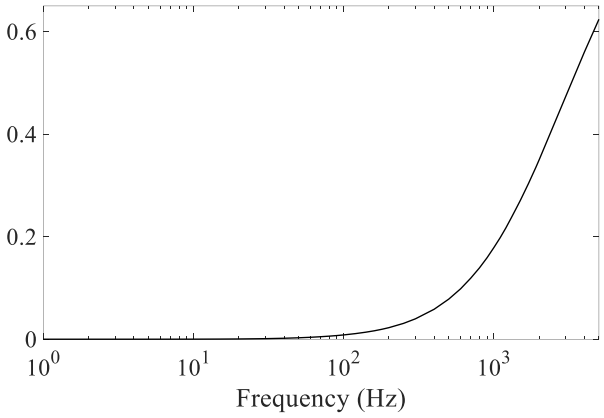

Figure 4.10 Ratio of eddy current loss to total energy consumption

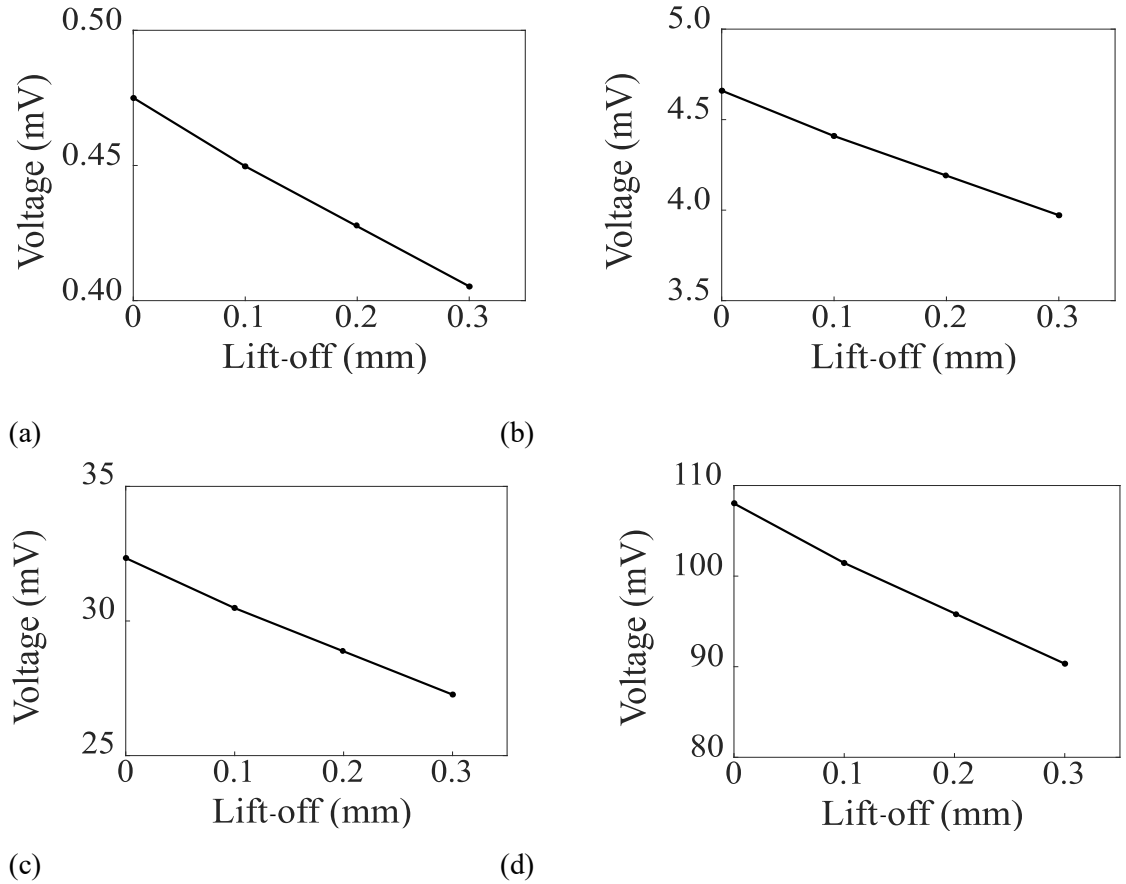

Figure 4.11 Relationship between detected voltage and lift-off, (a) 1Hz, (b) 10Hz, (c) 100Hz, (d) 1000Hz

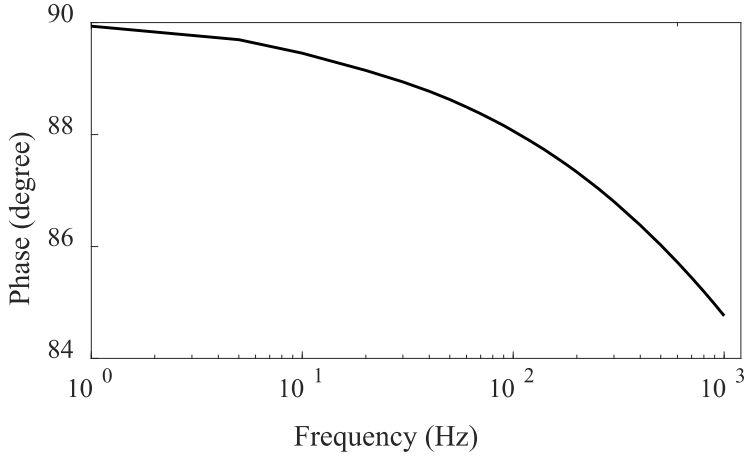

Figure 4.12 Relationship between phase and frequency

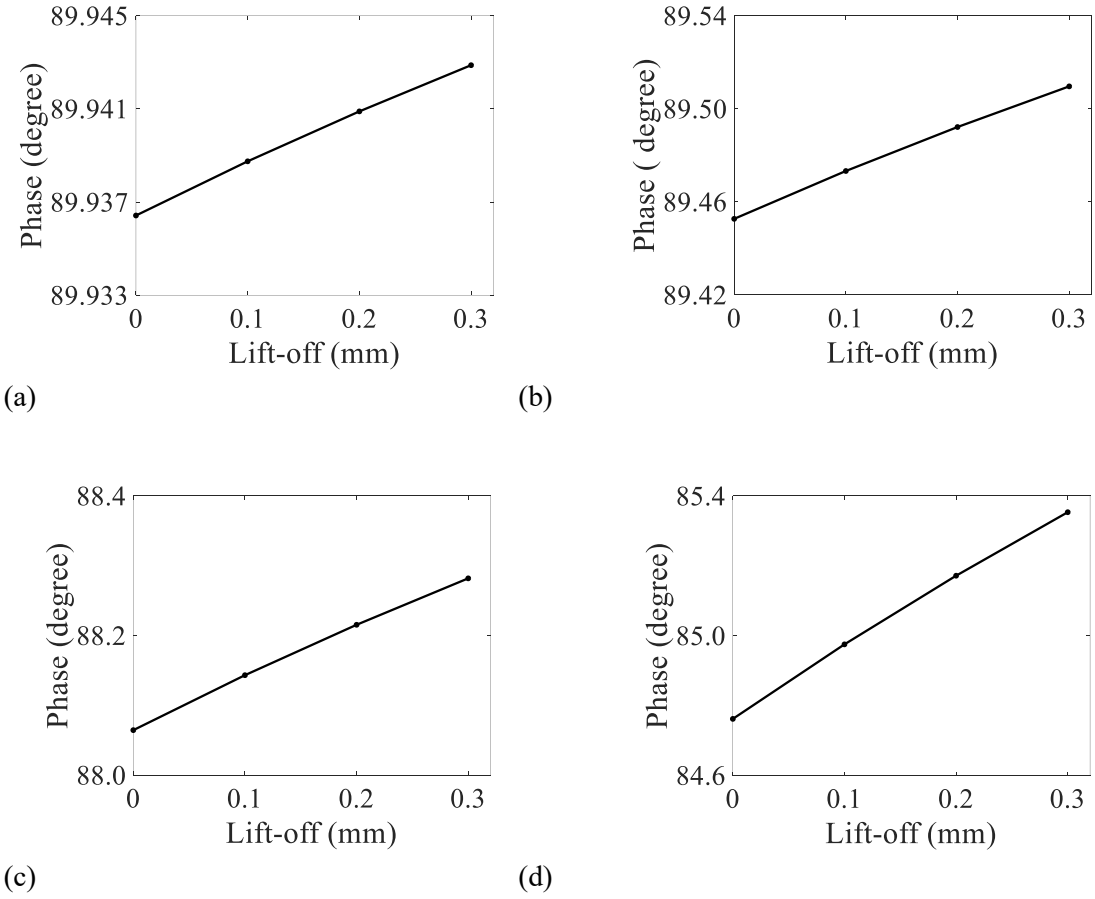

Figure 4.13 Relationship between phase and lift-off, (a) 1Hz, (b) 10Hz, (c) 100Hz, (d) 1000Hz

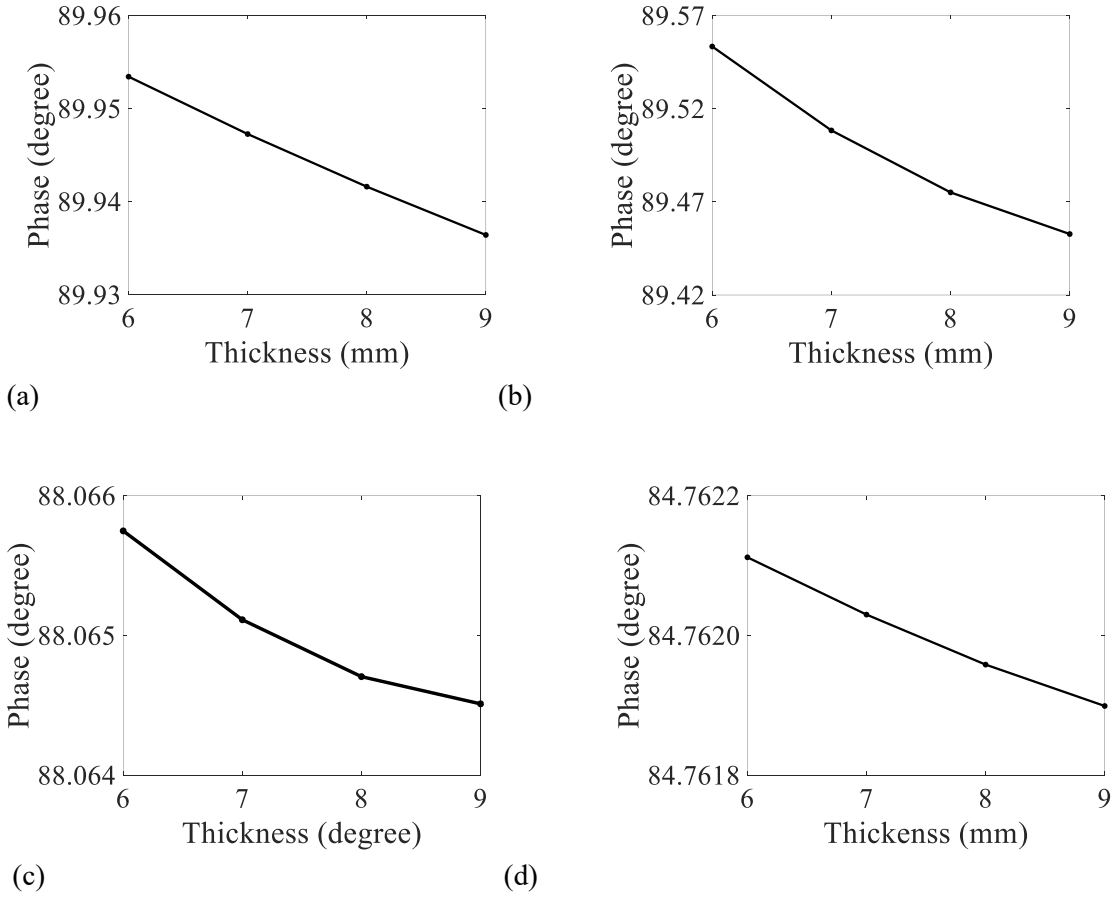

Figure 4.14 Relationship between phase and plate thickness, (a) 1Hz, (b) 10Hz, (c) 100Hz, (d) 1000Hz

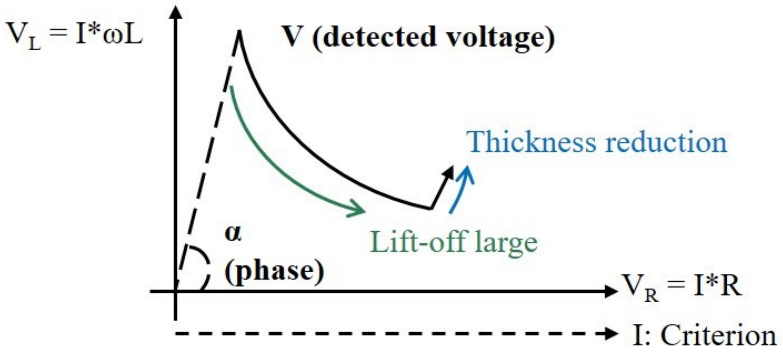

Figure 4.15 Conceptual image of the effect on lift-off and thickness by the detected signal

Table 4.4 Features of proposed CDE methods

	Lift-off	Thickness	Feature
CDE method (VV)	**V**oltage	**V**oltage	Deeper thickness
CDE method (VP)	**V**oltage	**P**hase	Speedy measurement

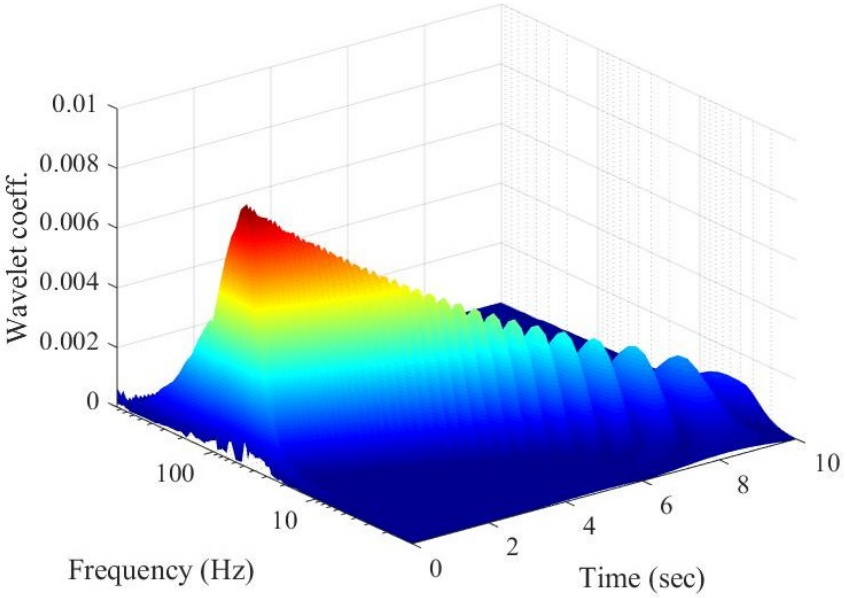

(a)

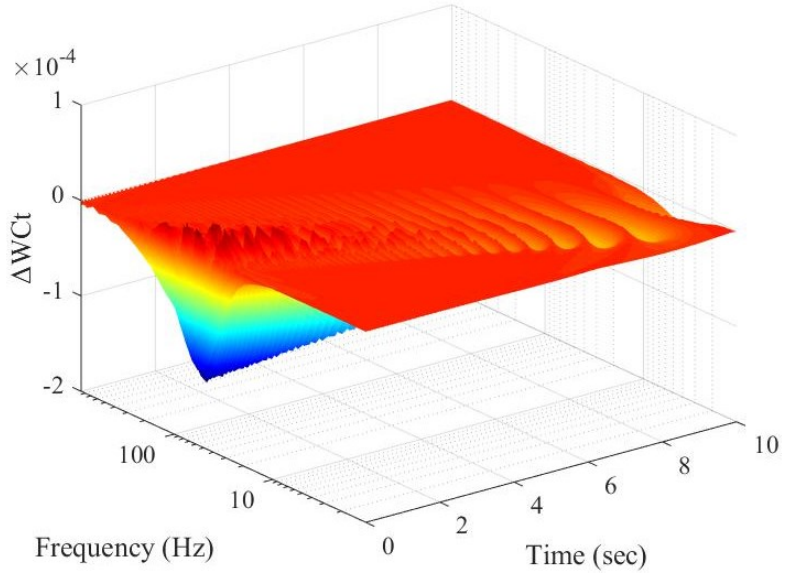

(b)

Figure 4.16 Example results applying wavelet transformation, (a) Plate thickness 9mm and lift-off 0 mm, (b) Plate thickness signal strength

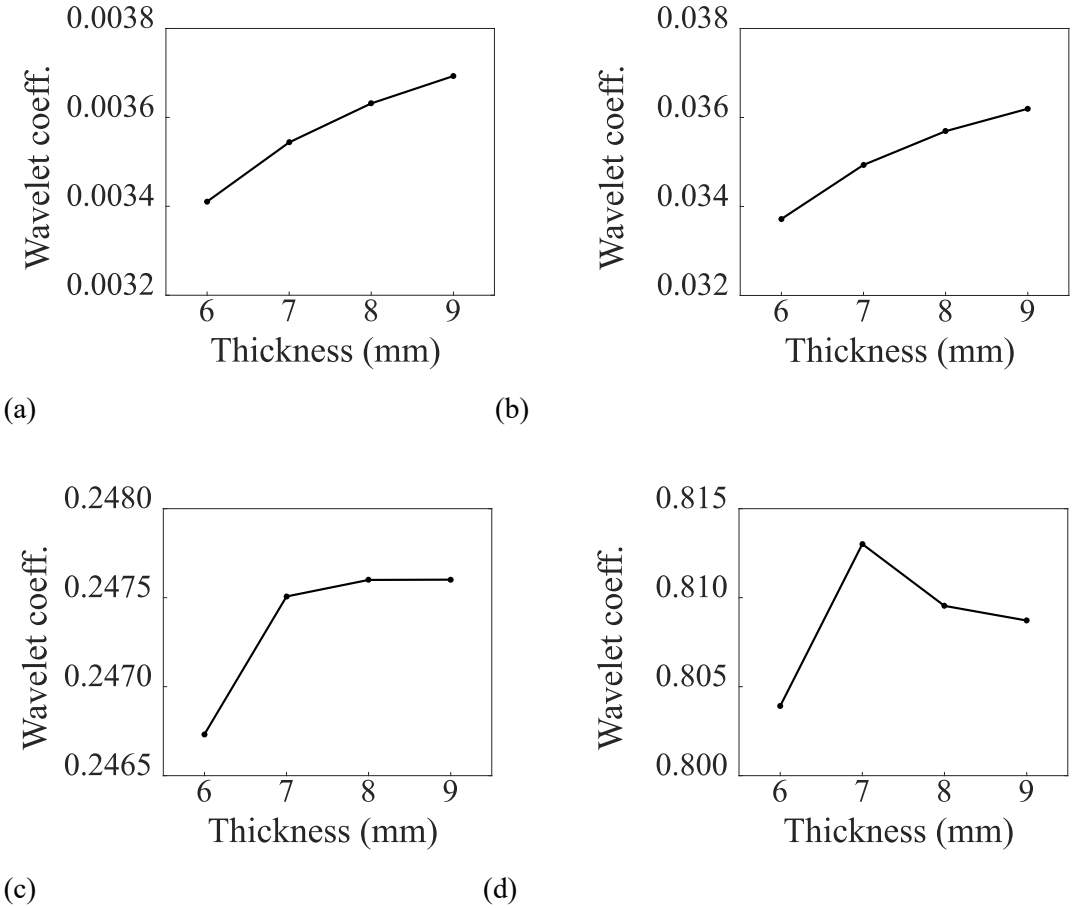

Figure 4.17 Relationship between wavelet coefficient and plate thickness, (a) 1Hz, (b) 10Hz, (c) 100Hz, (d) 1000Hz

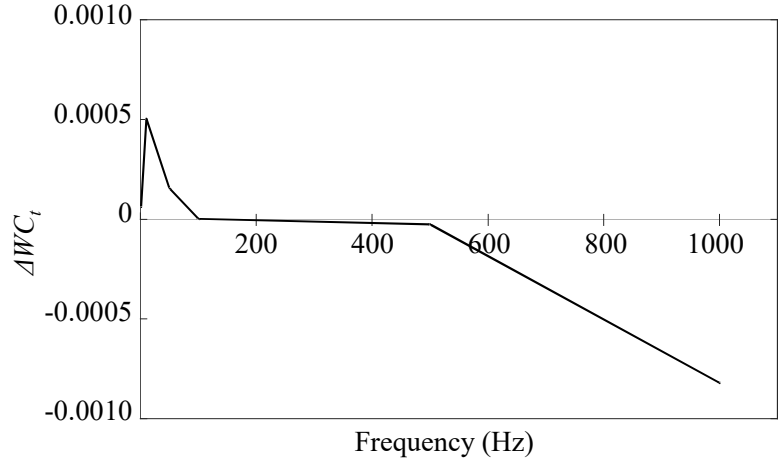

(a)

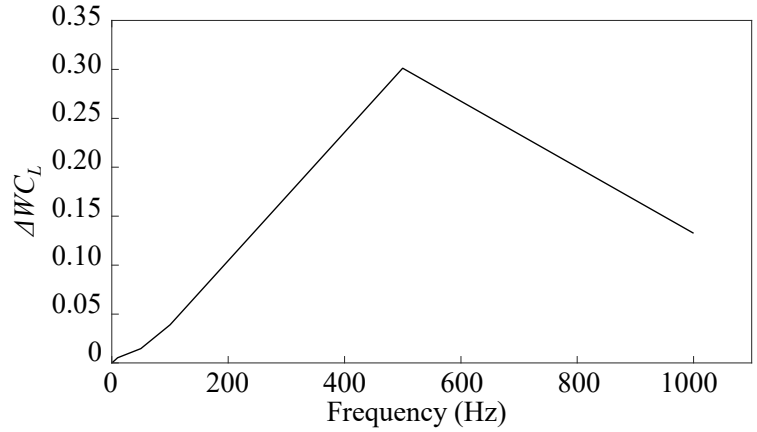

(b)

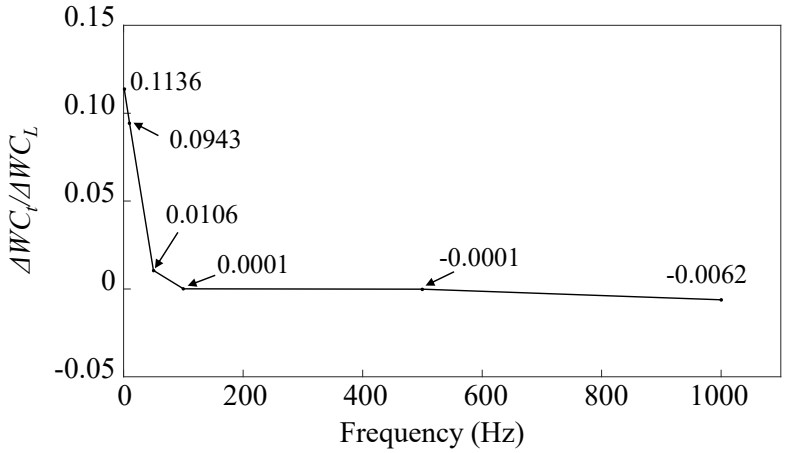

(c)

Figure 4.18 Signal strength, (a) Plate thickness signal strength, (b) Lift-off signal strength, (c) TL signal ratio

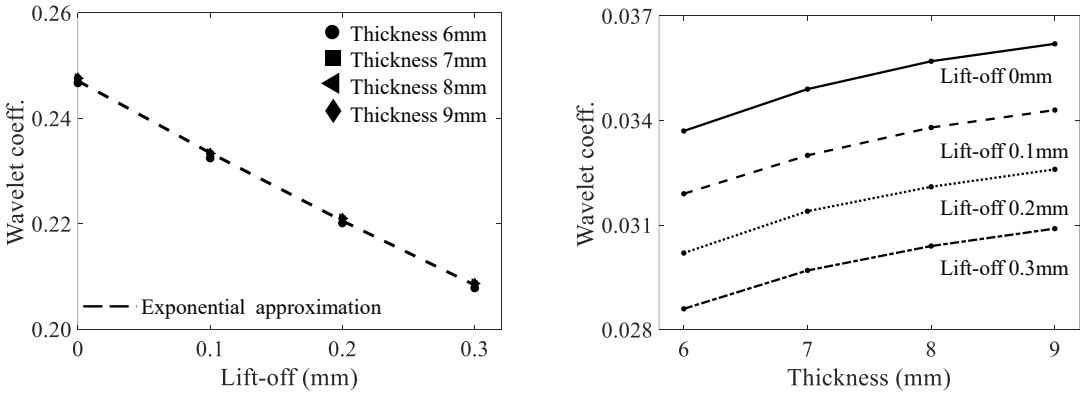

(a) (b)

Figure 4.19 Corrosion damage estimation curve, (a) Lift-off estimation curve (VV), (b) Thickness estimation curve (VV)

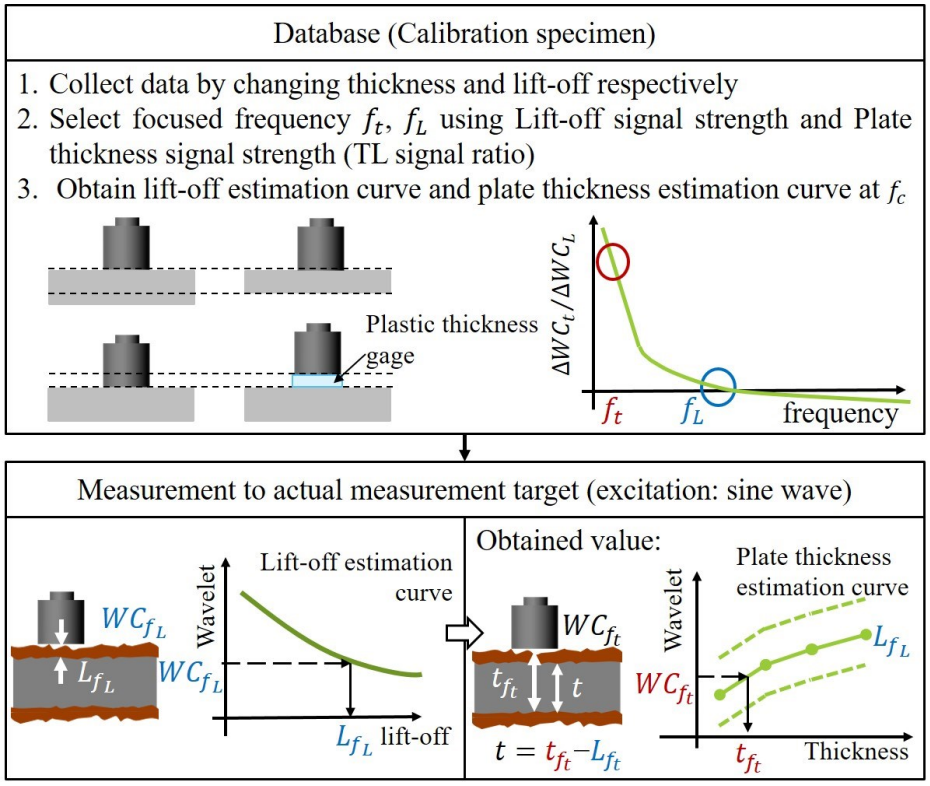

Figure 4.20 Flow of estimating lift-off and plate thickness (VV)

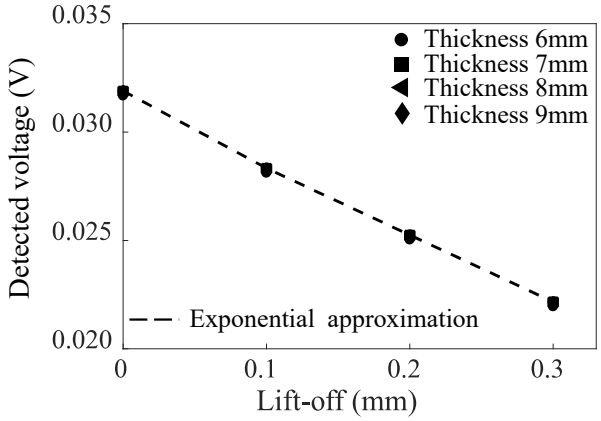

Figure 4.21 Lift-off estimation curve (VP)

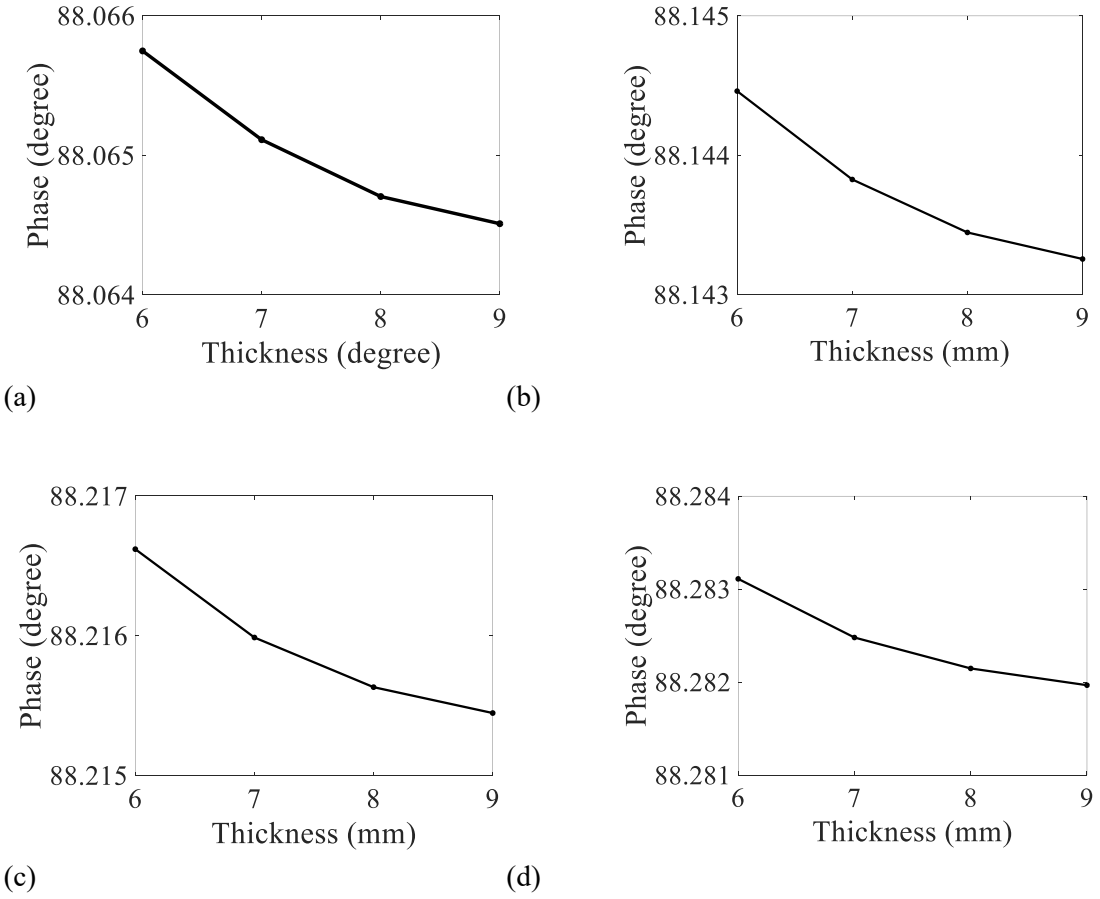

Figure 4.22 Plate thickness estimation curve (VP), (a) Lift-off 0 mm, (b) Lift-off 0.1 mm, (c) Lift-off 0.2 mm, (d) Lift-off 0.3 mm

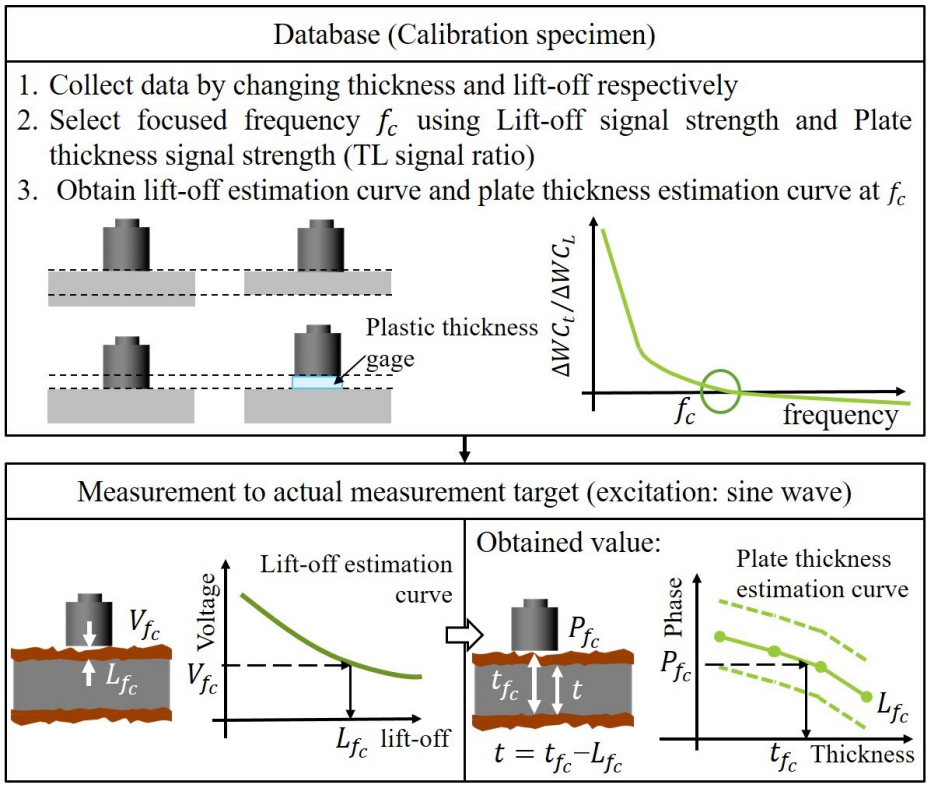

Figure 4.23 Flow of estimating lift-off and plate thickness (VP)

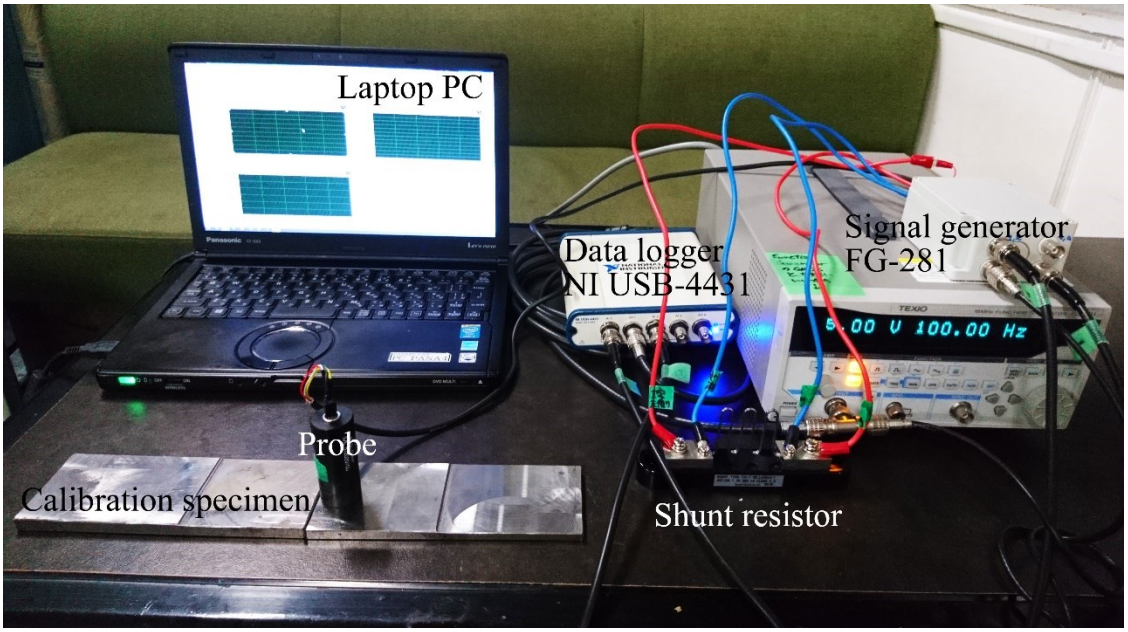

Figure 4.24 Measurement system

Table 4.5 Specification of measurement probe

Probe diameter [mm]	23.7
Probe height [mm]	58.3
Probe weight [g]	50.7

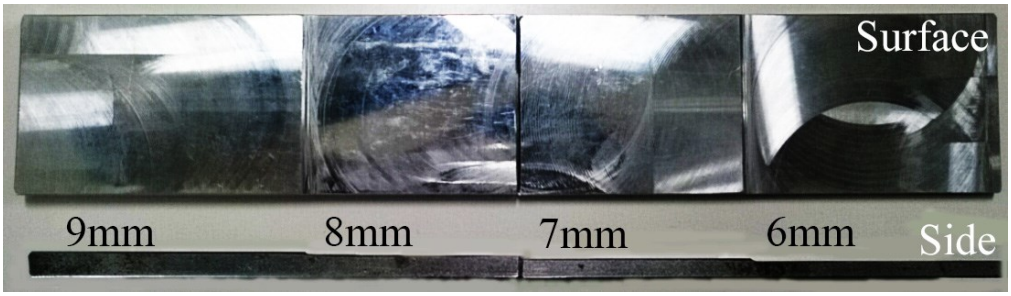

Figure 4.25 Calibration specimen

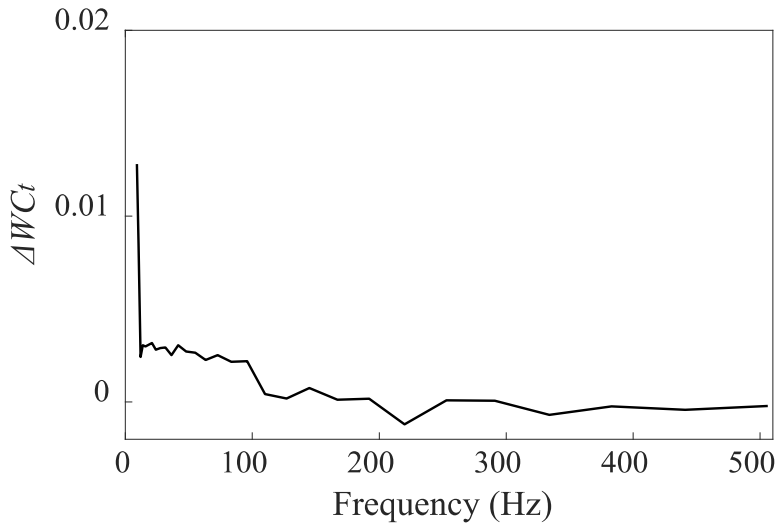

Figure 4.26 Thickness signal strength

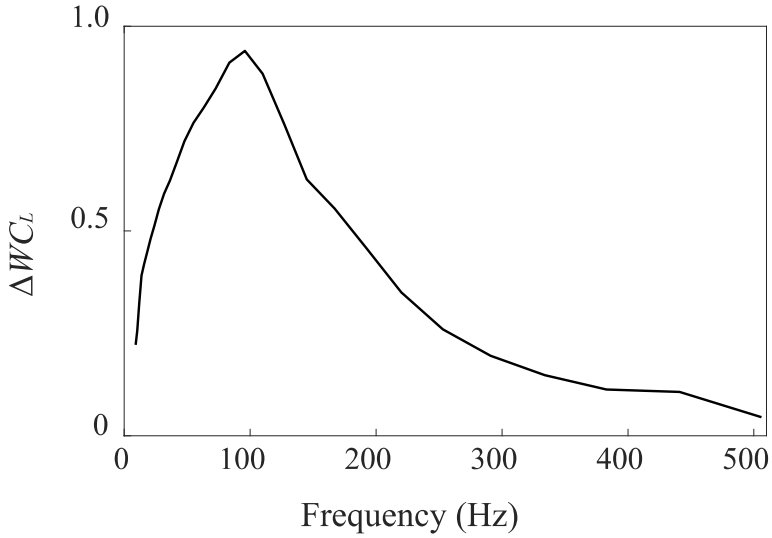

Figure 4.27 Lift-off signal strength

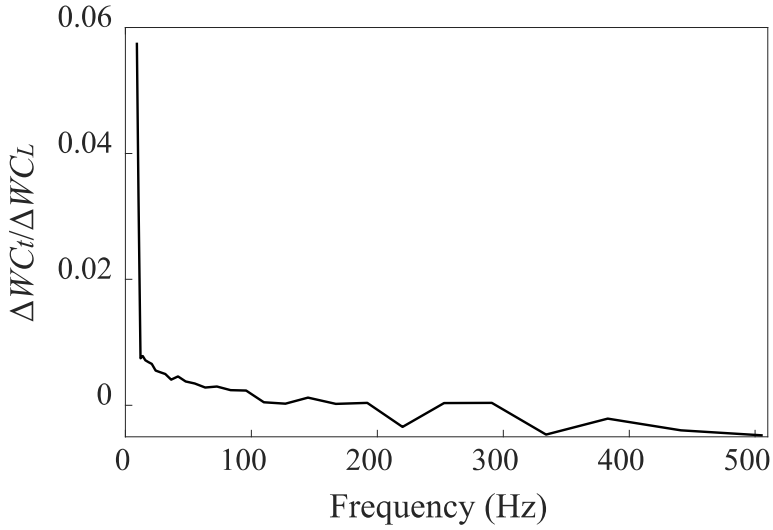

Figure 4.28 TL signal ratio

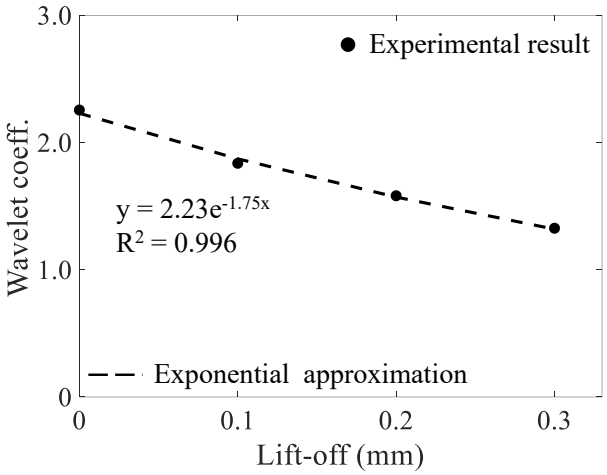

Figure 4.29 Lift-off estimation curve (VV)

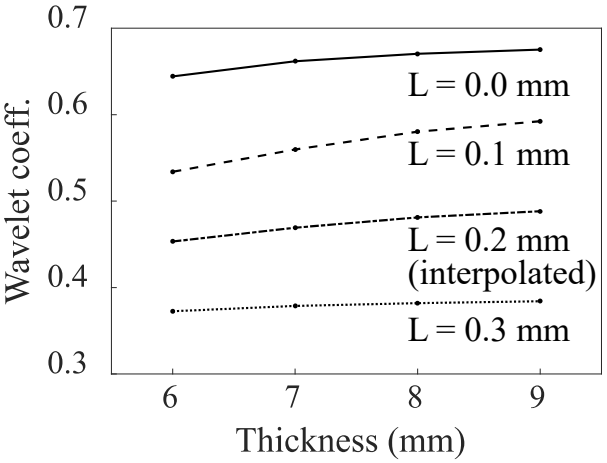

Figure 4.30 Plate thickness estimation curve (VV)

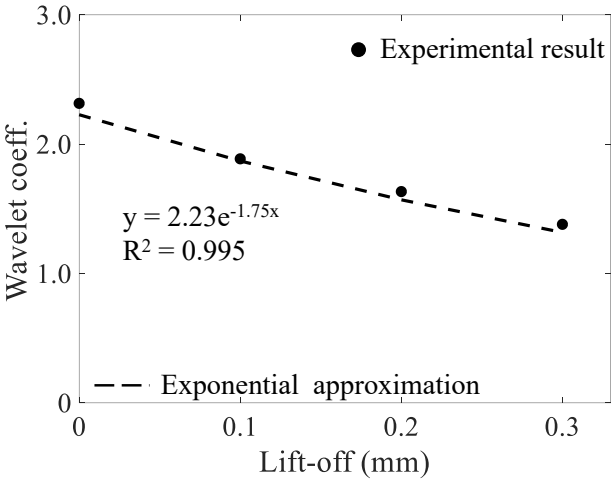

Figure 4.31 Lift-off estimation curve (VV) using thicker steel plate with thickness of 16 mm to 19 mm

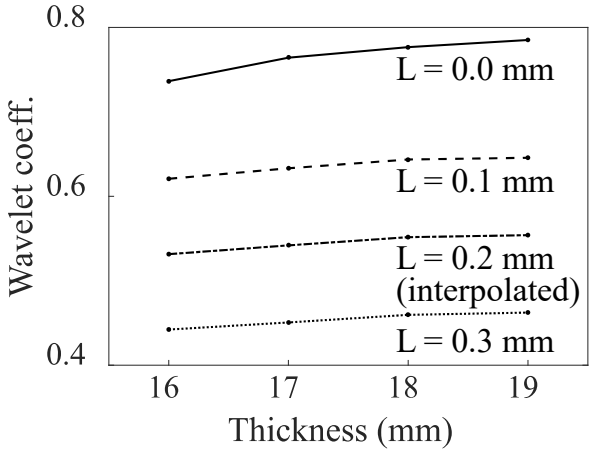

Figure 4.32 Plate thickness estimation curve (VV) using thicker steel plates with thickness of 16 mm to 19 mm

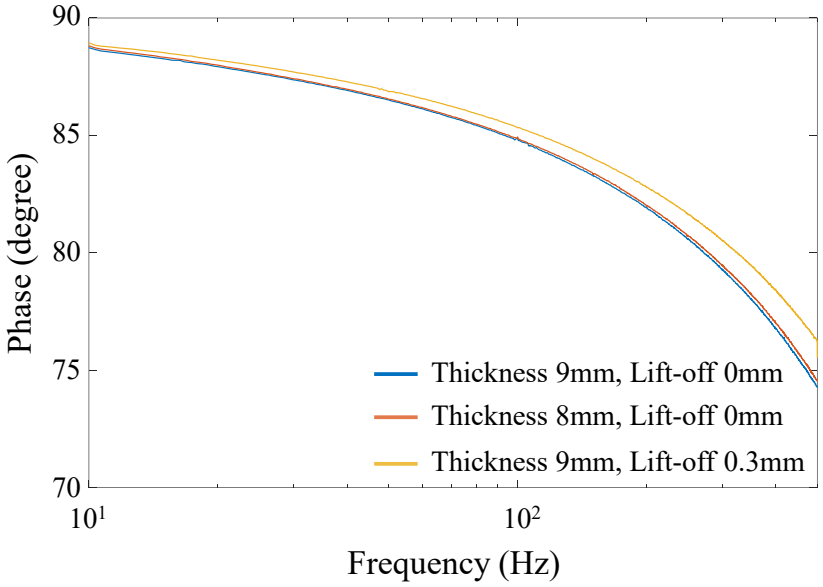

Figure 4.33 Relationship between phase and frequency as experimental example

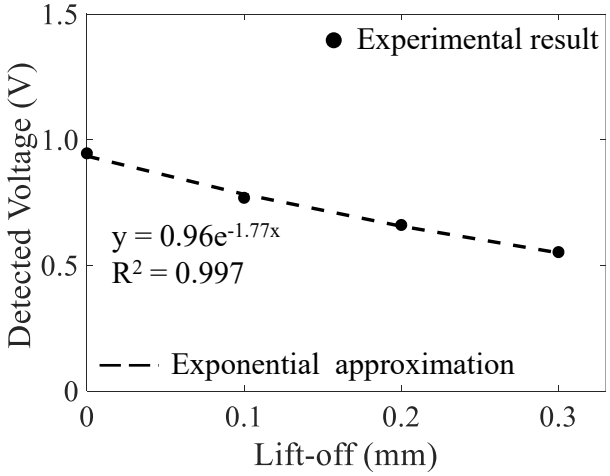

Figure 4.34 Lift-off estimation curve (VP)

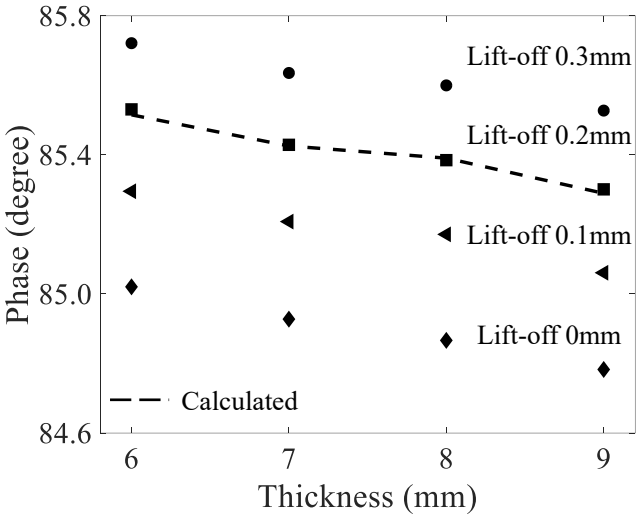

Figure 4.35 Plate thickness estimation curve (VP)

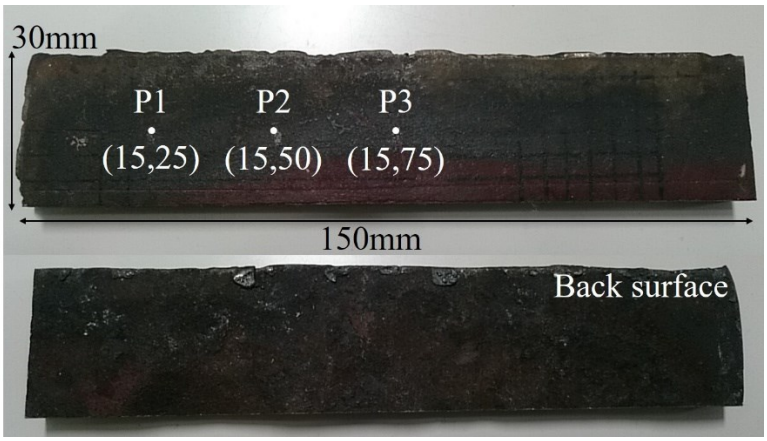

Figure 4.36 Corrosion specimen

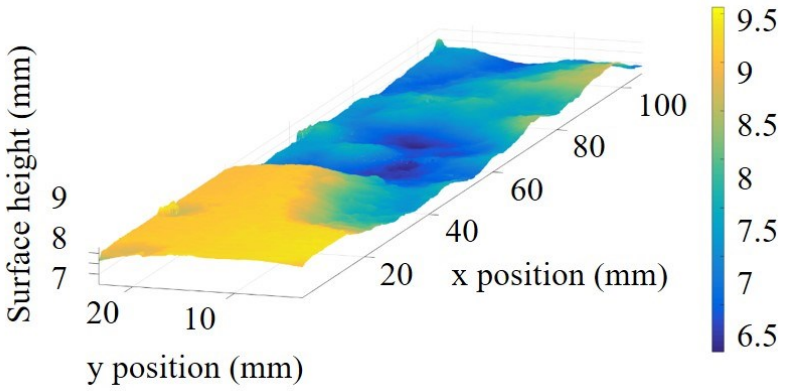

Figure 4.37 Back surface shape of corrosion specimen

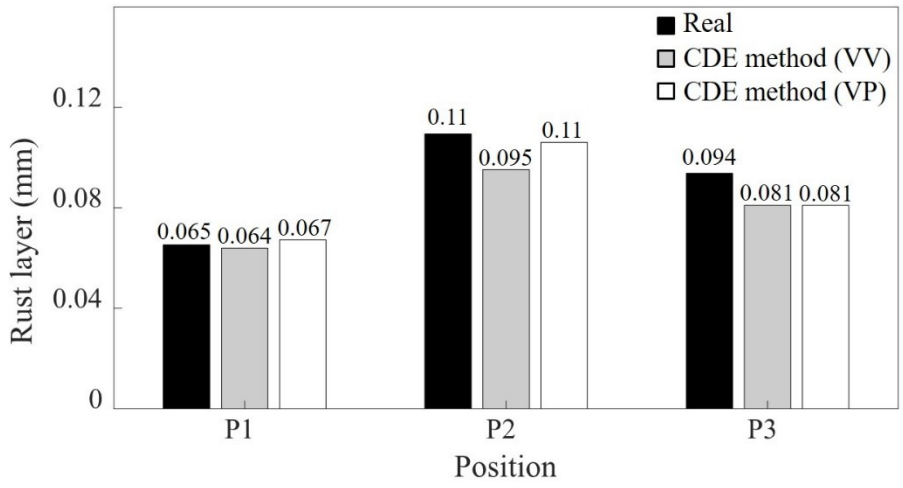

(a)

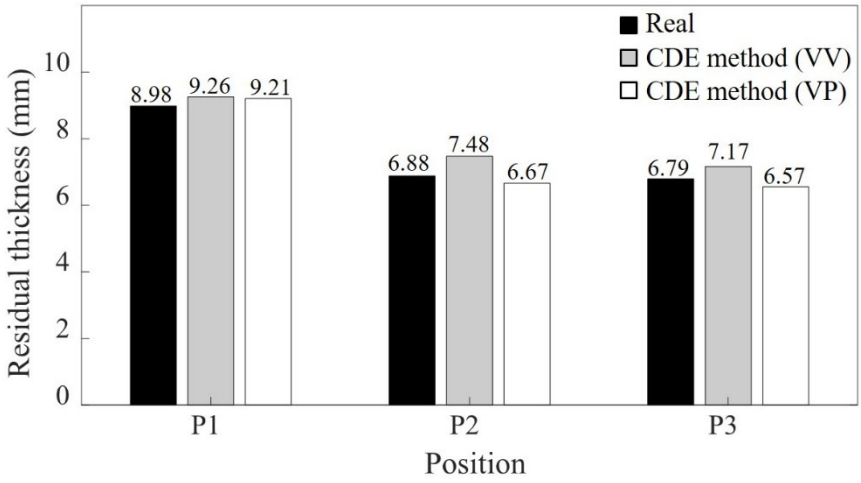

(b)

Figure 4.38 Corrosion damage estimation results, (a) Estimation result of rust layer thickness, (b) Estimation result of residual plate thickness

Table4.6 Specification of small probe

Probe diameter [mm]	10.0
Probe height [mm]	46.5
Probe weight [g]	9.4

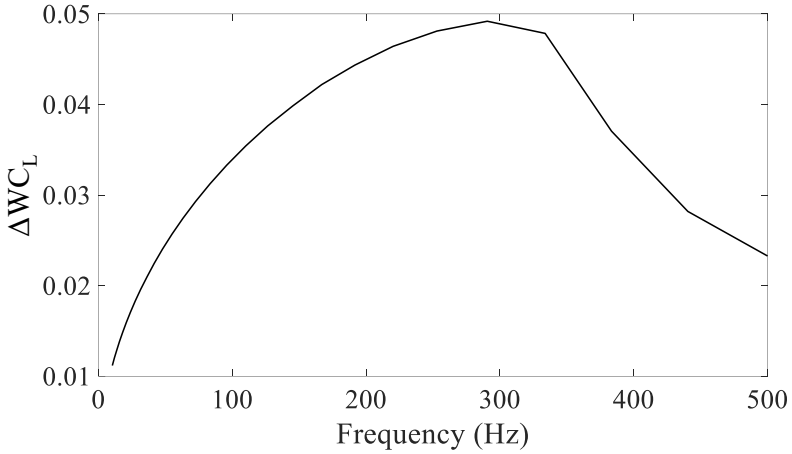

Figure 4.39 Lift-off signal strength (φ10 probe)

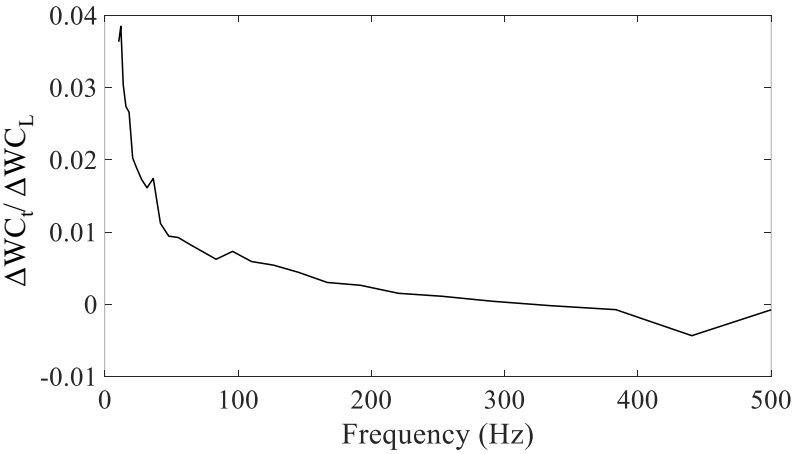

Figure 4.40 TL signal ratio (φ10 probe)

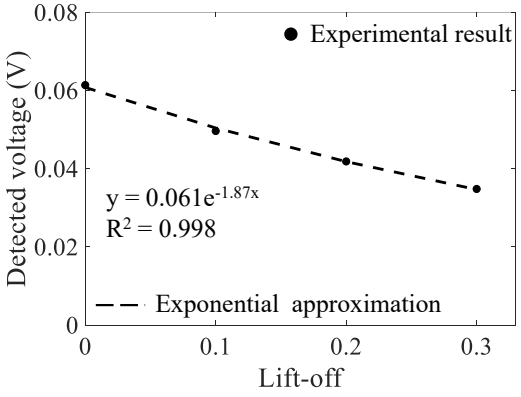

Figure 4.41 Lift-off estimation curve (VP_φ10)

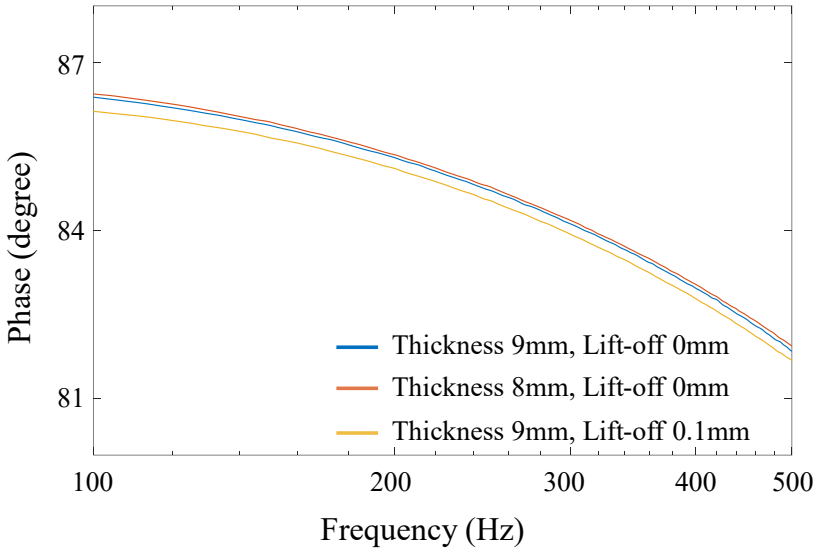

Figure 4.42 Relationship between phase and frequency

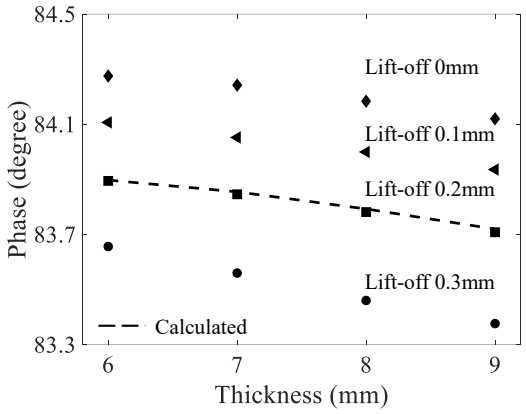

Figure 4.43 Plate thickness estimation curve (VP_φ10)

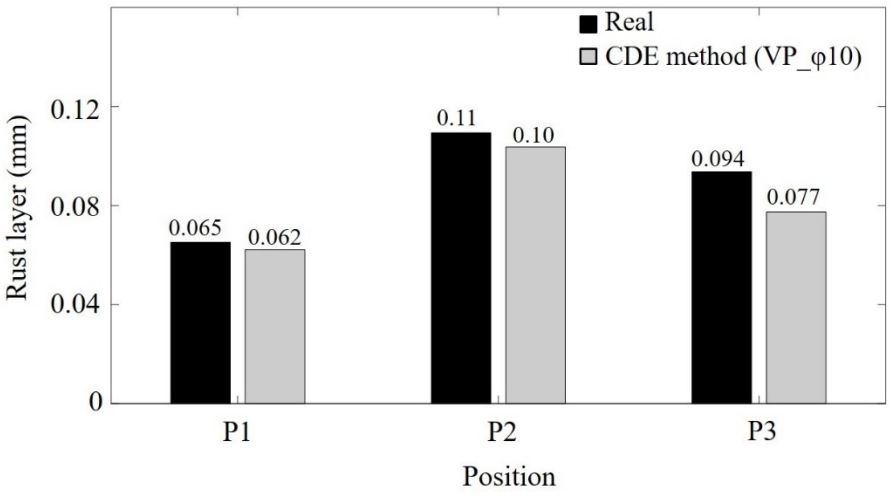

(a)

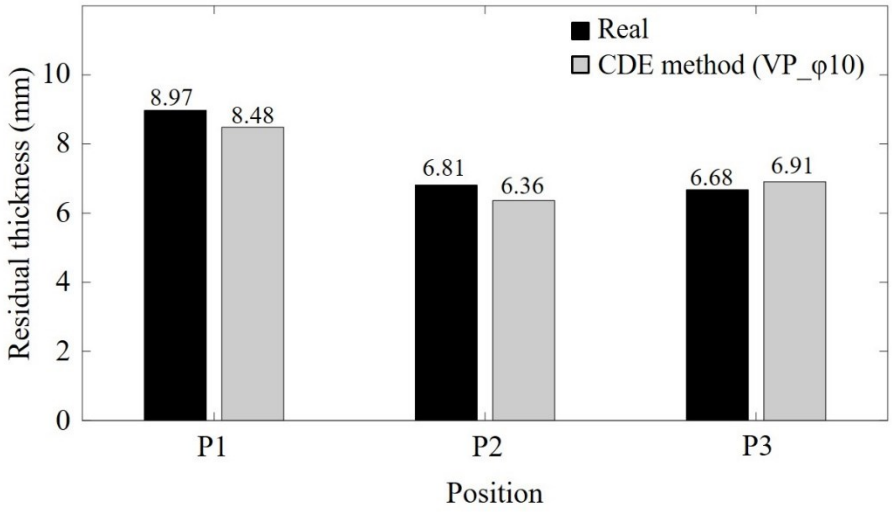

(b)

Figure 4.44 Corrosion damage estimation results (VP_φ10), (a) Estimation result of rust layer thickness, (b) Estimation result of residual thickness

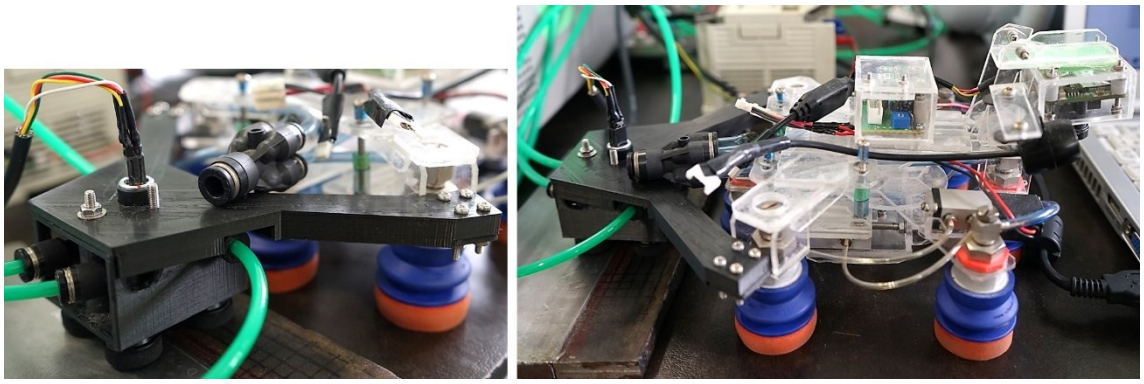

Figure 4.45 Appearance of probe holder and inspection robot with a φ10 probe

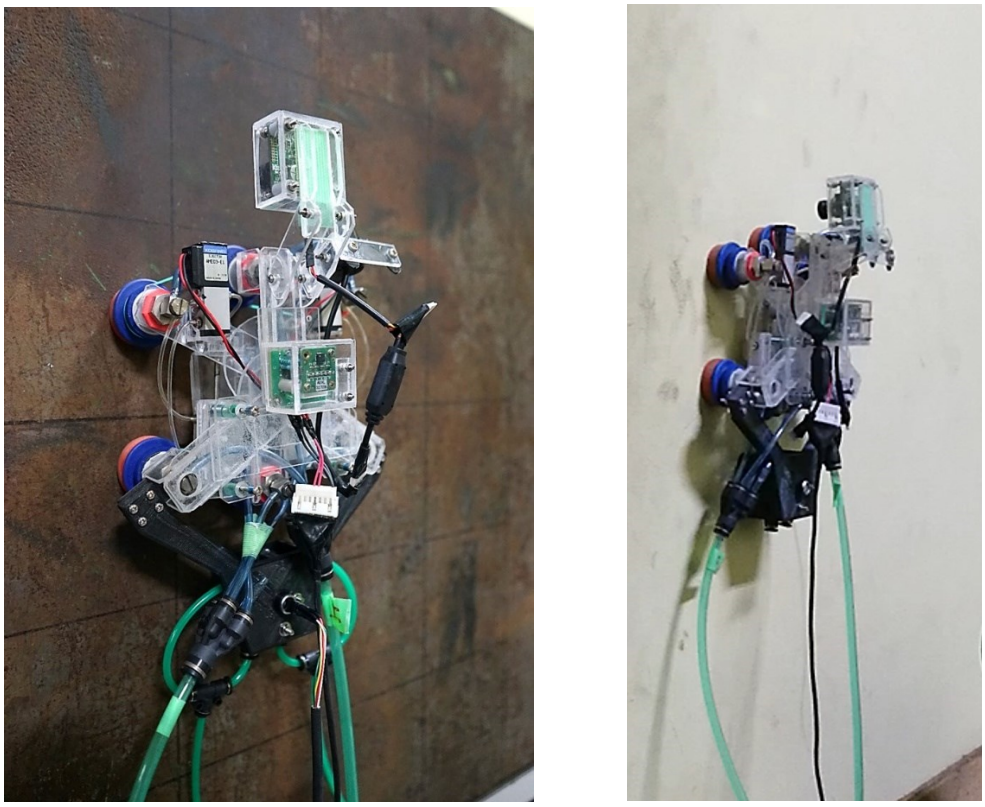

(a) (b)

Figure 4.46 Movement performance on a corroded metal surface and concrete wall surface, (a) Corroded metal surface, (b) Mortar wall surface

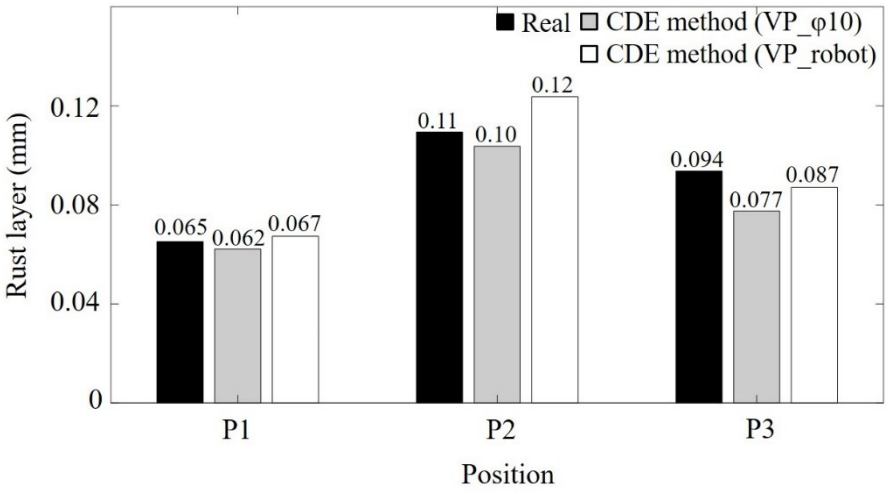

(a)

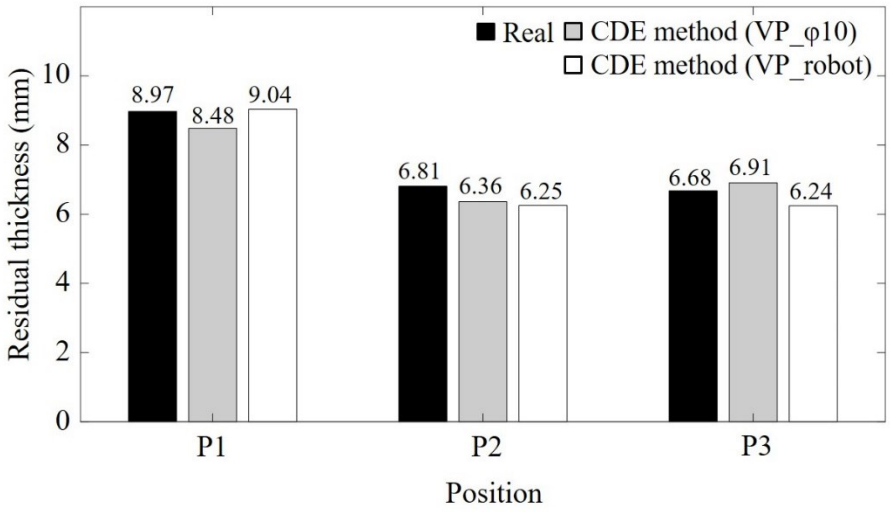

(b)

Figure 4.47 Corrosion damage estimation results (VP_robot), (a) Estimation result of rust layer thickness, (b) Estimation result of residual thickness

Chapter 5

Conclusions and Recommendations

5.1. Conclusions

The results obtained in this research are related to the objectives of this research. Conclusions of this study are described as follows:

- **Development of a mobile robotic inspection device which can move on various surfaces and access locations difficult for inspectors.**

An inspection robot which can move across various surfaces to carry inspection devices for robotic inspection has been developed. The developed inspection robot uses air pads to attach to various types of surfaces includes differences in materials, roughness, and angles and air cylinders to move forward, retreat and rotate. Moreover, to evaluate the suction condition which can evaluate attachment condition of the inspection robot, a gap coefficient, which is the average height between the air pads and surface has been defined. Using this gap coefficient, a quantitative evaluation method for the suction state has been proposed. The most important factor to use air pad is attachment condition, therefore, the suction state helps inspectors to estimate how well the inspection robot will attach to target bridges in advance of carrying out inspection. Further, to improve attachment condition, sponge bellows air pad and silicone sponge bellows air pad were proposed. Finally, performance of robotic movement was examined on target surfaces, at an existing bridge and at the trial bridge.

- **Investigation of robotic inspection functions for observation and various measurements.**

For steel bridges, which consist of steel or concrete sections, it is necessary to inspect damaged parts such as concrete decks with cracks or steel decks or truss components with corrosion. In this study, inspection functions as observation and measurement in concept of robotic inspection is implemented to the inspection robot. In the robotic inspection, robot is assumed to work at blind spot in addition, when inspectors find cracks or corrosion damage the location information of the robot is important. Therefore, the following inspection function are successfully implemented to the inspection robot.

(a) Visual inspection function using attached camera
(b) Location identification function using obtained images by visual inspection camera
(c) Crack detection function for decks
(d) Function to determine structural behavior using attached acceleration sensor
(e) Evaluation of hammering test results (optional function)

The influence of the inspection robot vibration to obtaining bridge behavior was confirmed by laboratory experiment and it can be distinguished from other signals such as noise. Therefore,

it was confirmed to be able to perform vibration measurement of bridges. The current installed equipment is two cameras and acceleration sensor. It can be considered that to perform another inspection using small sensors, it is able to replace or add sensors considering the needs of target bridges. As a result, it is conceivable that versatile inspection system has been proposed.

- **Proposal of an efficient corrosion damage evaluation method.**
  An independent inspection method (General inspection)
  One of the robotic inspection functions (Robotic inspection)

To acquire corrosion damage information such as a thickness of rust layer and a residual plate thickness, corrosion damage evaluation method based on eddy current was investigated and proposed. Focusing on the characteristics of detected signal, two evaluation methods were proposed. One is using only detected voltage for estimating the thickness of rust layer and the residual plate thickness by exciting two different frequency sine waves (CDE method (VV)). This method is very suitable even for thicker plates. The other method is using both detected voltage and phase between input current and detected voltage (CDE method (VP)). It needs only one wave to excite. Therefore, this method has an advantage for short time measurement. Applicability of these methods were confirmed using corrosion specimen which was collected from actual bridge. Moreover, installing the φ10 probe to the inspection robot, CDE method (VP) can be one of the robotic inspection function. Applicability after installing the φ10 probe to the inspection robot was also confirmed using corrosion specimen.

All methods have enough accuracy for the measurement in the regular or detailed inspection process. As a robotic inspection function, it can perform at the places where the inspectors cannot reach before. Eddy current can acquire rust layer or coating film therefore, surface preparation is needless. Therefore, the concept of the robotic inspection which access target sections by the inspection robot and perform simple and effective inspection can be achieved. It can be considered that all CDE methods have a possibility to be a versatile inspection method.

Finally, a method to perform simple and effective inspection has been successfully achieved using the proposed robotic inspection and corrosion damage evolution method. A robotic inspection system using proposed inspection robot and corrosion damage evolution method for steel bridges have been proposed and applicability for the actual bridge inspection has been examined. The proposed inspection robot can be applied various types of surfaces and surface conditions. Moreover, proposed corrosion damage evaluation method has become an independent inspection method and one of the robotic inspection function. However, it is difficult to cross over high steps for the inspection robot because there is no mechanism to move the robot legs up and

down or change the angle. The applicability of robotic inspection could be further improved if the sections where the inspection robot is able to access can be extended. In addition, the applicability of corrosion damage evaluation method could be further improved if the coil shape can be optimized because for example shape of the coil can exclude the influence of lift-off noise.

5.2. Recommendations

From the conclusions of this study, the followings are proposed as versatility enhancements of the robotic inspection and corrosion damage evaluation method.

1. If the inspection robot can cross over high steps such as parts of welded joints or concrete joints, the performance area of the inspection robot can be extended. To achieve this with condition of using vacuumed state and air pad, the leg parts of the inspection robot need to be flexible and controlled by electrical devices such as motor.
2. If the inspection robot has more inspection devices to obtain different information such as inclination of surfaces, temperature and humidity of inspection area, or temperature of surfaces, the inspection robot can apply to more versatile inspection. Installing other devices such as a hammer for hammering test, a tilt sensor, a gyro sensor, a thermography camera or replacing devices from current devices, it is considered to actualize aforementioned inspection.
3. Considering performing corrosion damage evaluation using the inspection robot, management of controlling lift-off is difficult. When the method performed by inspector's hand, the lift-off is also influenced to the measurement results. If the lift-off noise can be reduced by optimizing the coil, accuracy and applicability of the method is able to increase.

References

[1] Frangopol, D. M., & Kim, S.: Service life, reliability and maintenance of civil structures, in Lee, L., S., and Karbhari, V. (Eds.), *Service life estimation and extension of civil engineering structures*, Cambridge: Woodhead Publishing, Chapter 5, pp. 145-178, 2011.

[2] Tamakoshi, T., and Nakasu, K.: Current status of bridge management in Japan, The 20th US-Japan bridge engineering workshop, University of Nevada Reno Federal Highway Administration, pp. 159-168, 2004. 10.

[3] Fujino, Y.: Steel Bridges in Japan - Current Circumstances and Future Tasks -, *STEEL CONSTRUCTION TODAY & TOMORROW*, No. 15, pp. 1-3, 2006.

[4] Road Bureau of Ministry of Land, Infrastructure, Transport and Tourism, Japan, The National Highway and Risk Management Division.: 道路橋点検要領 (PDF), Retrieved from http://www.mlit.go.jp/road/ir/ir-council/pdf/yobo3_1_6.pdf. (accessed 21st January 2015), 2014.

[5] Nakashima, M., & Nagai, K.: An Investigation of Road Maintenance System in Japan in Developed Society, *Society for Social Management Systems Internet Journal*, Issue. 9, Vol.1, No. SMS13-2192, 2013. 12.

[6] Road Bureau of Ministry of Land, Infrastructure, Transport and Tourism, Japan, The Road Committee of the Panel on Infrastructure Development.: Recommendations for full-scale maintenance of aging roads (PDF), Retrieved from http://www.mlit.go.jp/road/road_e/03key_challenges/1-2-2.pdf. (accessed 10th March 2015), 2014.

[7] Road Bureau of Ministry of Land, Infrastructure, Transport and Tourism, Japan.: The maintenance of national road network in Japan (PDF), Retrieved from http://www.mlit.go.jp/road/road_e/03key_challenges/1-2-2.pdf. (accessed 11th March 2015), 2011.

[8] Sumitri, S., Tominaga, M., and Kato, Y.: Monitoring Based Maintenance for Long Span Bridges, *Proceeding of First International Conference on Bridge Maintenance Safety and Management IBMAS 2002*, Barcelona, Spain, pp. 1-8, 2002. 7.

[9] Ishida, M., and Usami, O.: Non Destructive Inspection Technology of the Bridge, *Journal of the Japan Society for Precision Engineering*, Vol. 80, No. 11, pp. 975-979, 2014.

[10] Furuta, H., Kayno, M., and Watanabe, E.: Current Status and Future Issues on Bridge Maintenance and Bridge Management System, *Journal of Japan Society of Civil Engineers F*, Vol. 63, No. 3, pp. 287-294, 2007.

[11] Sheils, E., O'Connor, A., Breysse, D., Schoefs, F., and Yotte, S.: Development of a two stage inspection process for the assessment of deteriorating infrastructure, *Reliability Engineering and System Safety*, Vol. 95, pp. 182-194, 2010.

[12] Okasha, N. M., and Frangopol, D. M.: Lifetime-oriented multi-objective optimization of structural maintenance considering system reliability, redundancy and life-cycle cost using GA, *Structural Safety*, Vol. 31, pp. 460-474, 2009.

[13] Hinow, M., and Mevissen, M.: Substation Maintenance Strategy Adaptation for Life-Cycle Cost Reduction Using Genetic Algorithm, *IEEE Transactions on Power Delivery*, Vol. 26, No. 1, pp. 197-204, 2011.

[14] Zhang, D., Ye, F., and Yuan, J.: Life-cycle cost analysis (LCCA) on steel bridge pavement structural composition, *Social and Behavioral Science*, Vol. 96, pp. 785-789, 2013.

[15] So, K. K. L., Cheung, M. M. S., and Zhang, E. X. Q.: Life-Cycle Management Strategy on Steel Girders in Bridges, *Journal of Advances in Civil Engineering*, Vol. 2012, pp. 1-14, 2012.

[16] Kage, I., Matsui, K., and Kawabata, F.: Minimum Maintenance Steel Plates and Their Application Technologies for Bridge - Life-Cycle Cost Reduction Technologies with Environmental Safeguards for Preserving Social Infrastructure Assets -, *JFE TECHNICAL REPORT*, No. 5, pp. 37-44, 2005.

[17] Gattuli, V., and Chiaramonte, L.: Condition Assessment by Visual Inspection for Bridge Management System, *Computer-Aided Civil and Infrastructure Engineering*, Vol. 20, pp. 95-107, 2005.

[18] 社団法人土木学会，鋼橋における劣化現象と損傷の評価，鋼構造シリーズ７，1997.

[19] Aso, T., Goto, S., Tabata, H., and Miyamoto, A.: Study on Corrosion Factors of Weathering Steel Bridges Based on On-Site Observations, *Journal of Japan Society of Civil Engineering F*, Vol. 63, No. 4, pp. 460-468, 2007.

[20] Otake, Y., Sasuga, T., Kobayashi, K., and Honjyo, Y.: An Evaluating Bridge Health Index of Steel Bridge RC Deck Considering Deterioration Mechanisms Based on Statistical Analysis of Bridge Inspection Data, *Journal of Japan Society of Civil Engineering A1*, Vol. 68, No. 3, pp. 683-695, 2012.

[21] Yamaguchi, E.: Application Potential of Weathering Steel Bridges, *STEEL CONSTRUCTION TODAY & TOMORROW*, No. 15, pp. 11-12, 2006.

[22] Tamakoshi, T., Yokoi Y., Okada, S., Mizuguchi, T., and Kowase, Y.: Study on Evaluation of Rust by Appearinca Properties for Weathering Steel Bridge, *TECHNICAL NOTE of National Institute for Land and Infrastructure Management*, No. 828, 2015.

[23] Imai, A., Yamamoto, T., and Aso, T.: A Study of Partial Repair Painting for Weathering Steel Bridge, *Journal of Japan Society of Civil Engineering A1*, Vol. 68, No. 2, pp. 347-355, 2012.

[24] Natori, T., Nishikawa, K., Murakoshi, J., and Ohno, T.: Study on Characteristics of Corrosion Damages in Steel Bridge Members, *Journal of Japan Society of Civil Engineering*, No. 688 / I-54, pp. 299-311, 2001.

[25] Yuan, S., and Chen, W.: Maintenance and Reinforcement Design of Relics Steel Arch Bridge, *Proceeding of the 5th International Conference on Civil Engineering and Trans potation (ICCET 2015)*, Guangzhou, China, pp. 105-111, 2015. 11.

[26] Hosoi, A., Itoh, Y., Kaneko, K., and Sugiura, Y.: Life-Cycle Management Strategy on Steel Girders in Bridges, *Journal of Structure Engineering*, Vol. 57A, pp. 669-680, 2011.

[27] Yuse, F., Matsushita, M., and Izumi, M.: Steel Plate for Bridges with Long-life Coating (Eco-View), *KOBELCO TECHNOLOGY REVIEW*, No. 34, pp. 6-11, 2016.

[28] 瀧澤一樹：ラック足場（ラックレール式移動吊足場）工法，建設の施工企画，Vol. 722, pp. 36-41, 2010.

[29] 下西勝，桑野忠生，桜井順：首都高速道路を支える調査診断技術，Vol. 46, No. 1, pp. 31-34, 2008.

[30] Lee, J. W., Kim, J. D., Yun, C B., Yi, J. H., and Shim, J. M.: Health-monitoring method for bridges under ordinary traffic loadings, *Journal of Sound and Vibration*, Vol. 257, No. 2, pp. 247-264, 2002.

[31] Miki, C., Koto, Y., Sasaki, E., Saito, K., and Ishikawa, Y.: Long-Term Monitoring of AN Urban Expressway Bridge Using Optical Fiber Sensor System, *Journal of Japan Society of Civil Engineers*, Vol. 71A, No. 3, pp. 416-428, 2015.

[32] Schmidt, D., and Berns, K.: Climbing robots for maintenance and inspections of vertical srtuctures-A survey of design aspects and technologies, *Robotics and Autonomous Systems*, Vol. 61, pp. 1288-1305, 2013.

[33] Ohtsu, S.: Current Status of and Issues relating to Inspection of Infrastructures using Small Unmanned Aerial Vehicles, *Annual Report of NTT Facilities Research Institute*, No. 27, pp. 18-22, 2016. 6.

[34] Hallermann, N., and Morgenthal, G.: Visual inspection strategies for large bridges using Unmanned Aerial Vehicles (UAV), *Proceedings of IABMAS 2014*, Shanghai, China, pp. 1-7, 2014. 7.

[35] Chan, B., Guan, H., Jo, Jun., and Blumenstein, M.: Towards UAV-based bridge inspection systems: a review and an application perspective, *Structural Monitoring and Maintenance*, Vol. 2, No. 3, pp. 283-300, 2015.

[36] Sankarasrinivasan, S., Balasubramanian, E., Karthik, K., Chandrasekar, U., and Gupta, R.: Health Monitoring of Civil Structures with Integrated UAV and Image Processing System, *Procedia Computer Science*, Vol. 54, pp. 508-515, 2015.

[37] Mathew, C.S., and Dayal, K. V.: Robotic Bridge Maintanance System: A Comprehensive Study, *International Journal of Engineering Technology Science and Research (IJETSR)*, Vol. 3, Issue 3, pp. 123-131, 2016.

[38] Paul, G., Webb, S., Liu, D., and Dissanayake, G.: A Robotic System for Steel Bridge Maintenance: Field Testing, Australasian Conference on Robotics and Automation (ACRA 2010), Brisbane, Australia, pp. 1-8, 2010. 1.

[39] Liu, D. K., Dissayanake, G., Manamperi, P. B., Brooks, P. A., Fang, G., Paul. G., Kirchner, N. Chotiprayanakul, P., Kwok, M., and Ren, T. R.: A Robotic System for Steel Bridge Maintenance: Research Challenges and System Design, Australasian Conference on Robotics and Automation, Canberra, Australia, pp. 1-7, 2008. 12.

[40] Nishimoto, S., Kamegawa, T., Gofuku, A., and Matsuno, F.: Proposal of a rail-truck bridge insepction robot and development of a prototype, The 16th SICE System Integration Division Annual Conference, Nagoya, Japan, pp. 2386-2390, 2015. 12.

[41] Kojima, S., Kamio, S., Takane, E., Katsuta, T., Tadakuma, K., Okada, Y., Ohno, K., and Tadokoro, S.: Proposal and Trial of Metallic Wall Inspection Method using Mobile Robot equipped with Distance-Image Sensor, The 16th SICE System Integration Division Annual Conference, Nagoya, Japan, pp. 2242-2246, 2015. 12.

[42] Katsumata, M., Edamoto, K., Nakamura, M., and Hara, Y.: 鋼橋桁を対象とした桁下点検ロボットの開発, The 27th Symposium on Civil Engineering Information Processing System, pp. 57-60, 2002.

[43] Wang, R., and Kawamura, Y.: An Automated Sensing System for Steel Bridge Inspection Using GMR Sensor Array and Magnetic Wheels of Climbing Robot, *Journal of Sensors, Vol. 2016*, Article ID 8121678, 2016.

[44] Takada, Y., Kirimoto, K., Tajiri, T., and Kawai, T.: Development of a Bridge Inspection Robot Working in Three-Dimensional Environment (Evaluation of Driving Performance of a Mechanism with Permanent Magnets), *Transactions of the Japan Society of Mechanical Engineers C*, Vol. 79, No. 805, pp. 155-166, 2013.

[45] Nhan, H. P., and Hung, M. L.: Design and Implementation of an Autonomous Robot for Steel Bridge Inspection, The 54th Annual Allerton Conference, Illinois, USA, pp. 556-562, 2016.

[46] Inari, Y., Sasaki, E., Takahashi, K., Minesawa, G., Takeya, K., and Miki, C.: 鋼橋点検用マイクロロボットの開発, 第 2 回　土木学会西部支部沖縄会　技術研究発表会, pp. 117-122, 2013. 9.

[47] Nakashima, T., Yamamoto, A., and Higuchi, T.: Development of a Wall Climbing Robot using Electrostatic Suction Films, 2006 JSPE Autumn Meeting, Utsunomiya, Japan, pp. 491-492, 2006.

[48] Ruffatto, D. 3rd., Pamess, A., and Spenko, M.: Improving controllable adhesion on both rough and smooth surfaces with a hybrid electrostatic / gecko-like adhesive, *Journal of the Royal Society Interface*, Vol. 11, Issue. 93, pp. 1-11, 2014.

[49] Yoshida, Y., and Ma, S.: Design of a Wall-Climbing Robot with Passive Suction Cups, *Proceeding of IEEE International Conference on Robotics and Biomimetic*, Tianjin, China, pp. 1513-1518, 2010. 12.

[50] Sakai, O.: Trends toward Practical Application of Robotic Technologies for Social Infrastructures, *NTT Facilities Research Institute, Annual Report*, No. 26, pp. 85-89, 2015.

[51] Liu,Y., Dai, Q., and Liu, Q.: Adhesion-adaptive control of a novel bridge-climbing robot, *Proceedings of the 2013 IEEE International Conference on Cyber Technology in Automation, Control and Intelligent Systems*, Nanjing, China, pp. 102-107, 2013. 5.

[52] Iwamoto, T., Furui, S., Inoue, I., and Mori, K: Development of Wireless Remote-Controlled Testing Machine for Vertical Concrete Wall, *Proceeding of the 8th International Conference on Fracture Mechanics of Concrete and Concrete, Structures*, pp. 1773-1777, 2013.

[53] Fumagalli, M., Naldi, R., Macchelli, A., Carloni, R., Stramigioli, S., and Marconi, L.: Modeling and Control of a Flying Robot for Contact Inspection, *Proceedings of IEEE/RSJ International Conference on Intelligent Robots and Systems*, Algarve, Portugal, pp. 3532-3537, 2012. 10.

[54] Ratsamee, P., Kriengkomol, P., Arai, T., Kamiyama, K., Mae, Y., Kiyokawa, K., Mashita, T., Uranishi, Y., and Takemura, H.: A Hybrid Flying and Walking Robot for Steel Bridge Inspection, *Proceedings of 2016 IEEE International Symposium on Safety, Security and Rescue Robotics (SSRR) EPEL*, Lausanne, Switzerland, pp. 62-67, 2016. 10.

[55] Matsuzaka, T., and Hirose, T.: 道路維持管理におけるモニタリングシステムの取組み, *Journal of the institute of Electrical Engineers of Japan*, Vol. 134, No. 7, pp. 428-431, 2014.

[56] East Nippon Expressway Company Limited, CSR Report 2013, pp. 10-15, 2013.

[57] Kuo, C. M., Kuo, C. H., Lin, S.P., Manuel, M. C. E., Lin, P. T., Hsieh, Y. C., and Lu, W. H.: Inftastructure Inspection using an Unmanned Aerial System (UAS) with Metamodeling-Based Image Correction, The ASME 2016 International Design Engineering Technical Conferences and Computers and Information in Engineering Conference, Charlotte, North Carolina, pp. 1-11, 2016. 8.

[58] Ichikawa, A., Abe, H., Ikeda, T., Ohara, K., Kishikawa, J., Ashizawa, S., Ohmichi, T., Okino, T., and Fukuda, T.: Hammering test system with compliance mechanism for inspection of infrastructure with multi-copter, The 16th SICE System Integration Division Annual Conference, Nagoya, Japan, pp. 2380-2381, 2015. 12.

[59] Okada, Y., Ishii, T., Salaan, C. J. O., Ohno, K., and Todokoro, S.: Development of Camera Systems for Visual Inspection of Bridges, The 16th SICE System Integration Division Annual Conference, Nagoya, Japan, pp. 0736-0740, 2015. 12.

[60] Okada, Y., and Okatani, Y.: Development of UAV with Passive Rotating Spherical Shell for Bridge Inspection and its Evaluation of Inspection Capability in Real Bridges, *Journal of the Robotics Society of Japan*, Vol. 34, No. 2, pp. 119-122, 2016.

[61] Tamura, K., Uchiyama, N, Sano, S., and Sakaguchi, T.: Design of a Wall Inspection System Using a Quadrotor Helicopter and Experimental Verification, The 16th SICE System Integration Division Anuual Conference, Nagoya, Japan, pp. 1028-1029, 2015.

[62] Nonami, K.: Rotary Wing Robotics, *Journal of the Robotics Society of Japan*, Vol. 34, No. 2, pp. 74-80, 2016.

[63] Lippiello, V., and Siciliano, B.: Wall Inspection Control of a VTOL Unmanned Aerial Vehicle Based on a Stereo Optical Flow, *Proceedings of IEEE/RSJ International Conference on Intelligent Robots and Systems*, Algarve, Portugal, pp. 4296-4302, 2013. 10.

[64] Miwa, M.: Multi Copter Drone for Investigation at Tunnel Disaster Site, The 16th SICE System Integration Division Annual Conference, Nagoya, Japan, pp. 0741-0743, 2015. 12.

[65] Mizutani, S., Okada, Y., Salaan, C. J., Ishii, T., Ohno, K., and Tadokoro, S.: Proposal and Experimental Validation of a Design Strategy for a UAV with a Passive Rotating Spherical Shell, *Proceedings of IEEE/RSJ International Conference on Intelligent Robots and Systems (IROS)*, Hamburg, Germany, pp. 1271-1278, 2015. 9.

[66] Chen, A. Y., Hung, Y. N., Han, J. Y., and Kang, S. C. J.: A review of rotorcraft Unmanned Aerial Vehicle (UAV) developments and applications in civil engineering, *Smart Structures and Systems*, Vol. 13, No. 6, pp. 1065-1094, 2014.

[67] Guerrero, J.A., and Bestaoui, Y.: UAV Path Planning for Structure Inspection in Windy Environments, *Journal of Intelligent & Robotic Systems*, Vol. 69, Issue. 1–4, pp. 297–311, 2013.

[68] Ashizawa, S., Oomichi, T., Fukuda, T., Ohara, K., Ichikawa, A., and Ikeda, T.: Construction of multi-Copter Simulator for inspection work, The 16th SICE System Integration Division Annual Conference, Nagoya, Japan, pp. 2391-2393, 2015. 12.

[69] Ahn, J. H., Kainuma, S., and Kim, I. T.: Shear failure be-haviors of a web panel with local corrosion depending on web boundary conditions, *Thin-Walled Structures*, Vol. 73, pp. 302-317, 2013.

[70] Yamasawa, T., Nogami, K., Komine, S., Yoda, T., Kasano, H., Murakoshi, J., Toyama, N., Mamoru, S., Arimura, K., and Guo, L.: Remaining compressive ultimate stength of diagonal members in steel truss bridge with imitated corrosions, *Journal of Structure Engineering*, Vol. 59A, pp. 143-155, 2013.

[71] Nogami, K., Yamasawa, T., Oguri, T., and Kato, M.: Evaluation of Capacity Loss Due to Corrosion Damages in Composite I Girder and Steel Columns, *Journal of Structure Engineering*, Vol.47A, pp. 93-102, 2001.

[72] Hamada, A., Sasaki, E., Koma, H., Machida, E., and Kihira, H.: Experimental and numerical evaluation of bearing capacity of steel plate girder affected by end panel corrosion, *Proceedings of constructional steel*, Vol. 17, pp. 731-738, 2009.

[73] Usukura, M., Kondo, A., Yamaguchi, T., Hatanaka, A., Mitsugi, Y., Hashimoto, K., and Sugirura, K.: Ultimate Strength and Repairing Design Method for Stiffeners on the Support of a Plate Girder End for Highway Bridges, *Journal of structural engineering*, Vol. 56A, pp. 722-732, 2010.

[74] "Hung, V. T., Nagasawa, H., Sasaki, E., Ichikawa, A., and Natori, T.: An Experimental and Analytical Study on Bearing Capacity of Supporting Point in Corroded Steel Bridges, *Journal of Japan Society of Civil Engineers*, Vol. 710, I-60, pp. 141-151, 2002.

[75] Khurram, N., Sasaki, E., Kihara, H., Katsuchi, H., and Yamada, H.: Analytical demonstrations to assess residual bearing capacities of steel plate girder ends with stiffeners damaged by corrosion, *Structure and Infrastructure Engineering*, Vol. 10, No. 1, pp. 69-79, 2014.

[76] Khurram, N., Sasaki, E., Katuschi, H., and Yamada, H.: Finite element investigation of shear capacity of locally corroded end plate girder, *International Journal of Steel Structures*, Vol. 13, No. 4, pp. 623-633, 2013.

[77] Khurram, N., Sasaki, E., Katuschi, H., and Yamada, H.: Experimental and numerical evaluation of bearing capacity of steel plate girder affected by end panel corrosion, *International Journal of Steel Structures*, Vol. 14, No. 3, pp.659-676, 2014., *ERRATUM*, Vol. 15, No. 1, pp.245, 2015.

[78] Rose, J. L.: A Baseline and Vision of Ultrasonic Guided Wave Inspection Potential, *Journal of Pressure Vessel Technology*, Vol. 124, pp. 273-282, 2002.

[79] Murakoshi, J., Takahashi, M., Iitsuka, T., and Ono, S.: Study on applicability of existing NDE techniques to measure remaining thickness of corroded steel plate, *Journal of Structure Engineering*, No. 59A, pp. 711-724, 2013.

[80] Shimozato, T., Tamaki, Y., Arizumi, Y., Yabuki, T., Ono, S., and Miki, C.: Corrosion performance of an aged weathering steel bridge in marine atmosphere environment, *Journal of Structure Engineering*, Vol. 62A, pp. 785-795, 2016.

[81] 社団法人日本非破壊検査協力会: 渦電流探傷試験Ⅲ, 2008.

[82] Ando, S., Kitane, Y., Nishijima, Y., Itoh, Y., and Nakano, Y. Study on output from the pulsed eddy current testing on steel plates with thickness loss of various shapes, *Journal of Structure Engineering*, Vol. 62A, pp. 603-616, 2016.

[83] Sullivan, S., Atherton, D. L., and Schmidt, T. R.: Comparison of conventional, through-wall and remote field eddy current techniques, *NDT International*, Vol. 22, No. 4, pp. 203-208, 1989.

[84] Yamamoto, T., Takagi, T., and Uchimoto, T.: Evaluation of Local Wall Thinning by the Use of RFECT for Flats Plates, *Journal of the Japan Society of Mechanical Engineering B*, Vol. 75, No. 751, pp. 431-433, 2009.

[85] Sun, Y., Ouyang, T., and Udpa S.: Multi-layer aircraft structure inspetion using super-sensitive Remote-Field Eddy-Current system, *AIP Conference Proceedings*, Vol. 557, Issue. 1, pp. 1906-1913, 2001.

[86] Lebrun, B., Jayet, Y., and Baboux, J. C.: Pulsed eddy current signal analysis: application to the experimental detection and characterization of deep flaws, *NDT & E International*, Vol. 30, No. 3, pp. 163-170, 1997.

[87] Angani, C. S., Park, D. G., Kim, C. G., Kollu, P., and Cheong, Y.M.: Dual core differential pulsed eddy current probe to detect the wall thickness variation in an insulated stainless steel pipe, *Journal of Magnetics*, Vol. 15, No. 4, pp. 204-208, 2010.

[88] Murakoshi, J., Takahashi, M., Iitsuka, T., and Ono, S.: Study on applicability of existing NDT techniques to measure remaining thickness of corroded steel plate, *Journal of Structure Engineering*, Vol. 59A, pp. 711-724, 2013.

[89] Park, D. G., Angani, C. S., Rao, B. P. C., Vértesy, G., Lee, D. H., and Kim, K. H.: Detection of the Subsurface Cracks in a Stainless Steel Plate Using Pulsed Eddy Current, *Journal of Nondestructive Evaluation*, Vol. 32, Issue. 4, pp. 350-353, 2013.

[90] Shimada, M., Naruse, T., Yoshii, T., and Suagsawa, S.: Fundamental Study on Non-Destructive Evaluation for the Degradation of Corroded Structural Materials, *National Maritime Research Institute*, Vol. 37, No. 1, pp. 1-17, 2000.

[91] Li, J., Wu, X., Zhang, Q., and Sun, P.: Measurement of lift-off using the relative variation of magnetic flux in pulsed eddy current testing, *NDT&E International*, Vol. 75, pp. 57-64, 2015.

[92] Kimura, Y., Murakoshi, J., Honma, H., Takahashi, M., and Hiroe, A.: Research on the Application of Nondestructive Inspection Technology to Highway Bridges, *Outline of Priority Research Projects Report, PWRI*, No. 23, pp. 1-14, 2013.

[93] Kitane, Y., Nishijima, Y., Itoh, Y., and Nakano, Y.: Feasibility Study of Thickness Measurement using Pulsed Eddy Current for Post Steel Structures, *Proceedings of constructional steel*, Vol. 22, pp. 943-949, 2014.

[94] Cheng, W., Hiyoku, S., Furukawa, T., Kako, A., and Ikedou, K.: Pulsed Eddy Current Testing of Wall-Thinning Over Insulation, The thermal and nuclear power generation convention 2014, Nagoya, Japan, pp. 40-45, 2014.

[95] Fan, M., Cao, B., Tian, G., Ye, B., and Li, W.: Thickness measurement using liftoff point of intersection in pulsed eddy current responses for elimination of liftoff effect, *Sensors and Actuators A: Physical*, Vol. 255, pp. 60-74, 2016.

[96] Kosaka, D., and Hashimoto, M.: Numerical and Experimental Study on Pulsed Eddy Current Testing in Steel Thickness Measurement, *Journal of Japan Society for Non-Destructive Inspection*, Vol. 64, No. 5, pp. 245-250, 2014.

[97] NIHON PISCO CO., LTD.: エア流量・有効断面積計算ツール, https://www.pisco.co.jp/technology/flow/, accessed 21th May 2015.

[98] DeGarmo, E. P., Black, J. T., and Kohser, R. A.: Measurement and inspection, in 9th ed., New York, NY: Wiley. *Material and process in manufacturing*, Chapter 10, pp. 72-81, 2003.

[99] Yokoyama, K.: Wind loading and wind resistant design manual for high way bridges, *Journal of Wind Engineering*, No.44, pp. 1-11, 1990.

[100] Zhang, Z.: Camera Calibration, in Medioni, G., and Kang, S. B. (Eds.), Emerging Topics in Computer Vision*, Prentice Hall Professional Technical Reference*, Chapter 2, pp. 4-43, 2004.

[101] Nagai, I., Watanabe, K., Nagatani, K., and Yoshida, K.: Noncontact position estimation device with optical sensor and laser sources for mobile robots traversing slippery terrains, *Proceedings of the 2010 IEEE/RSJ international conference on intelligent robots and systems*, Taipei, Taiwan, pp. 3422-3427, 2010.

[102] Navarro-Serment, L. E., Paredis, C. J. J., and Khosla, P. K.: A beacon system for the localization of distributed robotic teams, International conference on field and service robotics, Pittsburgh, PA, pp. 232-237, 1999.

[103] Aoki, T., Ito, K., Shibahara, T., and Nagashima, S.: High-accuracy machine vision using phase-only correlation, *IEICE ESS Fundamentals Review*, No.1, pp. 30-40, 2007.

[104] Ito, K., Nakajima, H., Kobayashi, K., Aoki, T., and Higuchi, T.: A fingerprint matching algorithm using phase-only correlation, *IEICE Transactions Fundamentals*, Vol. E87-A, No. 3, pp.682-691, 2004.

[105] Takita, K., Aoki, T., Sasaki, Y., Higuchi, T., and Kobayashi, K.: High accuracy subpixel image registration based on phase-only correlation, *IEICE Transactions Fundamentals*, Vol. E86-A, No. 8, pp. 1925-1934, 2003.

[106] Salman, M., Mathavan, S., Kamal, K., and Rahman, M.: Pavement crack detection using gabor filter, *Proceedings of the 16th international IEEE annual conference on intelligent transportation systems (ITSC 2013)*, Hague, The Netherland, pp. 2039-2044, 2013.

[107] Koyama, S., Maruya, T., Horiguchi, K., and Sawa, T.: Digital Image Analysis of Cracks on the Concrete Surface Based on the Gabor Wavelet Transformation, *Journal of Japan Society of Civil Engineers E2*, Vol. 68, No.3, pp. 178-194, 2012.

[108] Tamehiro, N.: Numerical Modeling and Analysis Methods for Monitoring of Transportation Infrastructure, *Journal of the Institute of Electrical Engineers of Japan*, Vol. 134, No. 7, pp. -4232014.

[109] Tai, M., Shimozato, T., Tamaki, Y., Arizumi, Y., and Yabuki, T.: Analytical investigation on collapse mechanism of steel girder bridge due to severe corrosion damage and damage recovery evaluation at bridge end span, *Journal of Structure Engineering*, Vol. 61A, pp. 416-428, 2015.

[110] Otake, Y., Sasuga, T., Honjo, Y., Murakami, S., and Kobayashi, K.: Statistical study on evaluating bridge health degree based on bridge inspection database, *Journal of Japan Society of Civil Engineers A2*, Vol. 67, No. 2, pp. I_813-I_824, 2011.

[111] Yamamoto, T., Takagi, T., and Uchimoto, T.: Extraction of Crack Indications from Detecting Signals based on Signal Phase Characteristics in Eddy Current Testing, *Journal of Japan Society of Mechanical Engineers A*, Vol. 76, No. 761, pp. 117-125, 2010.

[112] Koyama, K., Hoshikawa, H., and Kadoya, Y.: Surface Flaw Testing of Weld Zones using a Uniform Eddy Current Probe Intended to Detect Longitudinal and Transversal Flaws by Single Scanning, *Journal of Japan Society for Non-Destructive Inspection*, No. 5, pp. 275-282, 2011.

[113] Furukawa, T., Tanaka, H., Itoh, H., Fukumoto, H., and Ohchi, M.: Dynamic Electromagnetic Analysis of Guitar Pickup aided by COMSOL Multiphysics, *Proceedings of COMSOL Conference Tokyo 2012*, Tokyo, Japan, pp. 1-9, 2012.

[114] Santandrea, L., and Bihan, Y. L.: Using COMSOL-Multiphysics in an Eddy Current Non-Destructive Testing Context, *Proceedings of the COMSOL Conference 2010*, Paris, France, pp. 3576, 2010.

[115] Bennoud, S., and Zergoug, M.: Modeling and Simulation for 3D Eddy Current Testing in Conducting Materials, International, *International Journal of Mechanical, Aerospace, Industrial, Mechatronic and Manufacturing Engineering*, Vol. 8, No. 4, pp. 754-757, 2004.

[116] Erdogan, M., Tunc, S., Yildiz, S., and Inanir, F.: A Comparative Study of AC Transport and Eddy Current Losses for Coil Made of HTS Tapes Coated with Copper Stabilizer, *Journal of Superconductivity and Novel Magnetism*, pp. 1-7, DOI 10.1007/s10948-016-3855-x, 2016.

[117] Ota, T., Mitsutake, Y., and Tamura, H.: Electromagnetic Field Analysis Method for High-Efficiency Wireless Energy Transfer, *Panasonic Technical Journal*, Vol. 59, No. 1, pp. 51-56, 2013.

[118] Sekimoto, Y., Ogiso, N., Kawase, Y., Yamagchi, T., Nakano, T., Ono, Y., and Nishikawa, N.: Development of high-efficiency bus-bar, 平成 23 年度先端研究施設共用促進事業「地球シミュレータ産業戦略利用プログラム」利用成果報告書, pp. 83-912012.8.

[119] Yamada, T., and Suzuki, I.: An electromagnetic Method of Measuring Thickness, Journal of the Institute of Electronics, *Information and Communication Engineers*, Vol. J71-A, No. 7, pp. 1453-1460, 1988.

[120] Yamada, T., and Suzuki, I.: An Application of Electromagnetic Thickness Sensor to Measurement of the Object Coated with Film, *Transactions of the Society of Instrument and Control Engineers*, Vol. 27, No. 2, pp. 134-139, 1991.

[121] Gao, J., Pan, M., and Luo, F.: Defect Identification and Classification of Multi-Frequency Eddy Current Test based on Spectrum Method, *Proceedings of the 2010 IEEE International Conference and Automation, Harbin*, China, pp. 1883-1886, 2010. 6.

[122] Betta, G., Ferrigno, L., Laracca, M., Burrascano, P., Ricci, M., and Silipigni, G.: An experimental comparison of multi-frequency and chirp excitations for eddy current testing on thin defects, *Measurement*, Vol. 63, pp. 207-220, 2015.

[123] Hayashi, H., Kainuma, S., Yamamoto, Y., and Itoh, Y.: Effect of corrosion product on measuring thickness accuracy of rust layer formed on steel plate by electro-magnetic thickness tester, *Proceedings of Constructional Steel*, Vol. 21, pp. 862-868, 2013.